Effects of Polymer-Nanoparticle Interactions on the Dynamics of Attractive Polyhedral Oligomeric Silsesquioxane Nanocomposites

EFFECTS OF POLYMER-NANOPARTICLE INTERACTIONS ON THE DYNAMICS OF ATTRACTIVE POLYHEDRAL OLIGOMERIC SILSESQUIOXANE NANOCOMPOSITES

A Dissertation Presented

by

WALTER W. YOUNG

Submitted to the Graduate School of the
University of Massachusetts Amherst in partial fulfillment
of the requirements for the degree of

DOCTOR OF PHILOSOPHY

February 2024

Department of Polymer Science and Engineering

EFFECTS OF POLYMER-NANOPARTICLE INTERACTIONS ON THE DYNAMICS OF ATTRACTIVE POLYHEDRAL OLIGOMERIC SILSESQUIOXANE NANOCOMPOSITES

A Dissertation Presented

by

WALTER W. YOUNG

Approved as to style and content by:

_____
Reika Katsumata, Chair

_____
Murugappan Muthukumar

_____
E. Bryan Coughlin

_____
Manasa Kandula

_____
Alfred J. Crosby, Department Head
Polymer Science and Engineering

ACKNOWLEDGMENTS

Much of the text and many of the figures are adapted directly from works that are published or under revision, as noted. This work has been supported financially by the National Science Foundation (DMR #2046606), a Department of Education Graduate Assistance in Areas of National Need (GAANN) fellowship, and Startup Funding from the University of Massachusetts Amherst.

I would not be able to present this body of work without the help of countless individuals who have supported me along the way, and an environment which presented opportunities for me to excel and grow into the researcher I am today. I am particularly grateful to have had access to excellent formal and informal education systems growing up in the Twin Cities, and throughout my time at the University of Minnesota and the University of Massachusetts. I would like to specifically acknowledge some of the people who have contributed to these communities.

To my advisor, Dr. Reika Katsumata, it has been a pleasure to work with you and learn from you during my time as a graduate student. Your incredible patience has allowed me to push through setbacks, turning would-be failures into learning experiences that have improved the quality of our research.

To my committee members, you all have contributed in meaningful ways to the success of my research. Dr. Manasa Kandula, I will always appreciate your keen interest in my work. Our discussions always gave a fresh perspective that helped pull me out of the weeds and identify key areas for future exploration and study. Dr. Bryan Coughlin, you have checked my synthetic work and gave me the confidence to tackle some problems on my own while identifying areas where I needed to ask for help. Dr. Murugappan

Muthukumar, your sharp eye has preemptively saved me a great deal of time by forcing me to take a step back and check whether my conclusions are the best ones to draw based on the available data.

Countless individuals have aided me in mastering the experimental techniques I carried out during my thesis work. These include Dr. Weiguo Hu for nuclear magnetic resonance (NMR), Dr. Jim Chambers for fluorescence microscopy, Dr. Alex Ribbe and Louis Ribbon for electron microscopy, and Dr. Steve Eyles for mass spectrometry. I would also like to extend my gratitude for discussions related to synthesis and characterization: Carolyn Zhao for P(S-r-2VP) synthesis, Dr. Rick Laine, Dr. Tom McCarthy, and Dr. Bryan Coughlin for octa(aminophenyl) silsesquioxane OAPS synthesis, Dr. Henning Winter and Dr. Benjamin Yavitt for discussions of rheometry, and Dr. Benjamin Yavitt again for aiding in the interpretation of x-ray scattering results. Finally, Glenda Pons and Jack Hirsch deserve a hearty thank-you for their large role in getting the Katsumata Group lab space set up.

To my former managers during my time at 3M and Apple, Lan Liu, Dr. Tom Klun, Nate Morris, in addition to countless other colleagues such as Toni, Eli, Giuseppe, Salma, Pom, Yuanyuan, Pom, Suzane, and Vi, thank you for helping me learn the practical applications of polymer science to engineering, as well as other intangible skills.

To my colleagues in the Katsumata Group, I have always been delighted by our group's ability to be inquisitive and critical of ideas while remaining supportive and respectful, all while creating a welcoming environment for everyone. I am excited to see where our journeys take us.

I am also deeply grateful for the rest of the student body in the Polymer Science and Engineering department, particularly folks such as Dylan, Jerred, James, Evon, Demi, Deborah, Brandon, Eva, and Roshni as well as the rest of the incoming class of 2018 not mentioned specifically. Looking back at my time in grad school, the long hours spent in the lab and classroom were made bearable given the camaraderie and friendship I shared with you all.

I would also like to thank those outside of the polymer science and engineering community who have supported me in no less meaningful ways.

To my friends in Western Massachusetts and beyond, including but not limited to Bennett, Michael, Andy, Adam, Cesario, Greta, Firdavs, Kyle, Amber, Matt, Abdul and Rajvi, the joy you have brought to my life has been a constant source of energy and strength over the years, without which I would certainly have been burnt out a long time ago.

To William. I am so proud of your strength, resilience, passion, and drive. Despite being your older brother, I can safely say that I look up to you now!

To my parents. You both instilled in me a sense of wonder and curiosity. Dad, you taught me from a young age to keep promises and to honor commitments, even if that commitment goes unappreciated initially. It is fitting that you would model this mindset while raising me, because I know that as a kid I was not as appreciative of this lesson as I am now! Mom, you instilled in me a wonderful sense of curiosity, and love for tackling problems with mathematical reasoning. Perhaps more importantly, you showed me how to see the world with compassion, love, and acceptance.

To Ananya. I can’t begin to describe what you mean to me. Thank you for everything. I hope that as a husband I will be able to support you through your life in the same way you have supported me over these years.

CONTRIBUTIONS

Solid state NMR measurements presented in Chapter 2 were performed by Dr. Weiguo Hu of the University of Massachusetts NMR Core Facility.

Coarse grained and all-atom molecular dynamics simulations presented in Chapter 2 were performed by Dr. Rui Shi and Dr. Xiang-Meng Jia at Jinlin University, under the supervision of Dr. Hu-Jun Qian.

Joseph Saez aided in the synthesis of some poly(styrene-*r*-2-vinylpyridine) copolymers used in Chapter 2, and Jasney Combs aided in some of the strain-sweep rheometry measurements presented in Chapter 3.

All dielectric relaxation spectroscopy (DRS) measurements presented in Chapter 4 were performed at Ritsumeikan University by Hiromu Tabuchi, Ryo Iguchi, Hiroki Nobori, and Jun Yoshioka, under the supervision of Dr. Koji Fukao.

ABSTRACT

EFFECTS OF POLYMER-NANOPARTICLE INTERACTIONS ON THE DYNAMICS OF ATTRACTIVE POLYHEDRAL OLIGOMERIC SILSESQUIOXANE NANOCOMPOSITES

FEBRUARY 2024

WALTER W. YOUNG, B.S., UNIVERSITY OF MINNESOTA TWIN CITIES

M.S., UNIVERSITY OF MASSACHUSETTS AMHERST

PH.D., UNIVERSITY OF MASSACHUSETTS AMHERST

Directed by: Professor Reika Katsumata

Polyhedral oligomeric silsesquioxane (POSS) had long been recognized as a critical building block for inorganic-organic hybrid materials with unique and desirable properties and performance. Through synthesis and characterization of polymer/POSS nanocomposites, direct insights into the significant effects of the polymer/POSS interactions on the resulting material properties are obtained. Random copolymers of a hydrogen-bond accepting monomer and a non-interacting monomer are synthesized and loaded with a model amine-functionalized hydrogen bond donating POSS molecule via solution casting, to create a material with well-controlled dynamical heterogeneity. The increase in the glass transition temperature (T_g) of these materials is found to strongly depend on the number of interacting groups in the system. Essentially, the effect of increasing the POSS loading is the same effect as increasing the number of interacting monomers in the copolymer. Likewise, POSS molecules with a variable number of amines were synthesized and loaded into a hydrogen bond accepting homopolymer. Similar to what was observed for the random copolymers, increasing the functionality of the nanofiller increased the T_g enhancement effect. To probe the purported effects of POSS

molecules on entanglement dynamics, composites were prepared with a range of polymer molar masses. Across these materials, critical rheological timescales were observed which point to a relaxation process that occurs independently of the presence of entanglements, and scales exponentially with POSS loading. Attempts to probe this process with other experimental techniques such as dielectric relaxation spectroscopy were inconclusive due to competing experimental effects at similar frequencies. Overall, these results on highly controlled model materials reveal the role of specific nanofiller interactions on the properties of polymer composites.

TABLE OF CONTENTS

Page

LIST OF TABLES

Page

LIST OF FIGURES

Page

LIST OF SCHEMES

Page

CHAPTER 1

1 - INTRODUCTION: POLYMER NANOCOMPOSITES AND MULTISCALE DYNAMICS

1.1 – Polymer Nanocomposites

Polymer nanocomposites are used in applications for their ability to tune processability and provide exceptional material performance in ways otherwise inaccessible to polymers or fillers alone,[1] from the classic example of adding carbon black in tires to recent examples of conductive fillers added to 3D printing materials.[2] In efforts to establish the design rules of nanocomposite processing, understanding the dynamics of these systems at different length scales has been a key research thrust because segmental dynamics dictate properties in the glass state while entire chain dynamics dictate melt properties.[3–6] The complex polymer-nanoparticle interactions at the interface complicate this problem, particularly owing to the spatially heterogeneous nature of polymer chains in nanocomposites. These heterogeneous dynamics of the matrix polymer are also substantially influenced by nanofiller and polymer size,[5,7–15] molecular structure,[16–18] and changes in morphology due to processing conditions.[19–22] Molecular-level understanding of structure-property relationships in nanocomposites could enable rational design of polymeric materials with substantially improved properties for a wide variety of materials ranging from 3D printable resins to lightweight structural materials. Thus, it is critical to develop a solid fundamental understanding of these unique materials.

1.1.a – Structure and Dynamics in Nanocomposites

Numerous studies have been performed on the melt-state segmental and chain dynamics of homopolymer nanocomposites with nanofillers of size 10 nm or greater, and most of the systems studied have attractive interactions between matrix polymers and nanofillers to prevent aggregation of the nanofillers. From these studies, it is clear that a bound layer with substantially reduced mobility is found several nanometers from the nanofiller interface, while a relatively more mobile interfacial layer extends by approximately one radius of gyration,[4,7,12,14,16,23–30] and that polymer chains can form bridges between nanoparticles.[7,13,31–34]

Initial studies on the interfacial layers of polymer chains at nanofiller surfaces used thermogravimetric analysis (TGA) to infer the thickness of the interfacial layer by essentially burning off the unbound polymer and measuring the mass of residue that remained on the surface. This can then be converted to an interfacial layer thickness if the density of the polymer is assumed to be the same at the interface as in the bulk (Figure 1a).[29] This typically yields a result of a few nanometers of thickness. However, other experimental techniques suggested much larger interfacial layers. Dynamic light scattering (DLS) of nanofillers that had been annealed inside a polymer matrix before dissolving the matrix in solvent, leaving only the bound polymer layer, revealed an interfacial layer thickness on the order of 10 nm, as did transmission electron microscopy (TEM) analysis of the spacing of nanofillers. The situation was somewhat clarified by the use of broadband dielectric spectroscopy, which is able to distinguish between α-relaxations at the interface versus in the bulk (Figure 1b).[14] The present understanding of the polymer/nanofiller interface consists of a dynamic interfacial layer of several nanometers, and a bound

interfacial layer, extending approximately ~1 R_g from the nanofiller surface. This bound interfacial layer is not dynamically different from the matrix polymer at distances further than a few nanometers from the interface, but it is effectively irreversibly adsorbed to the interface on any relevant polymer timescale.[14,35] In contrast, nanocomposites with filler sizes smaller than 10 nm have unusual properties compared to those with larger filler sizes, largely owing to the lack of the same sort of interfacial layer at the nanofiller surface.

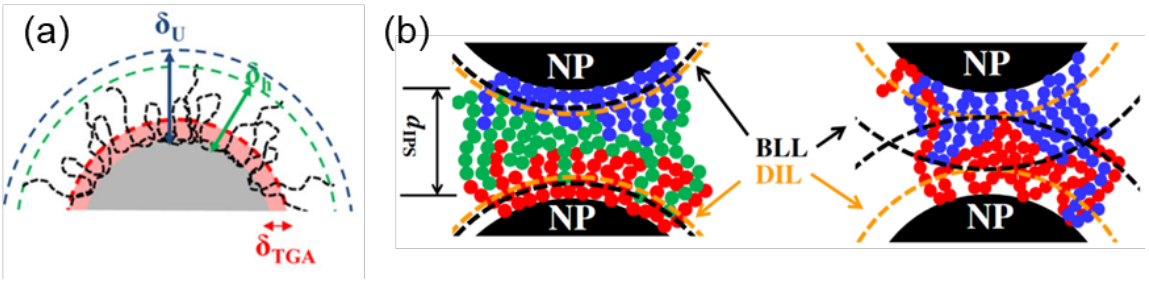

Figure 1. a) Different observed interfacial layer thickness measured by TGA (δ_{TGA}), hydrodynamic thickness measured by DLS (δ_h), and interaction potentials inferred from TEM images (δ_U). Adapted with permission from Jouault, N.; Moll, J. F.; Meng, D.; Windsor, K.; Ramcharan, S.; Kearney, C.; Kumar, S. K. Bound Polymer Layer in Nanocomposites. ACS Macro Lett. 2013, 2 (5), 371–374. https://doi.org/10.1021/mz300646a. Copyright (2018) by the American Physical Society.[29] b) Illustration of the distinction between the bound loop layer (BLL) and the dynamic interfacial layer (DIL) for polymer chains of different lengths, inferred from dielectric spectroscopy measurements. Adapted figure with permission from Cheng, S.; Holt, A. P.; Wang, H.; Fan, F.; Bocharova, V.; Martin, H.; Etampawala, T.; White, B. T.; Saito, T.; Kang, N.-G.; Dadmun, M. D.; Mays, J. W.; Sokolov, A. P. Unexpected Molecular Weight Effect in Polymer Nanocomposites. Phys. Rev. Lett. 2016, 116 (3), 038302. doi.org/10.1103/PhysRevLett.116.038302.[14]

1.2 – Polymer-POSS Nanocomposites

Nanocomposites prepared with much smaller nanofillers on the order of 2 nm in diameter, often polyhedral oligomeric silsesquioxane (POSS) derivatives, have categorically different behavior compared to nanocomposites with larger fillers. Polymer/POSS composites in particular are a system that has been explored extensively

over the last three decades with the lens of engineering applications, spanning simple mechanical reinforcement to tunable surface properties.[36–43] POSS is an attractive building block for advanced materials due to its high thermal stability,[44,45] low refractive index,[45] and ability to incorporate diverse chemistries into its molecular structure. The silicon content of POSS can make it a useful component in lithographic resist materials.[40] UV-stable coating materials with high transparency and gloss have been created using POSS and polymer in conjunction with other inorganic fillers such as titania,[46] while oleophobic coatings have been created by introducing fluorinated functionality to the POSS structure, both covalently bound to polymers or as unbonded blend constituents.[47,48]

In contrast, the use of polymer/POSS composites as a model system to study the extremely small length scale side of nanocomposite dynamics is more recent.[5,8,10,49] Because loadings over 50 vol% have been achieved without filler aggregation in poly(2-vinylpyridine)/octa(aminophenyl) silsesquioxane (P2VP/OAPS) due to the strong hydrogen bonding between the two components, these nanocomposites are "all-interfacial," (shown schematically in Figure 2),[7] a distinction that is also supported by simulation.[7] This substantially changes the physical layout of the system because interparticle spacings are sub-nanometer at high loadings. These systems display unique behaviors due to the extremely small size of the fillers,[3,5,42,43] and are distinct from dynamic crosslink systems due to the very high volume fraction of filler and the lack of elastomeric behavior at all temperatures and compositions.[50]

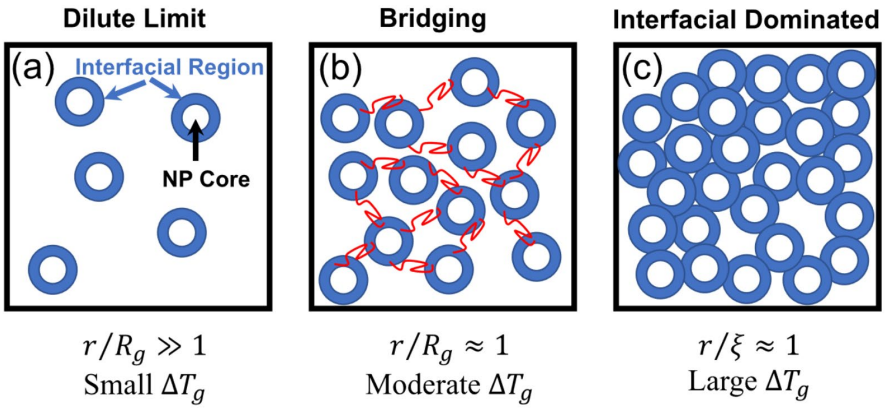

Figure 2. Illustration of the different regimes of polymer nanocomposite structure. Reprinted figure with permission from Emamy, H.; Kumar, S. K.; Starr, F. W. Diminishing Interfacial Effects with Decreasing Nanoparticle Size in Polymer-Nanoparticle Composites. Phys. Rev. Lett. 2018, 121 (20), 207801. doi.org/10.1103/PhysRevLett.121.207801. Copyright (2018) by the American Physical Society.[7]

1.3 – Multiscale Dynamics of Polymer-POSS Nanocomposites

These stark structural differences between POSS nanocomposites and more conventional nanocomposites can give rise to strikingly different dynamical behavior. Because polymer molecules span multiple length scales, ranging from the sub-nanometer molecular structure to the often 10 nm or larger radii of gyration, their dynamical behavior and movement is controlled by a cascading series of emergent phenomena. This Dissertation will focus on glass transition temperatures and alpha relaxation times of POSS nanocomposites, flow occurring at long times, and the various molecular processes that occur on timescales between these glassy dynamics and terminal flow.

1.3.a –Glass Transition and Glass Transition Temperature (T_g)

Rationalizing the change in T_g in multi-component polymeric systems such as nanocomposites is critical for a variety of applications, because T_g dictates the temperature range over which a material can operate.; for example, while a thermoplastic may need to

operate below its T_g to stay tough and avoid creep, an elastomer may need to operate above T_g to remain highly elastic. In the simplest case, where two glass forming components with no strong interactions are physically blended or copolymerized, the Fox equation[51] tends to perform adequately, taking the T_g of the mixture of i components to be

$$\frac{1}{T_{g,\mathrm{mix}}} = \sum_i \frac{w_i}{T_{g,i}} \tag{1.1}$$

where w_i is the weight fraction of the ith component. In the years since this empirical framework was proposed in 1955, numerous other treatments have been put forth. Some offer improved accuracy under certain conditions, often with the addition of fitting parameters, while others attempt to offer a more robust physical description.[52] One popular derivation of the Fox equation approaches the situation from the lens of thermodynamics and the Gibbs-Demarzio theory of the glass transition, which posits that the free volume of a material dictates the temperature at which glass formation occurs.[53–55] This derivation considers the total entropy of the system to be equal to the configurational entropy of the two components plus the additional entropy of mixing. When certain numerical approximations and assumptions about the heat capacities of the materials are made, the Fox equation is returned.

However, no theory of the glass transition itself has yet been universally accepted[56–58], so it is thus unclear which of the theories regarding the T_g of polymer blends is the most accurate. For this reason, theorists may be aided by experiments which probe T_g in relatively underexplored, yet highly controlled model systems, such as polymer/POSS nanocomposites.

It appears that no universal trend exists that can explain all of the various T_g effects of incorporating POSS into a polymer matrix, either as a covalently attached group, or as

a blend component based on an extensive collection of T_g data as a function of POSS loading.[59] In particular, the Fox equation seems poorly suited for this task of rationalizing the T_g change in POSS nanocomposites.[59] Nevertheless, it is clear that POSS can have a strong effect on T_g, and that this effect will be dependent on the chemical nature of the components in the system. Experiments and simulations on attractive polymer/POSS systems observe T_g enhancement with an approximately linear increase in T_g with interaction strength, as discussed and supported by experiments presented in Chapter 2. This can be treated quantitatively with various theories of glass formation, such as with interaction strength being modeled as a cohesive energy density,[60] work of adhesion,[61] in analogy to recent work on fractions of stickers in neat linear polymers with attractive end-groups.[62]

1.3.a.i – Slower Arrhenius Relaxation Processes in Glasses

Intimately related to theories of the glass transition are theories regarding physical aging in glass forming materials, where the structure of a glassy material changes while kept well below T_g. This structural change results in densification and more ordered packing of the glass former, changing important properties of the material such as increased stiffness and reduced toughness. Recent reports of slower Arrhenius processes observed in dielectric spectroscopy measurements of polymer thin films,[63] metallic glasses[64], and molecular glass formers[65] have revealed potential connections between physical aging and molecular relaxation phenomena which occur independent of the α-process and have an Arrhenius temperature dependence. Dielectric relaxation spectroscopy was used to analyze the thin polymer films, with electrodes deposited onto the thin films to avoid air gaps according to standard procedures. The measurements of metallic glasses and molecular

glass formers were carried out via flash differential scanning calorimetry. This additional experimental evidence may prove critical for understanding the apparent decoupling between observed rates of relaxation in polymer glasses below T_g, in which the structural rearrangements occur on timescales many orders of magnitude faster than what would be expected if the relaxations possessed the same temperature dependence as the α-process in all temperature regimes.

Chapter 4 of this Thesis shows an example of the use of dielectric relaxation spectroscopy as a technique for measuring nanocomposite dynamics and highlights potential pitfalls of searching for relaxation processes that occur slower than the frequency of the α-process. Given how susceptible measurements of relaxations in the glassy state are to concerns regarding experimental technique, and the resulting confusion regarding which experimentally observed phenomena theory ought to explain,[66–69] it is critical to conduct experiments that hold up to rigorous scrutiny.

1.3.b –POSS Dynamics

The dynamics of the motion of attractive POSS fillers seems to be well explained by the so-called "vehicle mechanism", presented by Sokolov, Schweizer and coworkers.[8,49] In this theory, the short-time motion of POSS is modeled as being predominantly controlled by the polymer segmental dynamics, rather than the entire chain dynamics. This framework explains the near independence of POSS motion on polymer molar mass when polymer radius of gyration is larger than the size of the nanofillers.[5,8] This is distinct from nanocomposites with larger fillers where the core-shell model applies. The nanofiller carries a shell of adsorbed polymer, and its motion is thus strongly coupled to the length of the polymer chains it carries.[5,8]

Essentially, the vehicle mechanism applies under a particular set of conditions. First, the radius of gyration (R_g) of the polymer must be much larger than the radius of the nanofiller. If polymer R_g is smaller than the nanofiller radius, the nanofiller motion will be well-described by Stokes-Einstein diffusion. Second, the desorption time of polymer segments to the nanofiller surface must be much shorter than the diffusion timescale of the nanofiller. If this condition is not met, the nanofiller motion will be strongly coupled to the dynamics of the chain itself. This condition also effectively rules out any systems with bound interfacial layers of polymer chains, which is almost ubiquitously observed in attractive, well-dispersed polymer nanocomposites with larger (~10 nm) fillers.

1.3.c – Rheology

1.3.c.i –Strongly-Interacting Polymer/POSS Nanocomposites

Polymer/POSS nanocomposites share some thermophysical and mechanical similarities with other nanocomposites, such as gel-like mechanical responses at high filler loadings.[10] However, they differ in other important regards, such as strong T_g enhancement as mentioned previously,[10,70,71] in addition to two anomalous features in the rheological response: 1) relatively unchanged zero-shear viscosity, and 2) decreased entanglement plateau width at high OAPS loadings.[10] Cheng et al. reported that T_g of P2VP/OAPS 37 vol% system was 22 °C higher than neat P2VP, yet the zero-shear viscosity of the corresponding composite was nearly identical to the neat P2VP. This indicates that models such as sticky Rouse cannot capture the nature of this dynamic response; the model would predict a large increase in the terminal relaxation time of entangled polymers with increasing OAPS loading.[72–75] This unique rheological property points to an opportunity to

reveal unconventional processing/property relationships, *e.g.*, high T_g polymer materials with low viscosity. Beyond the decoupling of zero-shear viscosity and T_g, P2VP/OAPS also displays an apparent decrease in the width of the entanglement plateau with increasing OAPS loading, as the entanglement onset time (τ_e) approaches the terminal flow time (τ_t), as shown in Figure 3. This change in entanglement onset times cannot be explained by tube dilution, so therefore must have a distinct physical description which is currently unclear, though it has been termed a disentanglement effect in the literature.[10] To fully understand the rheological behavior of nanocomposites, it is necessary to independently understand the frequency and temperature dependence of every relaxation process occurring in the material. A complete description of the anomalous response of P2VP/OAPS composites would be useful for developing models of nanocomposite behavior across the experimentally accessible window of nanofiller sizes. This remains a key open question in the field of polymer nanocomposite dynamics across all length-scales, not just for extremely small filler sizes.[76,77]

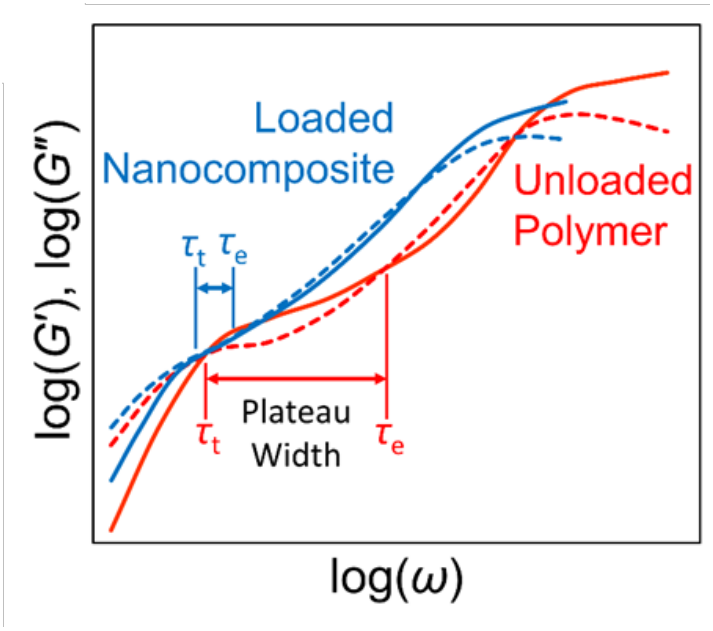

Figure 3. Typical P2VP/OAPS rheological response for entangled systems adapted from data from Cheng et al.[10], where solid lines show *G′,* dashed lines show *G″*. The terminal flow times τ_t and entanglement onset times τ_e are labeled, where the distance between them is the width of the entanglement plateau. The entanglement plateau appears to shrink in the OAPS loaded sample.

1.3.c.ii –Weakly-Interacting Polymer/POSS Nanocomposites

The interplay between entanglement dynamics and POSS molecules is dependent on the chemical identity of the filler and the matrix. In particular, when the polymer/filler interactions are weak, POSS molecules will effectively "disentangle" the polymer melt, reducing the storage modulus at the entanglement plateau and thus the apparent molar mass between entanglements, though this effect is not particularly strong as it appears to be on the order of experimental uncertainty (Figure 4).[43,78]

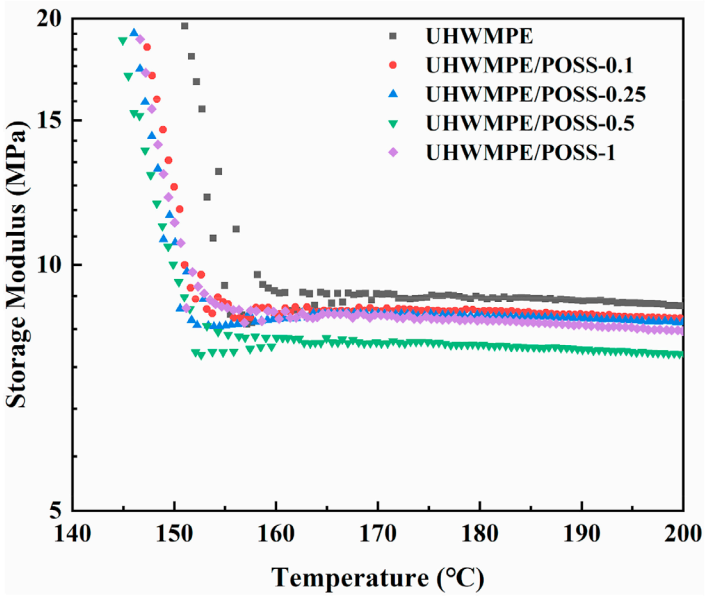

Figure 4. Storage modulus of ultra-high molecular weight polyethylene (UHMWPE) loaded with octamethyl-POSS, displaying apparent disentanglement. Reprinted from Zhang, X.; Zhao, S.; Xin, Z. The Chain Dis-Entanglement Effect of Polyhedral Oligomeric Silsesquioxanes (POSS) on Ultra-High Molecular Weight Polyethylene (UHMWPE). Polymer 2020, 202, 122631. Copyright 2020, with permission from Elsevier.[78]

Furthermore, the presence of weakly interacting fillers, including C_{60}, can often lead to reductions in viscosity, which is often justified in reference to a decrease in density (i.e. an increase in free volume) for the matrix polymer at the nanofiller surface.[79–82] However, given the small magnitude of these effects alongside the low achievable filler loadings (~1 wt%), it is difficult to rigorously test a molecular-scale understanding of these materials. Work presented in Chapter 3 will explore the distinction between the rheological disentanglement phenomena observed in these types of weakly interacting systems contrasted with the rheology of strongly interacting (hydrogen-bonding) systems.

1.4 – Conclusion

This Dissertation presents work that furthers the understanding of the glass transition and rheology of polymer/POSS nanocomposites, and polymer nanocomposites

more generally, as well as methods that are potentially useful for their study. Chapter 2 presents work which systematically studies the effects of polymer and POSS functionality on T_g. These results can be interpreted either via a molecular mixture perspective, or via a variety of active theories of the glass transition. Chapter 3 aims to showcase findings which distinguish between the conflicting definitions of disentanglement in the POSS nanocomposite literature, in particular, the difference between a) the decreasing plateau modulus observed in weakly interacting polymer/POSS composites and b) the decreasing width of the entanglement plateau in strongly attracting systems. Chapters 4 and 5 give overviews of the use of dielectric relaxation spectroscopy and fluorescence microscopy as analytical tools to study nanocomposites and polymer systems more generally, while highlighting particular pitfalls associated with their use and interpretation. Finally, Chapter 6 presents a viewpoint on opportunities and future directions illuminated by this work in the broader field of polymer nanocomposite dynamics.

CHAPTER 2

2 – RATIONALIZING THE COMPOSITION DEPENDENCE OF GLASS TRANSITION TEMPERATURES IN POLYMER/POSS COMPOSITES

2.1 – Introduction

The glass transition temperature (T_g) is among the most important physical properties of polymers in myriad applications. Whether above or below T_g the distance between operating temperature and T_g determines the suitability of polymers and their composites in applications. Though the effects of POSS loading on polymer T_g are extensively studied, a general understanding of this behavior which accounts for the composition of the polymer and the POSS has only recently begun to emerge.[59,70] Polymer/POSS nanocomposites have shown a variety of effects on T_g, including the broadening of the transition region,[10] and either enhancement or suppression of T_g, depending on the chemical structure of the polymer and POSS.[59,70] In strongly interacting systems, polymer-POSS interactions can increase T_g by up to 35 K,[10,70] while some POSS fillers can also greatly reduce T_g by as much as ~100 K, despite the presence of strong polymer-POSS interactions.[83,84] Predicting the T_g of nanocomposites remains challenging due to the complexity introduced by polymer/filler interfaces not captured by current models.[85]

Overall, there remains a gap of knowledge to justify T_g change with composition when the POSS component does not undergo glass transition, which can be addressed by rationalizing the fitting parameters of the forementioned equations according to molecular-level understanding. To address this, experiments are presented in this Chapter which probe the role of polymer-POSS interactions on T_g (Figure 5). First, a random copolymer of styrene and 2-vinylpyridine (2VP) loaded with OAPS is used, because the monomers have similar size and their homopolymers have nearly identical T_g, so any T_g change between nanocomposites with the same OAPS loading must be due to the presence of 2VP-OAPS interactions. Next, a P2VP homopolymer is loaded with molecules with variable amine functionalization on the phenyl rings. Using these results, an empirical method for rationalizing T_g change in polymer-POSS composites is presented.

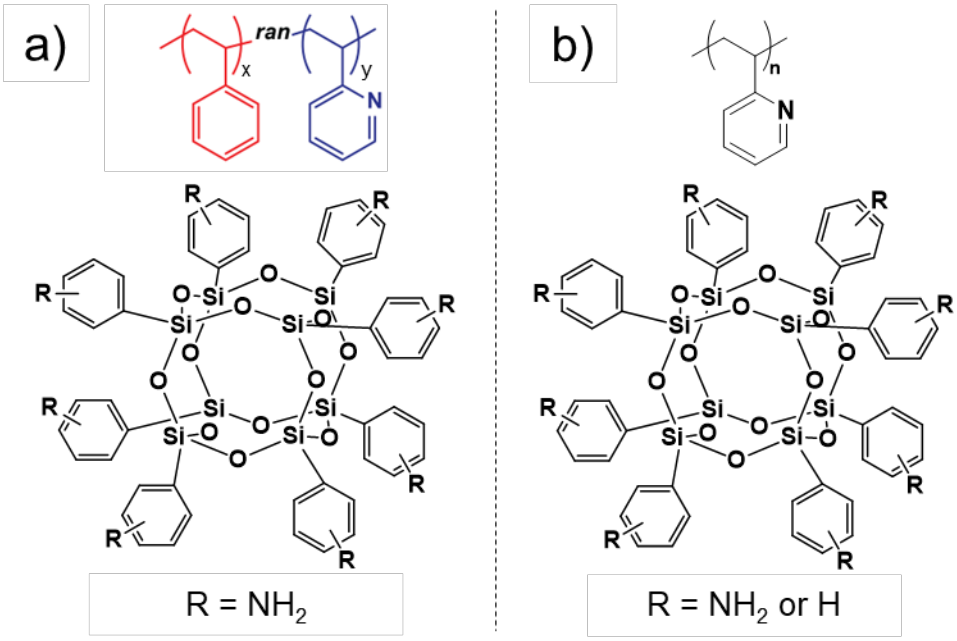

Figure 5. Illustrations of a) the random copolymer composites and b) the variably functionalized POSS composites presented in this Chapter.

2.2 – Methods

2.2.a – Materials

Hexanes, methanol, ethyl acetate, petroleum ether, fuming nitric acid, magnesium sulfate, ferric chloride, and Celite® 545 were purchased from Fisher Scientific (Waltham, MA, USA). Azobisisobutyronitrile (AIBN) and tetrahydrofuran (THF) were purchased from Alfa Aesar (Haverhill, MA, USA). Styrene, 2 vinyl-pyridine, basic alumina, calcium hydride and hydrazine hydrate were purchased from Acros Organics (Fair Lawn, NJ, USA). Octaphenyl silsesquioxane was purchased from Hybrid Plastics (Hattiesburg, MS, USA). Octa(aminophenyl) silsesquioxane was purchased from Gelest Inc. (Morrisville, PA, USA) and also synthesized in house. Ethyl 2-(phenylcarbonothioylthio)-2-phenylacetate was purchased from Sigma-Aldrich (St. Louis, MO, USA). AIBN was recrystallized in methanol. Styrene and 2-vinyl pyridine were purified by passing through a column of basic alumina to remove inhibitor. Anisole was dried over calcium hydride. All other materials were used as received.

2.2.b – Nuclear Magnetic Resonance (NMR) Spectroscopy

NMR measurements were taken on a Bruker 500 500 MHz NMR instrument with cryoprobe attachments. Carbon NMR measurements of polymers were performed in chloroform-*d* at concentrations of 50 mg/mL, while all other NMR measurements were performed in acetone-d_6 at concentrations of 50 mg/mL.

2.2.c – Gel Permeation Chromatography (GPC).

The molar mass and dispersity of P(S-2VP) copolymers synthesized were characterized via GPC in a mobile phase of dimethyl formamide (DMF) with 0.01 M lithium chloride salt at 50 °C relative to polystyrene standards. The GPC instrument consisted of an Agilent Technologies 1260 Infinity, fitted with a Gel 5 μm guard column, a PL Gel 5 μm mix D 1° column, and a PL Gel 5 μm Mix C 1° column. Samples were run at a flow rate of 1 mL/min, using toluene as the flow rate marker.

2.2.d - Attenuated Total Reflection Fourier-Transform Infrared Spectroscopy (ATR-FTIR)

FTIR measurements were taken on a PerkinElmer Spectrum One. High temperature measurements were performed using a DiaMax diamond ATR accessory under nitrogen atmosphere.

2.2.e – Nanocomposite Sample Preparation

Nanocomposites were prepared by co-casting following modified literature procedures.[5,10] Total 2 g of P(S-2VP) and OAPS were dissolved in 10 mL of THF at different weight ratios. Solvent was allowed to evaporate overnight at room temperature and atmospheric pressure, before being placed in a vacuum oven <100 mTorr at 180 °C for 36 hours to remove all remaining solvent. The samples, which were a red-orange powder, were melt casted in polytetrafluoroethylene lined washers in a vacuum oven at 180 °C for 18 hours. After annealing, the samples were either glassy, red, and optically transparent, or powdery, orange, and optically opaque, depending on the dispersion of OAPS.

2.2.f – Scanning Electron Microscopy (SEM)

Electron microscopy imaging was performed on a FEI-Magellan 400 SEM. Nanocomposite samples were drop cased from concentrated solutions onto silicon wafers and annealed under vacuum at 180 °C for 36 hours prior to imaging.

2.2.g – X-Ray Scattering

Scattering measurements were performed on a SAXSLAB GANESHA small/wide-angle X-ray scattering instrument. The source was Cu Kα 0.154 nm with a beam area of approximately 0.1 mm^2. All measurements were performed in transmission geometry on a nanocomposite powder sample 1 mm thick, between layers of polyimide tape. Results are reported as relative intensities on an arbitrary scale. SAXS measurements were acquired over 10 minutes, while WAXS measurements were acquired over 1 minute.

2.2.h – Differential Scanning Calorimetry (DSC)

Heat capacity versus temperature measurements were taken on a TA Instruments Q20 Differential Scanning Calorimeter at a heating/cooling rate of 10 K/min under nitrogen. T_g is reported as the midpoint of the heat capacity inflection point upon second heating. Typical sample weights were ~2 mg.

2.2.i – Electrospray Ionization Mass Spectrometry (ESI-MS).

Electrospray ionization time of flight mass spectrometry was performed on a Bruker MicroTOF ESI-TOF Mass Spectrometer at the University of Massachusetts Mass Spectrometry Core Facility. POSS samples were diluted to ~10 μM with 1mM formic acid in an acetonitrile/water (80:20 by weight) solution before injection.

2.2.j – Molecular Dynamics Simulations.

Coarse grained simulations were performed by Rui Shi at Jinlin University, while all-atom molecular dynamics simulations were performed by Xiang-Meng Jia at Jinlin University. Details regarding these simulations can be found in our published work.[71]

2.3 – Synthesis of Polymer and Nanofiller with Varying Number of Interacting Groups

2.3.a – Synthesis of Statistical Copolymers of Styrene and 2-Vinyl Pyridine (P(S-*r*-2VP))

The statistical copolymers of 2VP and styrene used in this model system were synthesized by reversible addition-fragmentation chain-transfer (RAFT) polymerization (Scheme 1).[86]

Scheme 1. Polymerization of random copolymers via reversible addition-fragmentation chain transfer polymerization.

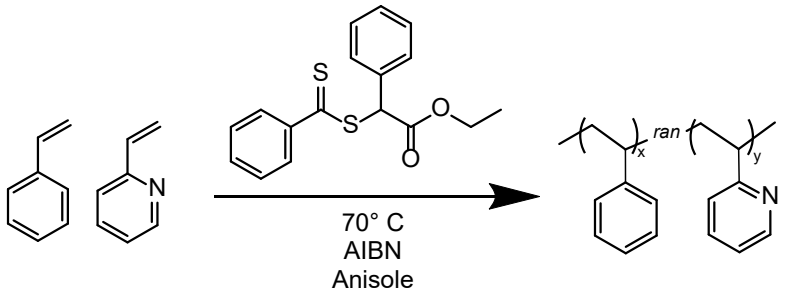

Total 20 g of styrene and 2 vinyl-pyridine were added to a 250 mL round bottom flask at different molar ratios, with 15 mL of anisole. Ethyl 2-(phenylcarbonothioylthio)-2-phenylacetate was used as the RAFT chain transfer agent (CTA), with azobisisobutyronitrile (AIBN) as the initiator. Reagents were added at a 600:4:1 molar ratio of monomers to CTA to AIBN. The reaction was degassed with nitrogen for 30 minutes and then heated to 70 °C for 18 hours, before quenching at 0 °C for 30 minutes and

precipitating in hexanes three times. Typical yield was ~40%, due to the difficulty of recovering the low molar mass polymers on precipitation. The pink powder was dried under reduced pressure at 80 °C for 24 hours and characterized by NMR (Figure 6) and THF gel permeation chromatography (GPC), relative to PS standards (Figure 7).

The fraction of 2-vinyl pyridine (2VP) monomer in the copolymer was calculated based on the integration values of the aromatic regions. The peak at 8.4 ppm corresponds to a proton alpha to the nitrogen in the pyridine ring, which is not present in styrene. A representative example of an NMR spectrum of the copolymers synthesized is shown in Figure 6.

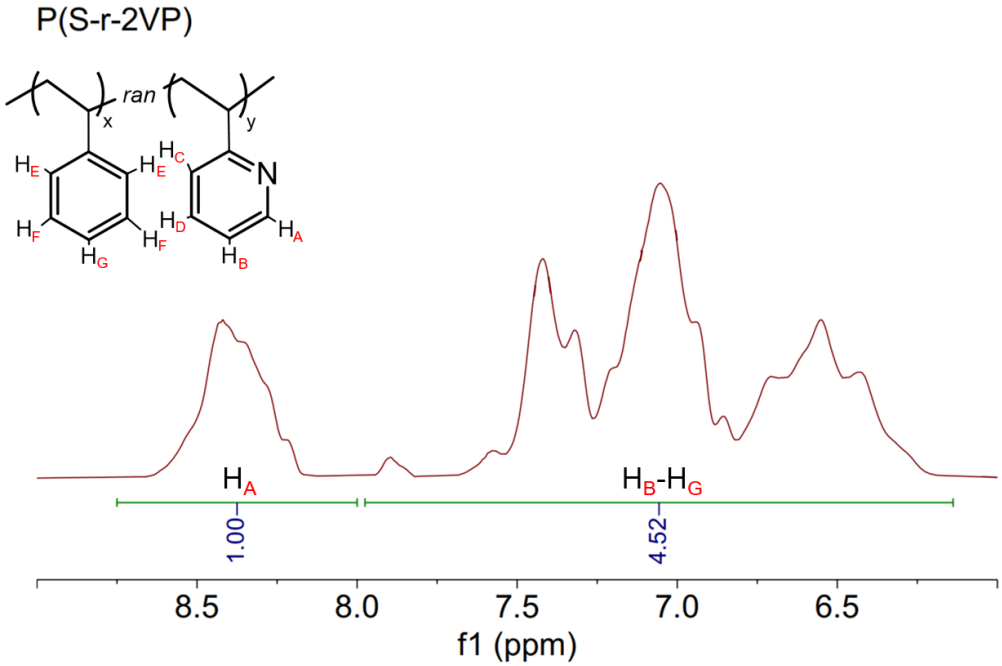

Figure 6. Representative example of proton NMR of a P(S-*r*-2VP), in this case targeting 75% 2VP monomer content. Integrations are used to calculate the relative incorporation of the two monomers.

As shown in Table 1, all copolymers used for the creation of P(S-*r*-2VP)/OAPS composites were unentangled ($M_n \approx 15$ kDa, versus $M_e \approx 30$ kDa)[29] with relatively low dispersity ($Đ < 1.2$), characterized by GPC with dimethylformamide mobile phase relative to PS standards. The polymers have reasonable dispersity for RAFT polymerizations with

$Đ$ < 1.2, although the f_{2VP} = 0.77 copolymer has some relatively high molar mass contamination. This is also summarized in Table 1.

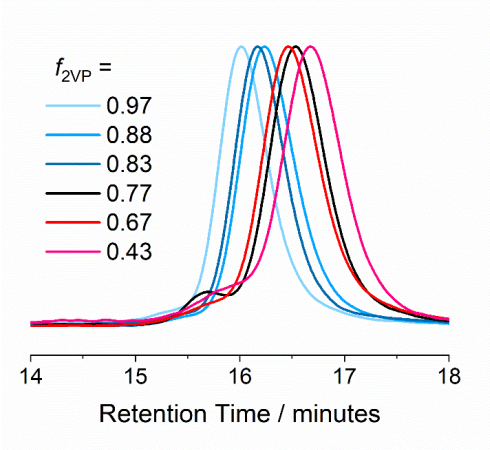

Figure 7. GPC trace of the P(S-*r*-2VP) copolymers with DMF mobile phase.

Table 1. P(S-2VP) Copolymer compositions used for the creation of P(S-*r*-2VP)/OAPS composites by NMR and molar mass relative to polystyrene by GPC.

f_{2VP} (feed)	f_{2VP} (measured)	M_n (kDa)	$Đ$
1	0.97	16	1.13
0.95	0.88	13	1.10
0.85	0.83	14	1.11
0.75	0.77	11	1.15
0.60	0.67	11	1.16
0.40	0.43	10	1.15

To determine whether blocky sequences were formed during the RAFT polymerization, two polymers were synthesized. A copolymer with f_{2VP} = 0.55 was studied with carbon NMR, in comparison to P2VP and PS homopolymers, as shown in Figure 8. Sharp peaks are observed in the homopolymer spectra, corresponding to specific tacticity sequences in the neighboring repeat units in the polymer. In contrast, the peaks are not sharp in the copolymer, suggesting that the number of distinct combinations of neighboring repeat unit identities (i.e., S or 2VP) and tacticities are too large to resolve. This indicates that there are no substantial blocks of either monomer in the polymer. Note that the solvent peaks are sharp in all spectra, thus the broadening cannot be due to poor shimming.

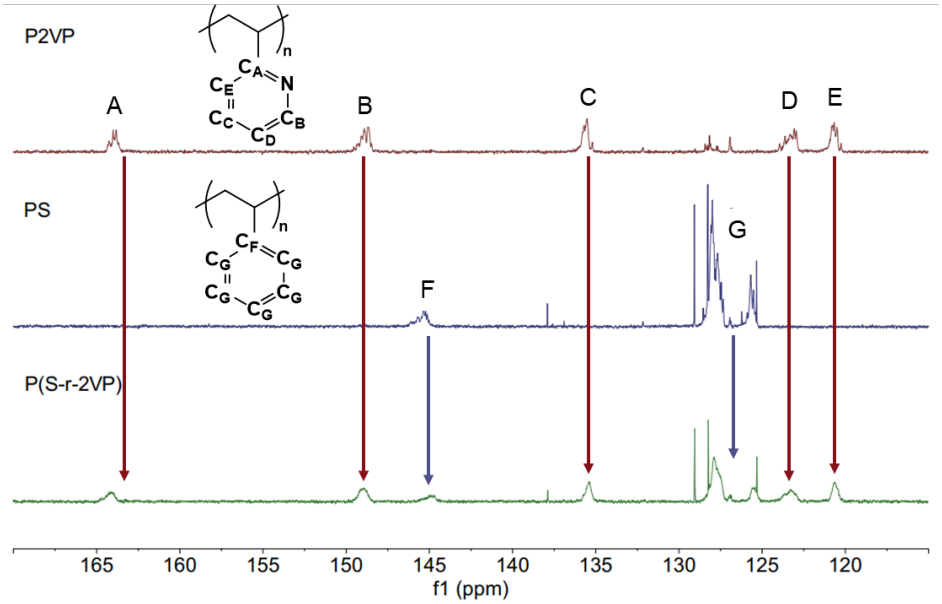

Figure 8. ^{13}C-NMR of P2VP and PS homopolymers, compared to 55% 2VP copolymer, in $CDCl_3$.

Copolymerization via RAFT can produce gradient copolymers when there is a substantial difference in the reactivity ratios of the components, which would not be desirable in this case. To check for this possibility, aliquots were taken during reaction for two copolymers. Based on ^{1}H NMR, the feed mole fraction and measured mole fraction of 2VP (f_{2VP}) in the copolymer are in reasonable agreement (Figure 9a), and no monomer drift is observed during the reaction, which reached completion at around 6 hours (Figure 9b). No polymer precipitated out before a reaction time of greater than 1 hour, indicating that the polymerization had not proceeded substantially before data could be collected. Similarly, the molar mass measured by GPC at 2 hours may be skewed to higher values due to the very low molar mass chains not precipitating out of solution.This provides further evidence that the sequence distribution in the copolymer is effectively random.

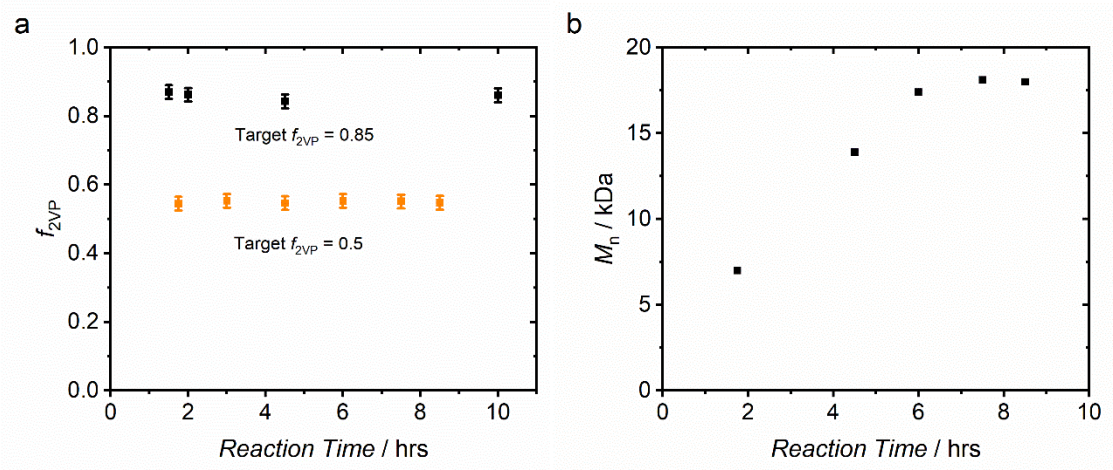

Figure 9. a) Fraction of 2VP incorporated in copolymers over time, measured via ^{1}H-NMR of aliquots during the reaction. Monomer composition is constant within error, during reaction, indicating that monomer drift is inconsequential during the polymerization of styrene and 2VP via RAFT. b) DMF GPC molar mass of the f_{2VP} = 0.5 polymer relative to polystyrene standards, indicating that the reaction reached completion near 6 hours.

2.3.b – Synthesis of Variably Aminated Octaphenyl Silsesquioxane (NH_2-OPS)

Aminated octaphenyl silsesquioxane (NH_2-OPS) with variable numbers of amines per POSS (n_{amine}) was synthesized according to modified literature procedure (Scheme 2).[87] Typical yield was ~80% for the nitration, and ~60% for the reduction step.

Scheme 2. Reaction scheme of NH_2-OPS with variable amine functionality

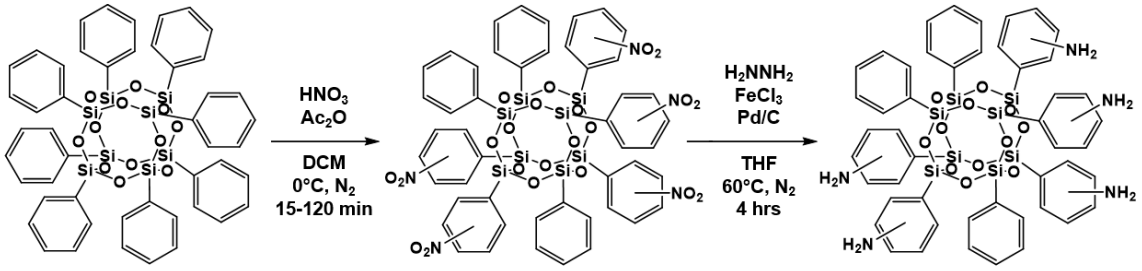

Nitric acid at 90 wt% in water and acetic anhydride were added from separate addition funnels dropwise to a dispersion of OPS in dichloromethane, with a 5-gram basis of OPS. The reaction flask was kept at 25 °C for times ranging from 15 to 180 minutes, after addition of reagents over 5 minutes. The different reaction times correspond to the

extent of nitration of OPS. When the concentration of nitric acid was larger than 90 wt%, an unwanted reaction occurred which produced a gummy yellow material upon drying. An example of the ^{1}H-NMR spectrum of this material is shown in Figure 10, potentially indicating the presence of an undesirable polymerized byproduct. To avoid this product from forming, the concentration of nitric acid in water was controlled by measuring the density and diluting to 90 wt%.

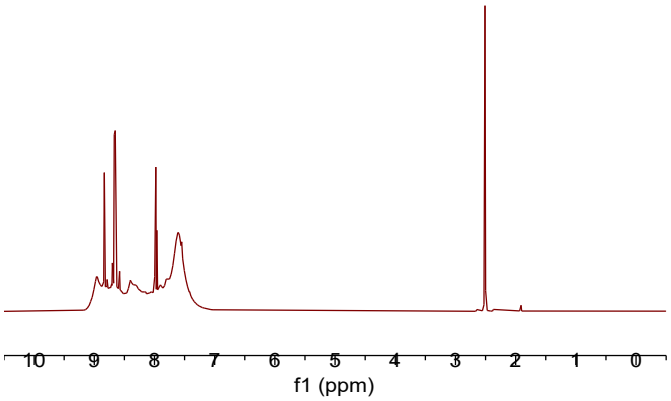

Figure 10. ^{1}H-NMR in DMSO-d_6 of product from unsuccessful ONPS synthesis with higher nitric acid concentration.

The resultant NO_2-OPS (denoted as ONPS at 100% reaction extent) produced by the synthesis with 90 wt% nitric acid was precipitated from the reaction solution in cold water, before evaporating off the dichloromethane. The solid product was collected via vacuum filtration and rinsed thoroughly with concentrated sodium bicarbonate solution and water and characterized by NMR (representative example shown in Figure 11). It is in principle possible to measure the functionality of the NO_2-OPS from this spectrum,[87] however, this analysis is highly multivariate and sensitive to error.

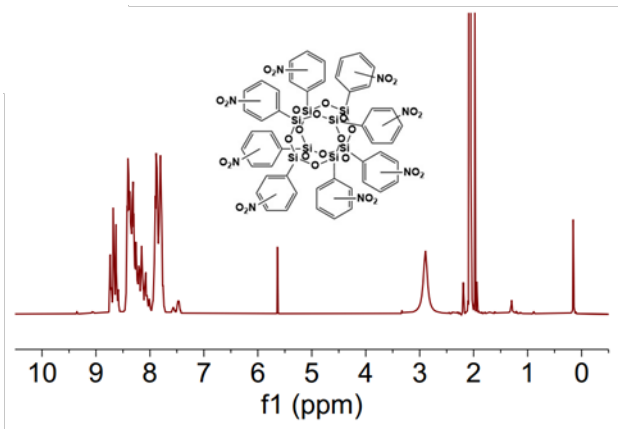

Figure 11. Proton NMR spectra in acetone-d_6 of the partially nitro-functionalized OPS (NO_2-OPS) intermediates used to synthesize NH_2-OPS from OPS.[88]

The product was then dissolved in tetrahydrofuran and precipitated into methanol, before drying. NO_2-OPS was reduced to NH_2-OPS (denoted as OAPS at 100% reaction extent) with hydrazine hydrate as an *in-situ* hydrogen source with ferric chloride catalyst, 5% Pd/C catalyst, and tetrahydrofuran solvent reflux at 60 °C, according to literature procedures. Fourier transform infrared spectroscopy (FTIR) results are shown for the fully reacted ONPS and OAPS samples of samples is shown in Figure 12. The OAPS molecule shows the N-H stretching of the amine group around 3300 cm^{-1}, and the disappearance of nitro groups at ~1550 and ~1350 cm^{-1}.

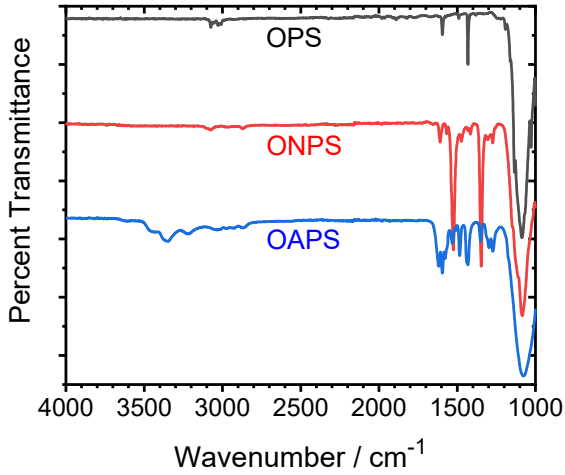

Figure 12. FTIR spectra of OPS, ONPS, and OAPS, corresponding well to the peak assignments by Tamaki *et al.*[44] to confirm the reaction was successful. Transmittance is shifted vertically for clarity and presented on a scale 20% per tick.

The experimentally achievable range of the number-average number of amines ($\langle n_{amine} \rangle$) was 5.7 to 7.3, as measured by electrospray ionization (ESI-MS) mass spectrometry (Figure 13, Figure 14, and Figure 15). The lower limit of n_{amine} was determined by the limited solubility (low functional POSS was insoluble in all tested solvents and could thus not be separated from the Pd/C catalyst). ESI-MS revealed the exact distribution of molecular POSS species with different numbers of amines from which the number average in each sample was calculated. This distribution was sharpest for samples with high $\langle n_{amine} \rangle$, and considerably broadened as $\langle n_{amine} \rangle$ decreased across samples. The values of $\langle n_{amine} \rangle$ obtained from ESI-MS agreed reasonably well with that from proton nuclear magnetic resonance (^{1}H-NMR) (Figure 16), however, the value determined by NMR is typically lower than measured by ESI-MS, presumably due to proton exchange with the NMR solvent ($CDCl_3$) by the amine protons. For this reason, the value measured by ESI-MS was used for all further analysis.

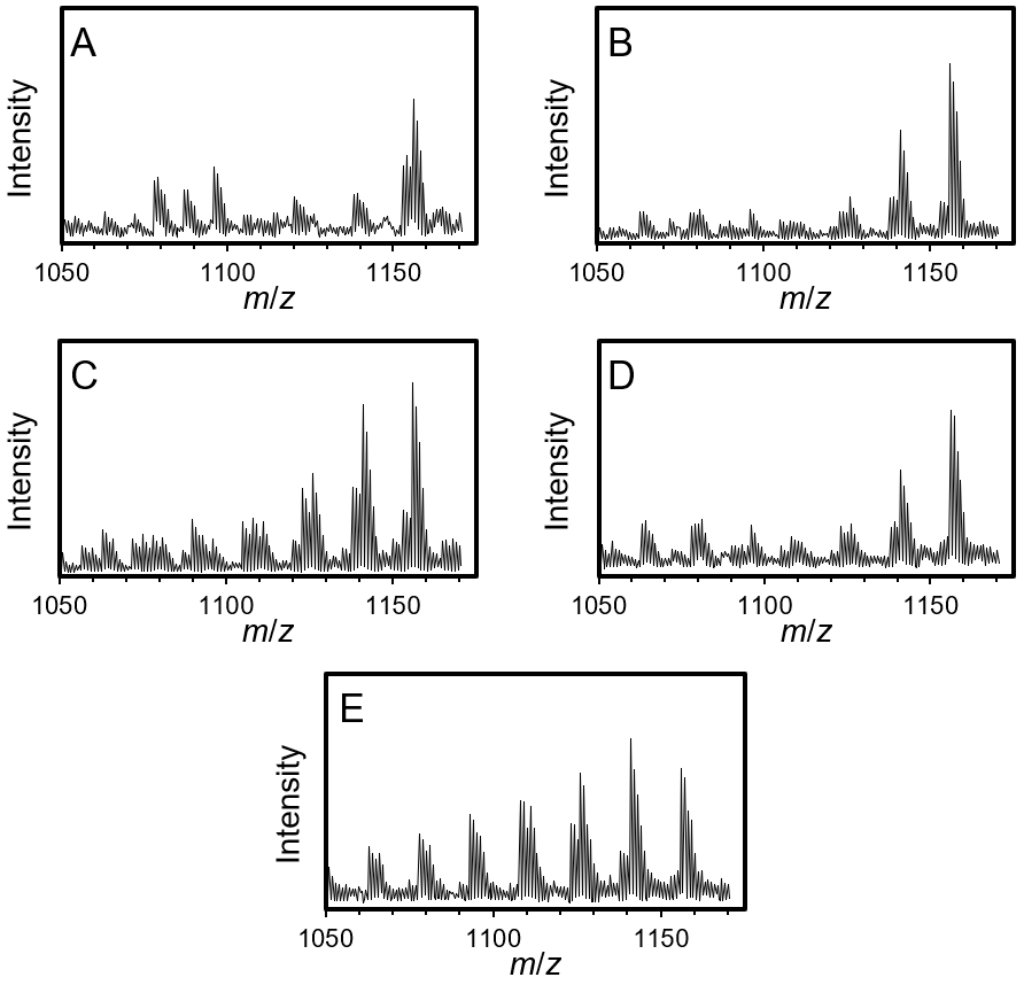

Figure 13. ESI-MS spectra corresponding to different NH_2-POSS samples synthesized. a) (n_{amine}) = 7.3, b) (n_{amine}) = 6.7, c) (n_{amine}) = 6.3, d) (n_{amine}) = 6.2, and e) (n_{amine}) = 5.7.

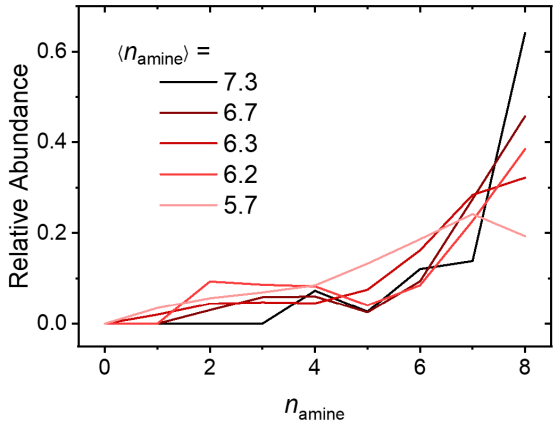

Figure 14. Distribution of number of amines (n_{amine}) in the different NH_2-OPS products measured by ESI.

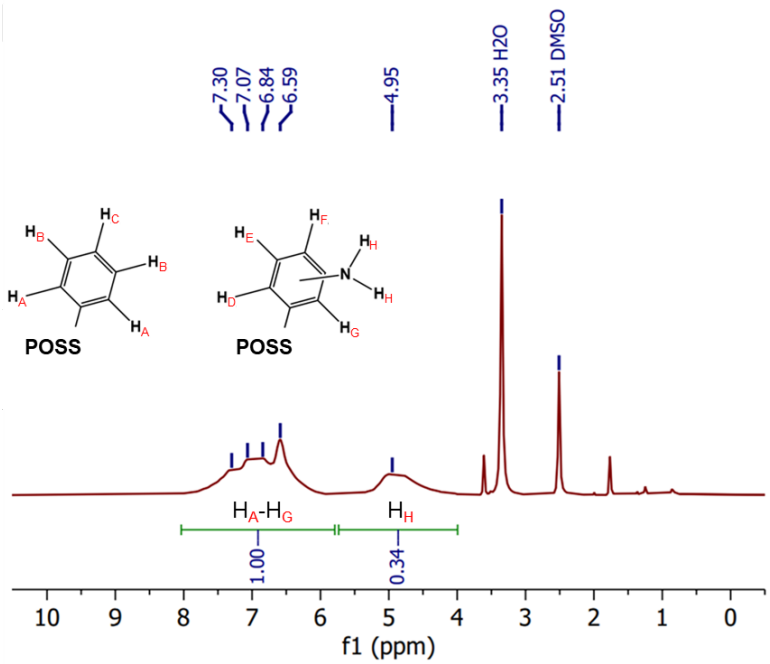

Figure 15. ^{1}H NMR spectra of the different NH_2-OPS used in this study. The ratio of phenyl ring protons at 8-6 ppm to amine protons at 5.5-4 ppm is used to calculate the value of $\langle n_{amine} \rangle$.[88]

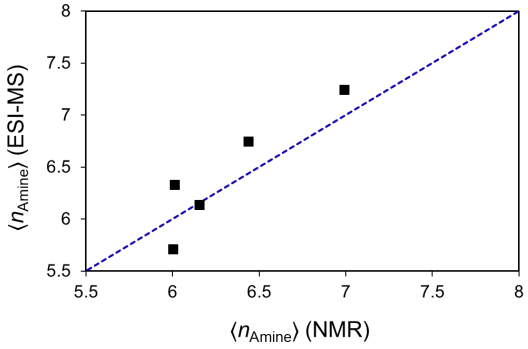

Figure 16. Comparison of the number average number of amines on each NH_2-POSS sample by ESI and ^{1}H-NMR. As expected, ^{1}H-NMR underestimates the number of amines due to proton exchange with the deuterated solvent.

2.4 – Phase Diagram of Dispersed/Aggregated POSS in Polymer Matrix

2.4.a – Scattering and Visual Inspection

To verify homogeneous OAPS distribution in the polymer matrix, optical examination, small-angle X-ray scattering (SAXS), and wide-angle X-ray scattering (WAXS) was performed. After solvent casting, the nanocomposite samples were found to

be either glassy and transparent due to well-dispersed OAPS, or powdery and opaque due to aggregated OAPS (Figure 17). Scanning electron microscopy showed no visible aggregates for these samples, confirming uniformly dispersed OAPS.

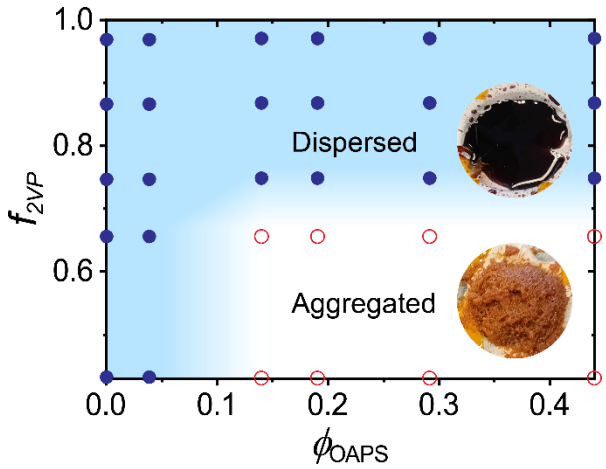

Figure 17. Phase diagram of nanocomposite state with f_{2VP} - ϕ_{OAPS} from visual inspection, SAXS, and WAXS. Inset pictures of glassy (top right circle) and aggregated (bottom right circle) nanocomposites. Red color of composites is from RAFT end-groups.

The appearance-based categorization of the OAPS dispersion is further supported by SAXS and WAXS. The SAXS curve followed q^{-3} scaling in the low q regime (Figure 18), consistent with previous reports on well-dispersed samples of polymer/POSS composites.[10,89] The physical origin of the –3 slope remains controversial but is potentially due to crazing or air bubbles in the polymer matrix.[89] WAXS measurements agree with this trend, as the peak at 0.5 $Å^{-1}$ corresponding to OAPS-OAPS spacing in OAPS clusters is negligible (Figure 19). Based on the composite composition screening, all further experiments were performed on the well-dispersed samples, i.e., $f_{2VP} \geq 0.77$ and weight fraction of OAPS (w_{OAPS}) ≤ 0.5.

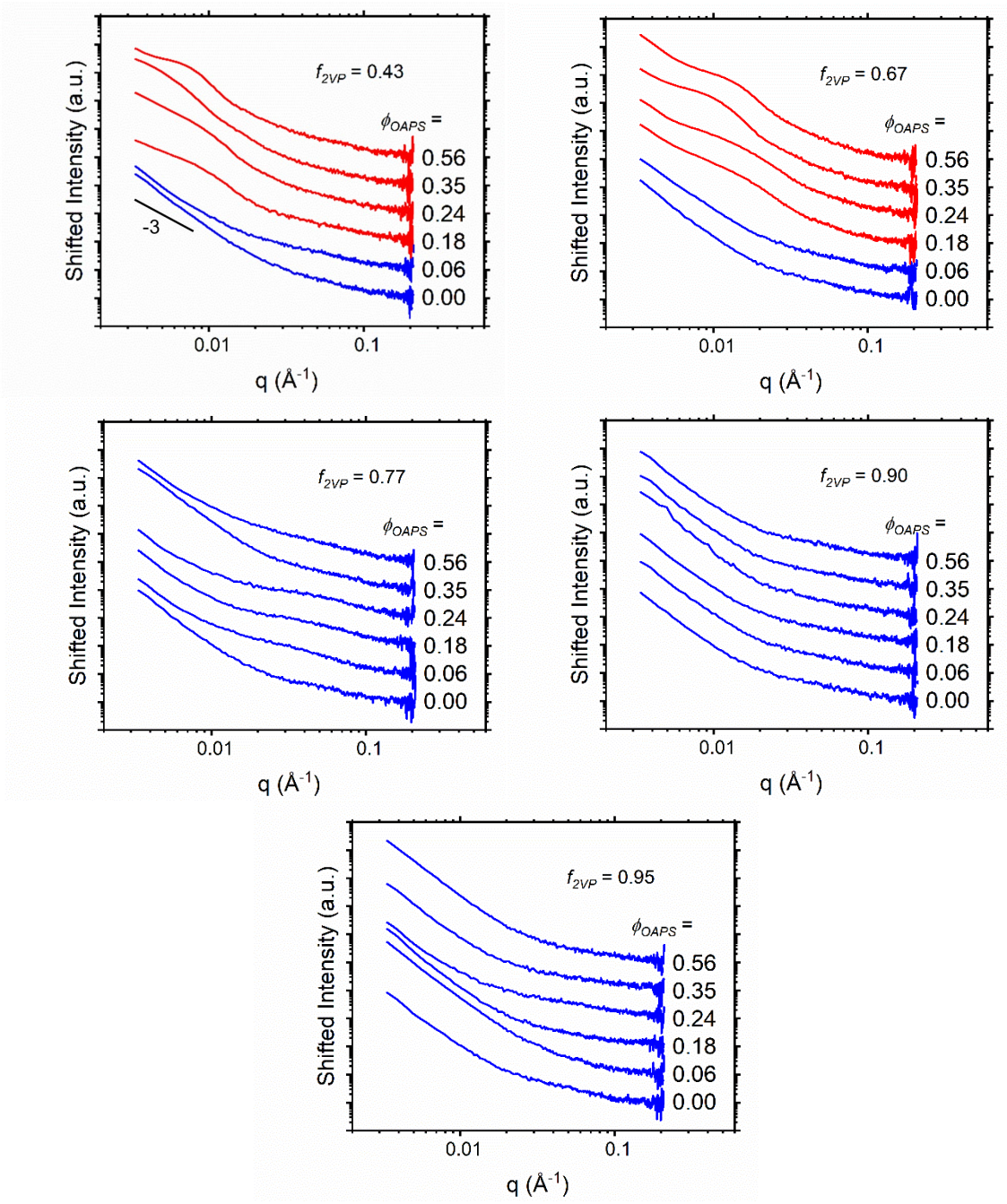

Figure 18. Set of SAXS data collected for P(S-2VP)/OAPS nanocomposites. Red dashed lines correspond to aggregated samples, while blue lines correspond to well-dispersed samples by visual inspection. Curves are shifted vertically on a logarithmic scale for clarity.

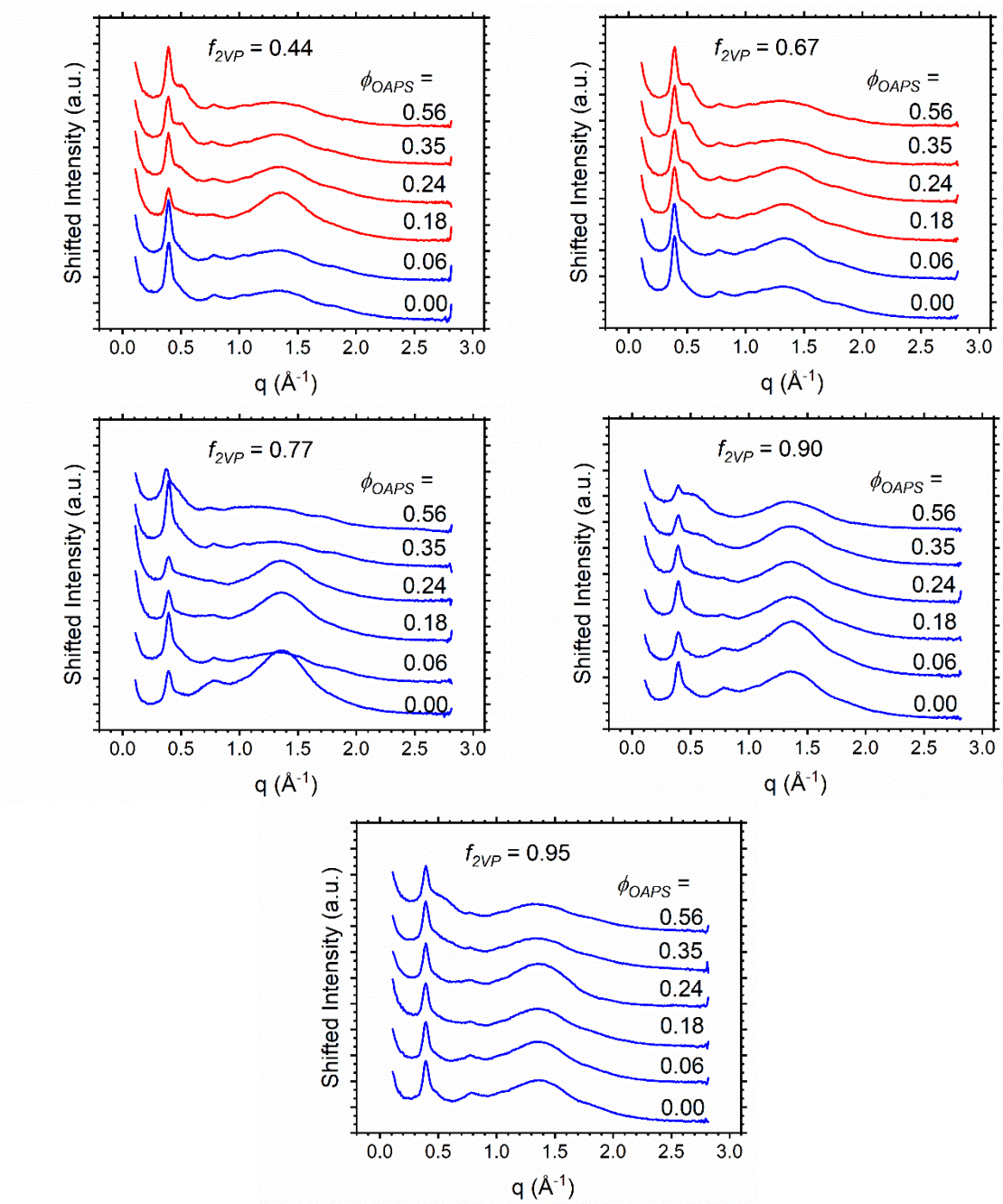

Figure 19. Wide-angle X-ray scattering scans of nanocomposites. Red lines correspond to aggregated samples, while blue lines correspond to well-dispersed samples by visual inspection. The peak at 0.5 Å^{-1} corresponds to OAPS-OAPS spacing in aggregates. The peak at 0.4 Å^{-1} comes from the polyimide sample holder, and the peak at 1.4 Å^{-1} comes from the amorphous halo of P2VP. Curves are shifted vertically on a linear scale for clarity.

SEM was used to attempt to observe OAPS aggregates in samples. Optically transparent samples were dissolved in THF and drop-casted on silicon substrates. No features were observed on any samples on resolutions down to approximately 10 nm.

2.5 – Changes in Glass Transition Temperature with Polyhedral Silsesquioxane Loading and Composition in P(S-*r*-2VP)/OAPS

The glass transitions of the well-dispersed composites were examined by differential scanning calorimetry (DSC), as summarized in Figure 20.

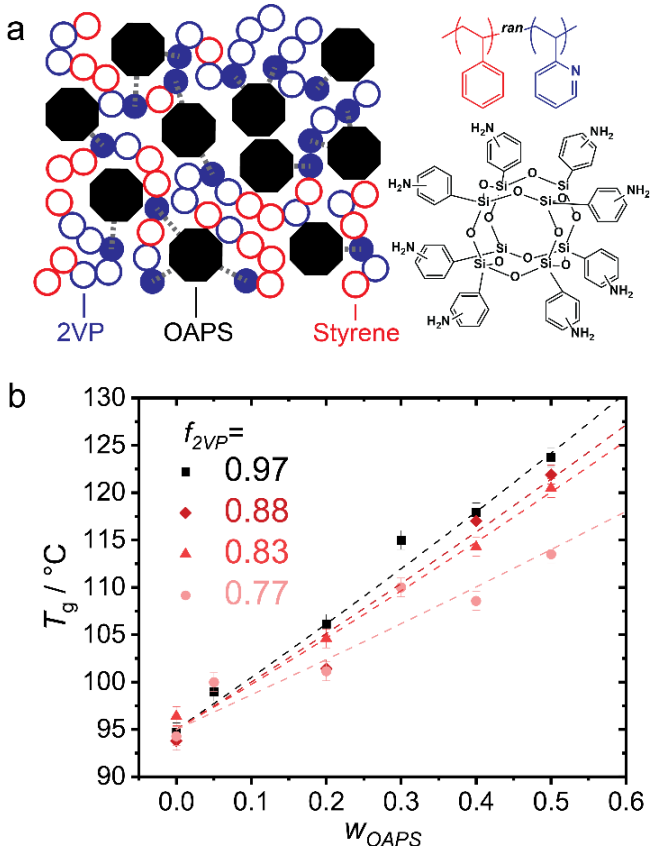

Figure 20. a) Schematic of P(S-2VP)/OAPS composite and chemical structures where closed and open circles represent "bonded" and "unbonded" monomers, respectively. b) Midpoint T_g versus OAPS weight fraction in nanocomposites measured by DSC. Error bars indicate instrumental uncertainty of ± 2 °C. Dashed lines are fitted to the conventional Fox equation assuming a two-component system of polymer and OAPS.

In agreement with literature,[5,10] the midpoint T_g measured with a heating rate of 10 K/min increases by 25 °C for the highest OAPS weight fractions (w_{OAPS} = 0.50) and 2VP mole fractions (f_{2VP} = 0.97). The T_g of unloaded samples (w_{OAPS} = 0) is independent of f_{2VP} because PS and P2VP have identical T_g. In contrast, the T_g of loaded samples increases with increasing f_{2VP} due to hydrogen bond formation, highlighting that the attractive interactions increase T_g, and thus slow down the segmental dynamics.

2.5.a – Rationalizing T_g Change with Fox Equation Framework

The conventional Fox equation cannot fully explain the effects of both f_{2VP} and w_{OAPS} on the T_g of the composites (Figure 20 dashed fitting lines). In Equation 2.1, we treat component A as P(S-*r*-2VP) and component B as OAPS, and $T_{g,mix}$ as the experimentally obtained T_g of composites.

$$\frac{1}{T_{g,mix}} = \frac{w_A}{T_{g,A}} + \frac{w_B}{T_{g,B}} \quad 2.1$$

Here, $T_{g,OAPS}$ is a fitting parameter because OAPS does not undergo any thermal transitions observable by DSC in the range from –20 to 270 °C.[10] Although these fits to the conventional Fox equation describe the data reasonably, the fitted values of T_g of OAPS ($T_{g,OAPS}$) lack physical significance, considering there is no thermal transition in the given temperature range. Furthermore, this analysis does not explain the increase in $T_{g,OAPS}$ from 135 °C to 158 °C with increasing f_{2VP}, suggesting that a revised model for this system must take both w_{OAPS} and f_{2VP} into account to fully capture the observed behavior.

We hypothesize that the effects of f_{2VP} and w_{OAPS} on composite T_g can be explained using a Fox Equation with two components of "bonded" (2VP hydrogen-bonded with OAPS) and "unbonded" monomers (unbonded 2VP and styrene) (Figure 20a), rather than

treating OAPS as a blend component. In this analysis, we assume that the bonded components are hydrogen-bonded 2VP monomers, whereas the unbonded components are styrene and unbonded 2VP monomers (Equation 2.2). These unbonded monomers are considered identical because of the indistinguishable T_g and similar chemical structure of PS and P2VP. Another assumption is that the components of the composite were randomly distributed without substantial changes to chain conformations, which is reasonable based on molecular dynamics simulations[90] and neutron scattering experiments on other POSS composites.[89] In this analysis, the T_g of a hypothetical polymer that has each monomer bonded to an OAPS amine group is given as $T_{g,bonded}$.

$$\frac{1}{T_{g,composite}} = \frac{w_{bonded}}{T_{g,bonded}} + \frac{1 - w_{bonded}}{T_{g,neat}} \quad 2.2$$

To test our hypothesis, weight fraction w_{bonded} needs to be correlated with the composition of the composites. We derived the w_{bonded} based on the stoichiometry of amines of OAPS and nitrogen lone pairs in 2VP as $w_{bonded} \cong z_{OAPS} \cdot \left(V_{M,monomer}/V_{M,OAPS}\right) \cdot p_{bond} \cdot f_{2VP} \cdot \phi_{OAPS}$, where $V_{M,monomer}$ and $V_{M,OAPS}$ are the molar volume of a monomer and OAPS, z_{OAPS} is the number of amines per OAPS (equal to 8), p_{bond} is the probability of forming a hydrogen bond between OAPS and 2VP when OAPS amine is surrounded by 2VP neighbors, and ϕ_{OAPS} is the volume fraction of OAPS in the composite. Note that $V_{M,monomer}$ is approximated as equal for styrene and 2VP and independent of OAPS loading. The fraction of monomers that are bonded, f_{bonded}, is calculated from stoichiometry and the composition of the system. We start by defining the number of bonded monomers per volume of composite as $n_{bonds,monomer}$ from the molar volume of a monomer as $V_{m,monomer}$, which is approximated as equal for styrene and 2VP and independent of OAPS loading (Equation 2.3).

$$n_{\text{bonds,monomer}} = \frac{(1-\varphi_{\text{OAPS}})}{V_{\text{m,monomer}}} f_{\text{bonded}} \quad (2.3)$$

The value of $n_{\text{bonds,monomer}}$ must equal the number of OAPS amines that are bonded to monomers, $n_{\text{bonds,OAPS}}$, assuming each amine can only form one hydrogen bond. The number of OAPS amines per volume, n_{amines}, is calculated as $n_{\text{OAPS}} = \left(\varphi_{\text{OAPS}}/V_{\text{m,OAPS}}\right) \cdot z_{\text{OAPS}}$ with the molar volume of OAPS, $V_{\text{m,OAPS}}$ and the number of amines per OAPS is denoted $z_{\text{OAPS}} = 8$. From n_{OAPS}, the number of amine-polymer bonds, $n_{\text{bonds,OAPS}}$ can be calculated as $n_{\text{OAPS}}(1-\varphi_{\text{OAPS}})\, f_{\text{2VP}}\, p_{\text{bond}}$, where p_{bond} is the probability of forming a hydrogen bond between OAPS and 2VP when OAPS amine is surrounded by 2VP neighbors. It is assumed that the components of the system are randomly distributed in space, so the fraction of volume surrounding an OAPS amine occupied by 2VP monomers is proportional to f_{2VP} and $(1 - \phi_{\text{OAPS}})$.

$$n_{\text{bonds,OAPS}} = \frac{\varphi_{\text{OAPS}}}{V_{\text{m,OAPS}}} z_{\text{OAPS}}(1-\varphi_{\text{OAPS}})\, f_{\text{2VP}}\, p_{\text{bond}} \quad (2.4)$$

Setting Equation 2.3 equal to Equation 2.4, an expression for f_{bonded} is derived. This mole fraction f_{bonded} is approximately equal to the weight fraction w_{bonded} because the difference between the molar mass of styrene and 2VP monomers are small (< 1%).

$$f_{\text{bonded}} = z_{\text{OAPS}} \frac{V_{\text{m,monomer}}}{V_{\text{m,OAPS}}}\, p_{\text{bond}}\, f_{\text{2VP}}\, \phi_{\text{OAPS}} \cong w_{\text{bonded}} \quad (2.5)$$

With these assumptions about the probability of a strong monomer-OAPS interaction, the Fox equation can predict the T_{g} of the composite.

Equation 2.2 is now rewritten as the modified Fox equation as Equation 2.6 and 2.7, where m is a material parameter for each composition.

$$\frac{1}{T_{\text{g,neat}}} - \frac{1}{T_{\text{g,composite}}} \cong m\, f_{\text{2VP}}\, \phi_{\text{OAPS}} \quad (2.6)$$

$$m = z_{\text{OAPS}} \frac{V_{\text{M,monomer}}}{V_{\text{M,OAPS}}} p_{\text{bond}} \left(\frac{1}{T_{\text{g,neat}}} - \frac{1}{T_{\text{g,bonded}}}\right) \quad (2.7)$$

The modified Fox Equation can explain the increase in T_g of the unentangled P(S-2VP)/OAPS as well as entangled P2VP/OAPS composites, demonstrating the universality of this approach. Our data for composites with variable f_{2VP} is plotted alongside literature data for P2VP homopolymer/OAPS composites in Figure 21, with a linear slope fitting Equation 2.6 with $m = 4.5 \times 10^{-4} \pm 0.1 \times 10^{-4}$ K^{-1} with R^2 of 0.99, indicating good agreement with our assumption that monomer-nanoparticle pairs are responsible for the dramatic increase in T_g observed in these systems. This value is used to construct the fitting lines shown in Figure 21b, alongside T_g data of our study ($M_n \approx 15$ kDa, $0.77 \leq f_{2VP} \leq 0.97$, $T_{g,neat}$ = 95 °C, blue triangles; DSC, heating), Cheng et al.'s study (M_n = 101 kDa, f_{2VP} = 1, $T_{g,neat}$ = 101 °C, light blue ×; DSC, heating),[10] and Bailey et al.'s study (M_n = 100 kDa, f_{2VP} = 1, $T_{g,neat}$ = 95 °C, green +; DSC, cooling).[5]

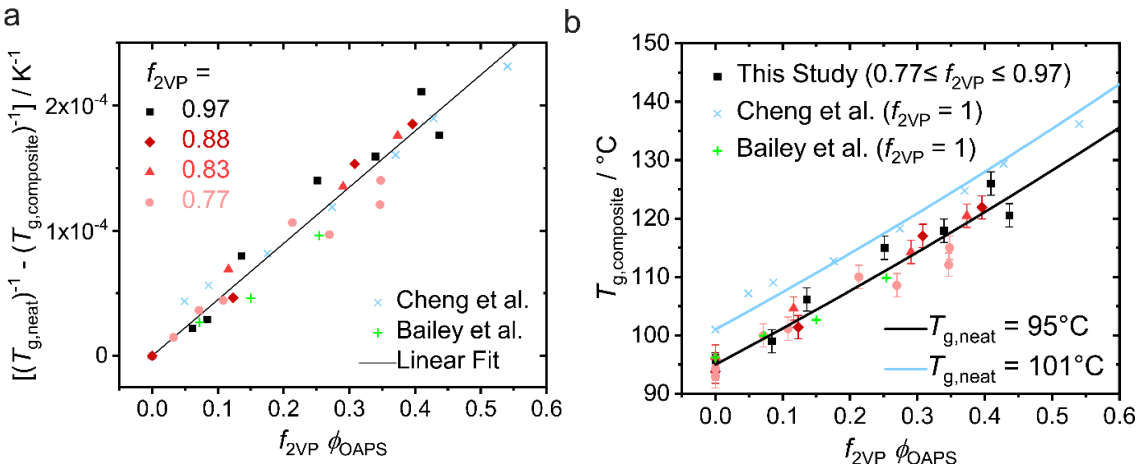

Figure 21. T_g data of our study (variable f_{2VP}, black and red filled symbols), Cheng et al.'s study (f_{2VP} = 1, light blue ×),[10] and Bailey et al.'s study (f_{2VP} = 1, green +).[5] a) Data for the three studies are linearized according to **Equation 2.6**, and fitted to determine the value of m equal to $4.5 \times 10^{-4} \pm 0.1 \times 10^{-4}$ K^{-1} with R^2 of 0.99. b) Our fitted model is shown versus measured T_g data on a linear axis as solid lines corresponding to the measured T_g of the neat polymer, $T_{g,neat}$.

The fitted value of m gives an empirical relationship between $T_{g,bonded}$ and p_{bond} because the other values in Equation 2.7 are known. The value of p_{bond} is estimated based on molecular dynamics simulations by Qian and coworkers,[71,90] due to the experimental

difficulty of measuring it directly, as will be discussed later in the Chapter. The value of p_{bond} near the T_g of the material is found to be to be ~0.6 from these simulations, yielding $T_{g,bonded} \approx 400$ °C, though this analysis should be considered an approximation due to the assumptions of the model. Also, Kuo et al. performed FTIR in a POSS blend system of phenolic resin loaded with octa(acetoxystyrl) POSS fille to obtain a p_{bond} value as high as ~0.7 in the dilute POSS limit,[84] indicating that the simulations are returning a reasonable value for a polymer/POSS composite with hydrogen bonding. Our derivation ignores the dynamic nature of hydrogen bonds and the interplay between temperature and bonding kinetics, interactions which may have a meaningful effect on the interpretation of $T_{g,bonded}$.

Our analysis can only be applied to "all-interfacial" systems where a ~1-2 nm filler such as POSS is well dispersed. When this assumption does not hold, predictions of the Fox equation and our model typically deviate near the composition at which POSS aggregates are first observed, as discussed later in the Chapter.[59,82,83,91] Also, our analysis is limited to amorphous systems, while significant numbers of POSS composites are semicrystalline.[43,59,78] Lastly, this analysis is more powerful to predict T_g over a wide range of w_{POSS}, approaching unity. In contrast, the classic Fox equation works well when the system lacks strong interactions between polymer matrix and POSS, such as hydrogen bonding. This result is also in qualitative agreement with theories which predict an approximately linear increase in T_g with number of interactions in a homogenous melt.[60–62]

2.5.a.i. – Extending Framework to Other Polymer-POSS Nanocomposites

The aforementioned polymer/POSS blend system of phenolic resin loaded with octa(acetoxystyrl) POSS fillers (Figure 23a) is found to satisfy these requirements for the

framework, but additional complexity is introduced because the POSS component has a measurable T_g. To account for this, we apply "a Fox equation within a Fox equation." As illustrated as a blue copolymer in Figure 23a, the parameter $T_{g,chain}$ is defined conceptually as the T_g of the hypothetical copolymer of "bonded" (closed circles) and "unbonded" monomers (open circles) where the fraction of these monomers depends on the loading of POSS. The blend of this copolymer with POSS is then treated with the Fox equation.

$$\frac{1}{T_{g,chain}} = \frac{f_{bonded}}{T_{g,bonded}} + \frac{1 - f_{bonded}}{T_{g,neat}} \tag{2.8}$$

$$\frac{1}{T_{g,composite}} = \frac{w_{POSS}}{T_{g,POSS}} + \frac{1 - w_{POSS}}{T_{g,chain}} \tag{2.9}$$

The data from Kuo et al.[84] is fitted with a single fit parameter $T_{g,bonded}$. This is possible because the fraction of POSS bonding sites which are participating in hydrogen bonding was measured via FTIR. Start by supposing that the T_g of the composite is well described by a Fox equation representing the polymer chain and the POSS fillers. However, the effective T_g of the polymer chain is increased with increasing POSS loading, due to the attractive hydrogen bonds between polymer and POSS. Thus, we calculate the effective T_g of the polymer chain for a given POSS loading based on the measured T_g of a given composition and $T_{g,POSS}$. Equation 2.9 is rearranged to solve for $T_{g,chain}$.

$$T_{g,chain} = \frac{1 - w_{POSS}}{\frac{1}{T_{g,composite}} - \frac{w_{POSS}}{T_{g,POSS}}} \tag{2.10}$$

Equation 2.10 is then rearranged to be linear with f_{bonded}, which is calculated from stoichiometry analogously to the P(S-*r*-2VP) composite. Note that because p_{bond} was measured, a value of f_{bonded} can be calculated from geometry, unlike the OAPS/P(S-*r*-2VP) composite where p_{bond} is more difficult to measure experimentally.

$$\frac{1}{T_{\mathrm{g,neat}}} - \frac{1}{T_{\mathrm{g,chain}}} \cong f_{\mathrm{bonded}} \left(\frac{1}{T_{\mathrm{g,neat}}} - \frac{1}{T_{\mathrm{g,bonded}}} \right) \qquad 2.11$$

This linearized equation is plotted in Figure 22. The value of all parameters besides $T_{g,bonded}$ are known, thus the single fit parameter $T_{g,bonded}$ is found to be 978 K from a slope of 2.05×10^{-3} K^{-1} with $R^2 = 0.99$, with $T_{g,neat} = 52.5$ °C.

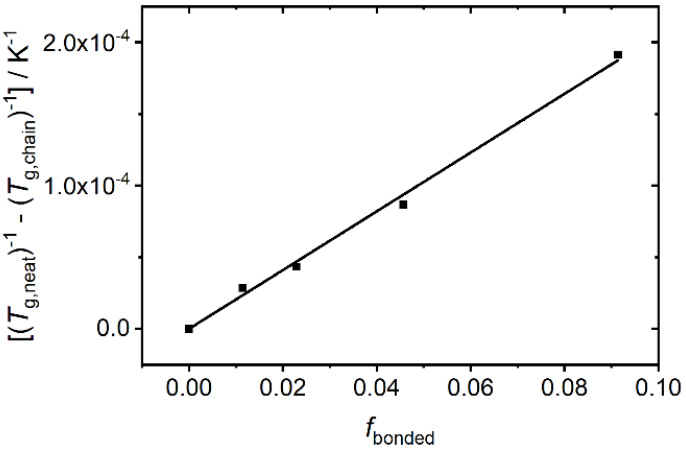

Figure 22. Graph of $T_{g,chain}$ vs w_{POSS} calculated from Equation 2.11 with $R^2 = 0.99$.

This analysis is applied to Kuo et al.'s T_g data measured by DSC,[84] which are clearly above the Fox equation prediction (dashed line in Figure 23b) due to the strong polymer-POSS interaction between hydroxyl groups on the polymer with the ester on the POSS via hydrogen bonds. In other words, the composite T_g is higher than what is predicted by simply treating octa(acetoxystyryl) POSS as a low T_g blend component. In Equation 2.5, f_{bonded} can now be calculated because $p_{bond} = 0.7$ is experimentally obtained, and $T_{g,POSS}$ = –15 °C and $T_{g,neat}$ = 50 °C are known. In Figure 23b, the solid line based on this analysis explains the data better than the conventional Fox Equation in the dashed line. We note that fitting the Kwei equation to the data yields a similarly good fit as demonstrated by the authors; however, this requires two fitting parameters whose physical significance is less immediately obvious.

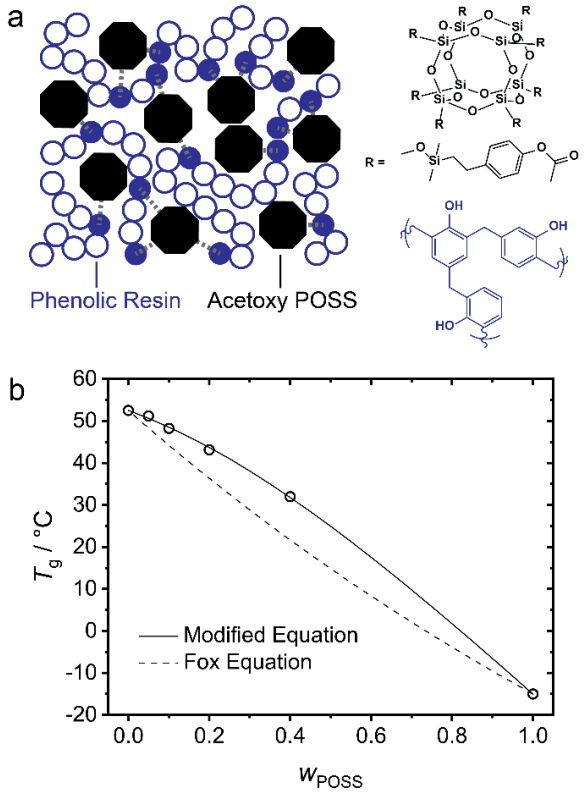

Figure 23. a) Schematic of acetoxy-POSS/Phenolic resin composite and chemical structures. b) T_g data collected by Kuo et al. for phenolic resins loaded with octa(acetoxystyryl) POSS at a variety of compositions.[84] The data set is well explained by our modified Fox equation, as well as the Kwei equation shown by Kuo et al.

The above assumption that treats polymer/POSS interactions as non-transient suggests an analogy to polymers synthesized with pendent POSS moieties (i.e., $p_{bond} = 1$), by only changing w_{bonded} to be identical to the weight fraction of monomers with pendent POSS groups incorporated into the polymer. Crucially, this analysis does not add the mass of POSS to the molar mass of the organic monomer, i.e., POSS is considered to be a hard material interface, rather than a chemical moiety. Equation 2.12 is derived by analogy to Equation 2.6 where f_{bonded} is the mole fraction of monomers with POSS pendants.

$$\frac{1}{T_{g,composite}} \cong \frac{f_{bonded}}{T_{g,bonded}} + \frac{1 - f_{bonded}}{T_{g,neat}} \qquad 2.12$$

This equation successfully explains T_g changes in data collected in poly(4-methyl styrene) (P4MS) copolymerized with styrenic pendent POSS monomers by Haddad and Lichtenhan measured as the softening temperature in a melt press (Figure 24).[38]

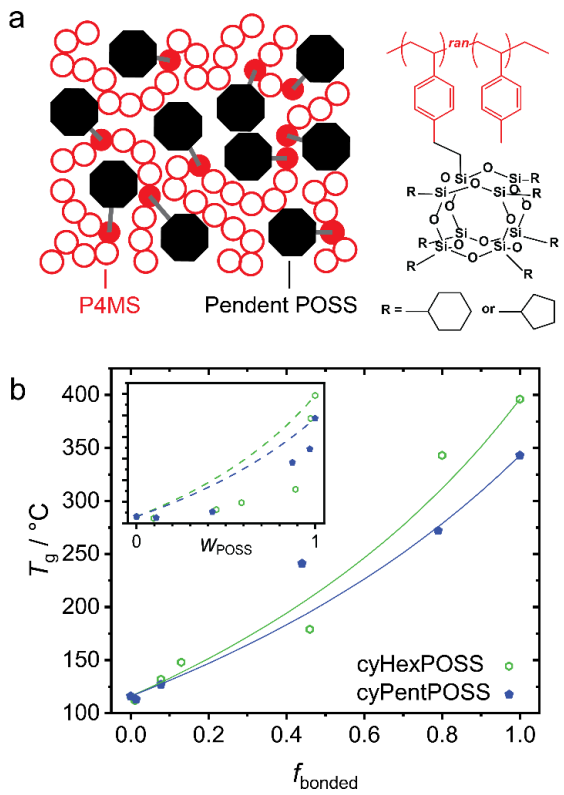

Figure 24**.** a) Schematic of pendent POSS composite and chemical structures of the poly(4-methyl styrene) (P4MS) pendent POSS copolymer. b) T_g data collected by Haddad and Lichtenhan for P4MS pendent POSS composites,[38] plotted versus mole fraction of bonded monomers f_{bonded}, or weight fraction of POSS w_{POSS} (inset). Solid lines are Fox equation predictions according to our model, and dashed lines in inset are the conventional approach.

A good agreement with the model prediction from Equation 2.12 is seen continuing all the way to $f_{bonded} = 1$ at which point every monomer has a pendent POSS (Figure 24b). Note that this analysis introduces no fitting parameters because all quantities in Equation 2.12 are easily obtained. In contrast, there is a substantial deviation from the prediction when plotted against w_{POSS} (i.e., the traditional Fox equation approach) (Figure 24b inset).

Essentially, the weight fraction of POSS in the system is less significant than the fraction of bonded monomer in the system when it comes to predicting T_g.

2.6 - Changes in Glass Transition Temperature with Polyhedral Silsesquioxane Loading and Composition in P2VP/NH_2-OPS

The previous results suggest that changing the functionality of the POSS filler will have a similar effect on T_g. Simulation and experiment were performed to study the effect of POSS surface chemistry on the T_g of poly(2-vinylpyridine) (P2VP) composites by precisely tuning n_{amine}, the number of amines (hydrogen bond donors), present on the POSS, i.e., variably aminated octa(phenyl) silsesquioxane (NH_2-OPS) (Figure 25). Overall, our results suggest that the number of interactions is a robust framework for understanding the T_g of a polymer/POSS nanocomposite and highlight the importance of molecular-scale geometry and size effects.

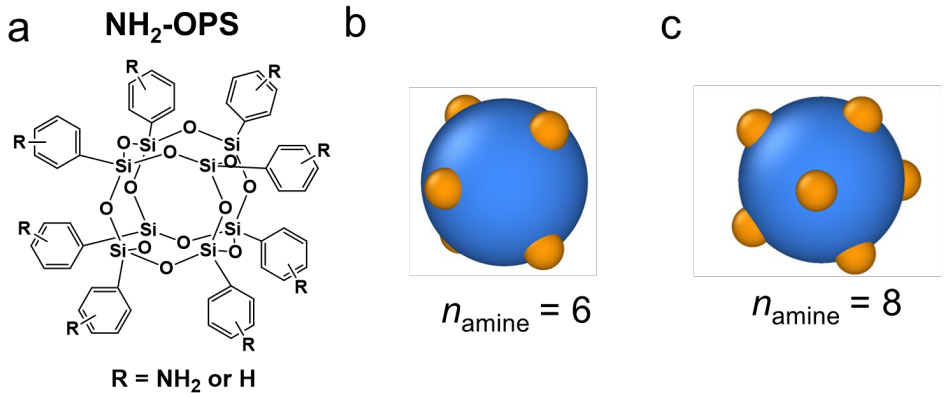

Figure 25. General chemical structure of NH_2-OPS and P2VP. (b) Illustration of coarse-grained POSS with 6 amine groups and (c) 8 amine groups, the blue sphere represents the POSS core and orange sites represent amine groups.

2.6.a – Changes in Glass Transition Temperature

The T_g of P2VP/NH_2-OPS nanocomposites were studied experimentally as a function of n_{amine} and ϕ_{POSS}, measured via DSC. As expected, T_g increased monotonically with NH_2-OPS loading (ϕ_{POSS}) as shown in Figure 26b, and does not saturate at high loadings, suggesting that the polymer is essentially "all-interfacial" without a distinct interfacial layer surrounding the nanoparticle.[92] Results are consistent with the hypothesis that the T_g increases with increasing number of interactions, i.e. increasing n_{amine} and increasing ϕ_{POSS} (Figure 26).

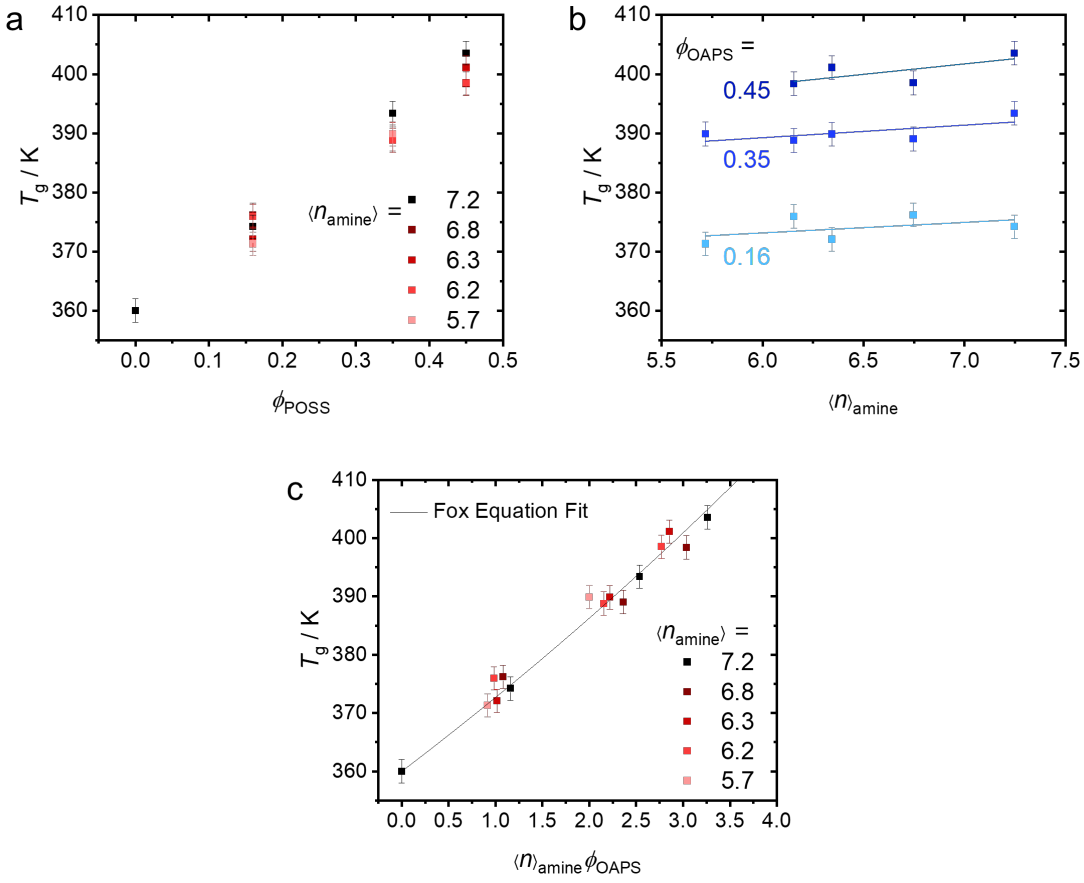

Figure 26. Plots of T_g versus composition in P2VP NH_2-OPS composites from DSC, with error bars corresponding to experimental uncertainty. a) Data is plotted against ϕ_{POSS}. b) Data replotted to show trend of T_g with $\langle n_{amine} \rangle$, with linear fits for each value. c) Data plotted against product of ϕ_{POSS} and $\langle n_{amine} \rangle$.

2.6.b – Coarse Grained Simulations of P2VP/ NH_2-OPS T_g

Coarse grained molecular dynamics simulations were also performed as detailed in collaborative work with Qian and coworkers.[70] In line with experimental results, an increasing number of interacting sites between polymer and POSS increases the T_g of the composite (Figure 27).

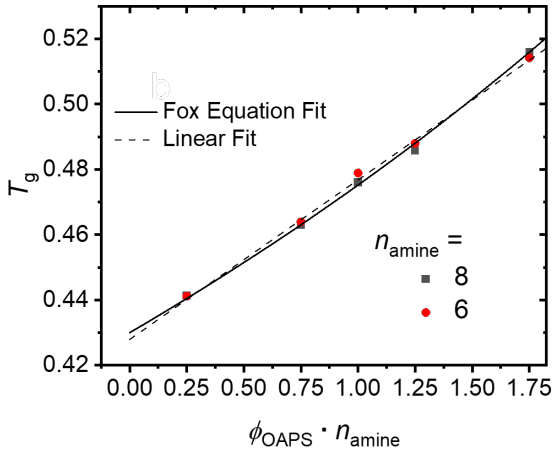

Figure 27. Glass transition temperature (in reduced units) for coarse-grained simulations of NH_2-OPS with either 6 or 8 amines. The trend matches the trend observed in experimental systems.

2.7 –Connection Between Nanofiller Aggregation and T_g Trends

The glass transition temperatures presented previously were all conducted on materials which displayed no signs of inhomogeneity or OAPS aggregation. Sample compositions which displayed evidence of OAPS aggregation tended to display plateaus in T_g with OAPS loading, with T_g no longer increasing despite the increasing weight fraction of filler. This is reasonable, given that the OAPS aggregates would have a much smaller effective surface area than would be the case if they were well-dispersed in the matrix, thus reducing the number of OAPS-polymer interactions (Figure 28).

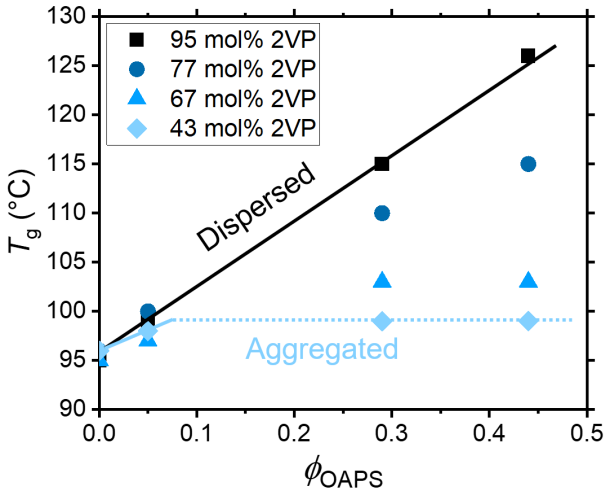

Figure 28. Sample data of glass transition temperatures of P(S-*r*-2VP)/POSS composites. For well-dispersed POSS, the trend is linear, whereas for samples displaying OAPS aggregation, the T_g increase plateaus at low loadings.

A similar trend has also been observed in a phenolic resin loaded with acrylic functionalized POSS, where there is a plateau in T_g at high POSS loadings which displayed evidence of aggregation in x-ray scattering measurements.[83] Given that materials with aggregated POSS clusters do not present particularly desirable properties, the connection between T_g, composition, and the presence of OAPS aggregates suggests the possibility of using T_g as a simple diagnostic method to screening for compositions which do not have well dispersed POSS, before carrying out other experiments such as X-ray scattering or mechanical testing.

2.8 – Attempts to Directly Quantify Number of Hydrogen Bonds in P2VP/OAPS

Directly quantifying the proportion of pyridine nitrogen atoms and OAPS amines which are participating in hydrogen bonds in equilibrium as a function of composition and temperature would be useful to further probe the effects of hydrogen bonds on T_g, and to understand the applicability of time-temperature superposition (TTS) to P2VP/OAPS nanocomposites. It is typically assumed that TTS holds in nanocomposite, however, this

assumption implicitly assumes that the nanocomposite structure is independent of temperature. If, for example, the number of hydrogen bonds present in the system dropped substantially at higher temperatures, this would have a confounding effect on the interpretation of the dynamics of the composite. Thus, various methods were attempted to determine the proportion of pyridines and amines that were participating in hydrogen bonds.

^{15}N-NMR was initially chosen as a method, because in principle, both the pyridine nitrogen and OAPS amine nitrogen will shift in the presence of hydrogen bonds; the pyridine N will be shifted upfield, while the amine will be shifted downfield. This was first attempted in solid-state ^{15}N-NMR at room temperature; however, no signal was detected, presumably due to the low abundance of ^{15}N isotopes in the material. Furthermore, the mixed tacticity of the pyridine repeat units of P2VP, and the mix of ortho-, meta-, and para-substituted amines on the phenyl rings of OAPS would be a reason that the signal would be weaker due to broadening. Signal-to-noise ratio in NMR increases with the square root of acquisition time, so there are diminishing returns to running these experiments for longer than the 16 hours trials ran here. The only other feasible way to increase the signal-to-noise ratio would be to increase the relative abundance of the ^{15}N isotope in the nanocomposite. To prepare a ^{15}N-enriched P2VP polymer, the best route would likely be to react acrylonitrile-^{15}N (available from Sigma Aldrich at time of writing) with acetylene to form 2-vinylpyridine-^{15}N in the presence of a cobalt catalyst.[93] Alternatively, OAPS could be synthesized with nitric-^{15}N acid, and the shift of the position of the nitrogen atom in the amine in the presence of hydrogen bond accepting P2VP could potentially be detected.

To test whether the study was sound in principle, a liquid-state ^{15}N NMR was conducted, using 2-vinyl pyridine (2VP) monomers as a small-molecule analogue of P2VP, as shown in Figure 29. This analogue was then scanned either neat or loaded with 20 wt% OAPS. The ^{15}N signal from 2VP was observed strongly above the baseline, but no amine signal of OAPS was observed. The presence of OAPS in solution shifts the pyridine peak upfield due to the formation of hydrogen bonds between the ^{15}N nucleus and the amine hydrogen of OAPS.

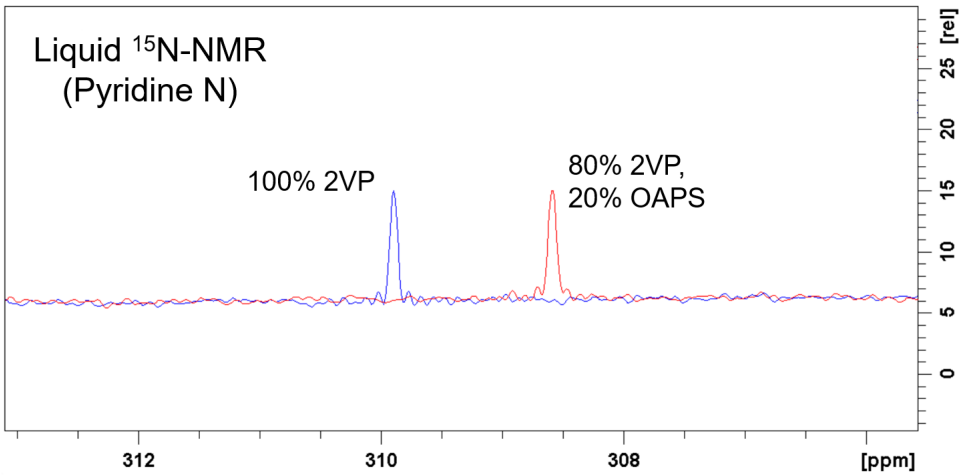

Figure 29. Liquid-state ^{15}N-NMR of 2VP neat (blue) or loaded with 20 wt% OAPS (red). Peak is shifted upfield by presence of hydrogen bond donors.

Fourier-Transform Infrared Spectroscopy (FTIR) was also performed on these OAPS/P2VP nanocomposites. Peak deconvolution was performed on the region 4000-3000 cm^{-1} to determine the N-H stretching peaks associated with OAPS amines as a function of temperature. It was hypothesized that this could reveal the proportion of hydrogen-bonded amines on OAPS, as has been performed in polyurethanes (secondary amines)[94,95] and other POSS nanocomposites (hydroxy groups).[84] The N-H stretching peaks can be cleanly deconvoluted, and the signal displays some temperature dependence, however, assigning these peaks to bonded versus unbonded amine N-H stretches is not

straightforward (Figure 30). Because the POSS contains a secondary amine, the interactions between the two protons introduce more peaks. Furthermore, FTIR is not a quantitative technique, the integrated value under the peaks is not necessarily precisely proportional to the actual relative abundance of the molecular species they represent.

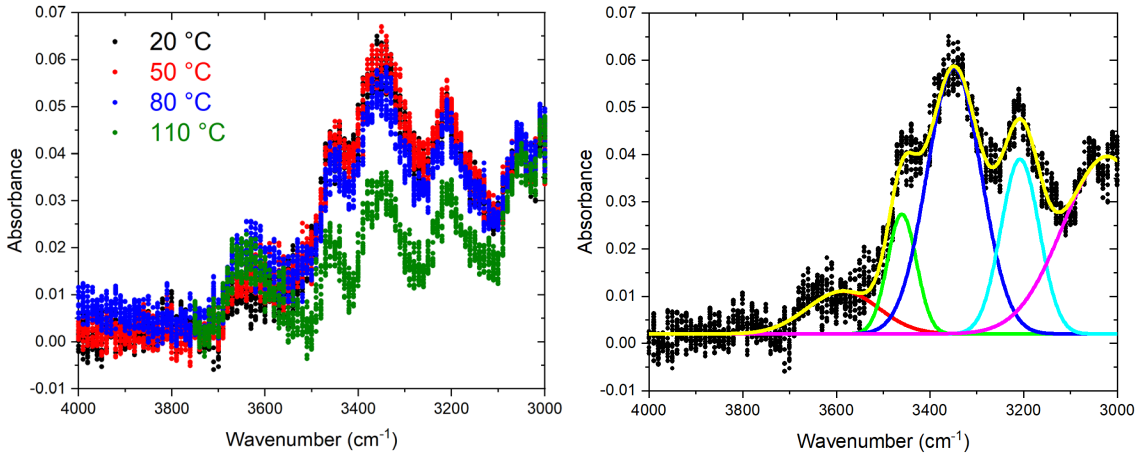

Figure 30. Heated FTIR scans of an P2VP/OAPS nanocomposite with 30 wt% OAPS loading, and peak deconvolution via Gaussian fit.

2.8.a – All-Atom Molecular Dynamics Simulations

Due to the complexity of directly determining the proportion of hydrogen-bonded components in the real system, all-atom molecular dynamics simulations were conducted through a collboration with Qian and coworkers. The all-atom molecular simulation is designed to give insight into the behavior of the composites[71] by analyzing the number of H-bonds per POSS molecule ($N_{\text{H-bond}}$) as a function of n_{amine} and temperature in a P2VP matrix (Figure 31a). $N_{\text{H-bond}}$ decreases substantially with temperature, decreasing by almost a factor of two in the temperature range studied (400 K to 530 K) for both values of n_{amine}. Also, in line with assumptions used to construct the Fox equation fitting in Figure 26c, the probability of hydrogen bond formation increases with the number of interaction sites in the nanocompsite (i.e. $N_{\text{H-bond}}$ increases with n_{amine}).

However, the increase in $N_{\text{H-bond}}$ is less than proportional to the increase in n_{amine} (Figure 31b). When the number of amines on each POSS is lower, each individual amine has a higher probability of participating in a hydrogen bond, likely due to the chain frustration associated with bonding to neighboring amines. The non-linearity between n_{amine} and $N_{\text{H-bond}}$ shows that our assumption of uniform spatial distribution of monomers and POSS was not entirely accurate when the number of amines on NH_2-POSS changes.

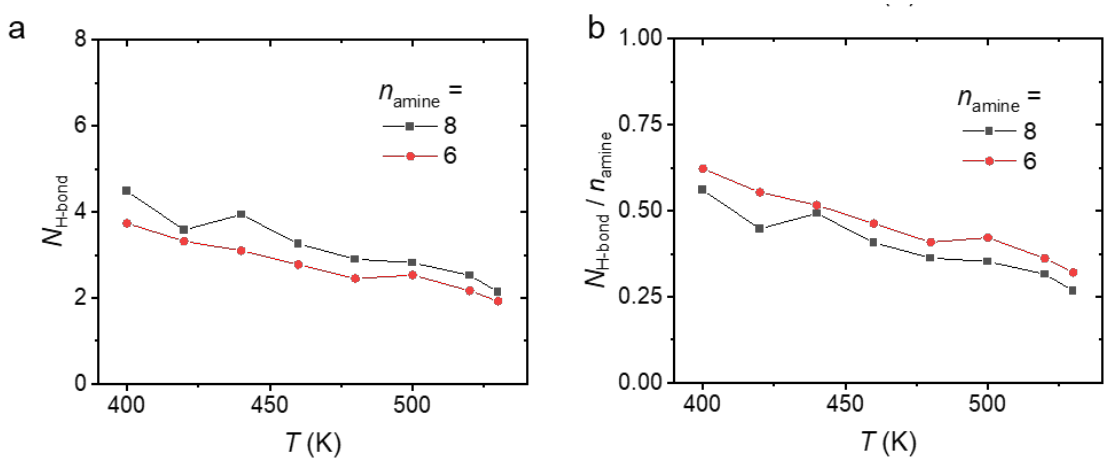

Figure 31. (a) Number of hydrogen bonds as a function of temperature and n_{amine} revealed by all-atom molecular dynamics simulations. There is a strong temperature dependence. (b) fewer amines lead to fewer hydrogen bonds, but this decrease is less than linearly proportional to n_{amine} indicating that the number of interactions between polymer and filler is more complex than would be assumed with a random mixing argument.

In other words, f_{bonded} has a more complex composition dependence than previously assumed. This effect is not observed in the coarse grained model, because the direction-specific nature of hydrogen bonding is not considered in the coarse grained model.[96] As a whole, these results show that approximating f_{bonded} to be proportional to the number of polymer-POSS interactions is generally sufficient to match experimental observations, however, this assumption slightly overestimates the number of hydrogen bonding sites observed in simulations due to the greater configurational freedom present in nanocomposites with fewer interaction sites.

2.9 – Conclusion

Invoking a framework that accounts for the number of interacting pairs in a polymer/POSS composite can give a straightforward picture of the composition dependence of T_g in a range of model systems. This analysis also holds when the filler functionality is systematically varied. Ideally, the fraction of monomers and/or nanofiller functional groups which are participating in hydrogen bonds with different components of the system would be experimentally verified, however, all-atom molecular dynamics simulations were able to capture the temperature and stoichiometric dependence of hydrogen bonding in the model P2VP/NH_2-OPS nanocomposite. Moving forward, further control experiments to determine hydrogen bonding fractions in model polymer/POSS nanocomposites could elucidate a precise picture of the temperature and composition dependence of hydrogen bonding. This insight will prove powerful for understanding, for example, the applicability of time-temperature superposition (TTS) in the rheological analysis of polymer nanocomposites, potentially in conjunction with advanced mechanical spectroscopy with an extended range of accessible oscillatory frequencies.[97–99]

CHAPTER 3

3 – DYNAMICAL CHARACTERIZATION OF POLYMER/POSS COMPOSITES VIA RHEOLOGY

3.1 – Introduction

As discussed in Chapter 1, the rheological response of polymer/POSS composites is largely dependent on whether the POSS and polymer have strong favorable interactions such as hydrogen bonds, or whether they have a weaker interaction. In the case where the interactions are weak, the apparent molar mass between entanglements as measured by the plateau modulus tends to decrease, in addition to an increase in the terminal flow frequency. This can be reasonably justified by an increase in polymer mobility and free volume near the POSS surface. However, in the case of strongly interacting polymer/POSS composites such as P2VP/OAPS, the behavior is quite different. The apparent width of the entanglement plateau decreases, with, if anything, an increase in the plateau modulus, and a relatively unchanged terminal flow frequency. With both phenomena for weakly and strongly interacting composites having an apparent connection to the response of entanglements to a mechanical stress, it is critical to identify the distinguishing features between the two classes of materials.

We hypothesize that these anomalous rheological properties at high OAPS loadings are governed by the emergence of a polymer relaxation which occurs on timescales which vary with ϕ_{OAPS}, independent of the presence of entanglements. The rheological response

of a model P2VP/OAPS composite system is presented and rationalized based on the principles of gelation at high OAPS loadings and the emergence of a relaxation process which dominates at timescales between the alpha process and disentanglement. Previous work[10] for entangled P2VP reported that the disentanglement/terminal flow time remains independent of OAPS loading until the system enters the gel regime in which the filler network dynamics dominate the polymer response, and breadth of the entanglement plateau decreased with increasing OAPS loadings. Based on this observation, four qualitative regimes of the rheological response are identified based on being either below or above entanglement molar mass (M_e) of P2VP and critical gelation concentration of OAPS (ϕ_{gel}) as shown in Table 2. Our systematic rheological study reveals that the timescale associated with either the onset of terminal flow (unentangled) or the onset of the entanglement plateau (entangled) exhibits the same loading dependence as the slower process.[100] These results support our hypothesis that the unconventional rheological response is due to the increasing timescale of a relaxation process occurring between the entanglement relaxation time and the α-relaxation time.

Table 2**.** The four regimes of the P2VP/OAPS rheological response, dictated by polymer entanglement and OAPS loading with regards to ϕ_{gel}.

Φ_{OAPS}	**Unentangled**		**Entangled**	
	Observation	***Explanation***	***Observation***	***Explanation***
$\phi < \phi_{gel}$	Zero-shear viscosity increases with $\sim\phi^n$	Viscosity increases due to extra process	Width of the entanglement plateau decreases. Zero-shear viscosity is unchanged	Extra process dominates reptation at intermediate frequencies normally dominated by reptation
$\phi > \phi_{gel}$	$tan\delta \rightarrow 1$ at low ω	Gelation	$tan\delta \rightarrow 1$ at low ω	Gelation

3.2 – Methods

NMR, FTIR, Nanocomposite sample preparation, X-ray scattering and DSC were performed as described in Chapter 2.

3.2.a – Rheometry

Rheometry measurements were conducted on a Malvern Kinexus PRO rheometer with Peltier Plate Cartridge heating stage under nitrogen atmosphere. 1.5 cm parallel plates were used for all measurements. Frequency was varied from 0.01 to 100 rad/s, with temperature up to 200 °C. The gap height was set to 1 mm. Data were analyzed and TTS master curves were constructed using the IRIS Rheo-hub software package.[101]

3.3 – Rheology of P2VP/POSS Composites with Variable Molar Mass

To systematically study the connection between the slower process of P2VP and the rheological response of the P2VP/OAPS nanocomposite, melt oscillatory shear rheometry was performed on P2VP/OAPS samples with different OAPS volume fractions (ϕ_{OAPS}) and different P2VP number average molar mass (M_n). The molar mass tested were M_n = 30 kDa, 58 kDa, and 850 kDa, while the M_e of P2VP is approximately 29 kDa.[102] P2VP and OAPS were co-casted from tetrahydrofuran and annealed at 180 °C at 10^{-5} mTorr for at least 5 days. To check the dispersion of OAPS in the P2VP matrix, small-angle X-ray scattering (SAXS) was performed on the samples, with representative examples shown in Figure 32. These results are in agreement with literature[5,10] and do not display low q features associated with large-scale phase separation due to nanoparticle aggregation.[70]

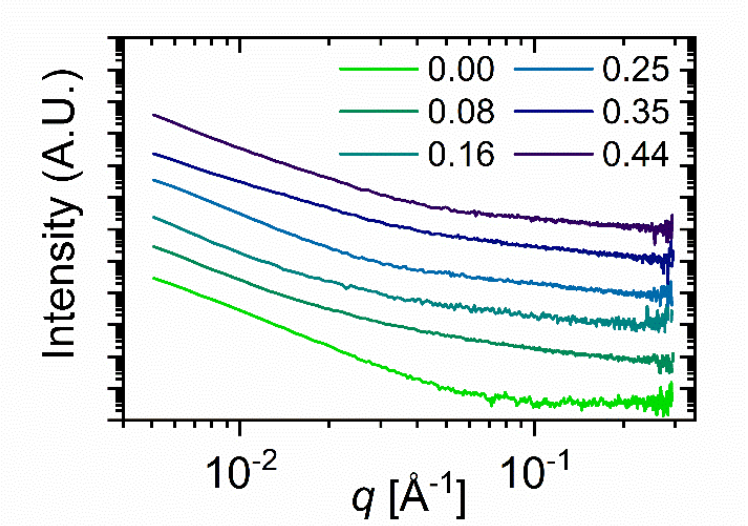

Figure 32. Scattering patterns of M_n = 58 kDa P2VP/OAPS composites loaded with different ϕ_{OAPS}. No evidence of OAPS aggregation is observed.

Rheometry experiments were performed on all samples with temperatures up to 200 °C under nitrogen atmosphere, and angular frequency (ω) varying from 0.01 to 100 rad/s. Results were shifted based on horizontal temperature shift factors a_T as shown in Table 3, Table 4, and Table 5. To reduce the number of fitting parameters, vertical shifting was not performed.

Table 3. Rheological shift factors for M_n = 30 kDa composites

M_n = 30 kDa							
ϕ_{OAPS} = 0		ϕ_{OAPS} = 0.08		ϕ_{OAPS} = 0.16		ϕ_{OAPS} = 0.25	
T [°C]	$\log_{10} a_T$	T [°C]	$\log_{10} a_T$	T [°C]	$\log_{10} a_T$	T [°C]	$\log_{10} a_T$
160	-1.31	170	-2.54	170	-2.54	160	-2.09
145	-0.38	140	0.00	140	0.00	140	0.00
140	0.00	125	0.76	125	0.76	130	0.37
130	0.80						
120	1.80						

Table 4. Rheological shift factors for M_n = 58 kDa composites

M_n = 58 kDa									
ϕ_{OAPS} = 0		ϕ_{OAPS} = 0.08		ϕ_{OAPS} = 0.16		ϕ_{OAPS} = 0.25		ϕ_{OAPS} = 0.35	
T [°C]	$\log_{10} a_T$	T [°C]	$\log_{10} a_T$	T [°C]	$\log_{10} a_T$	T [°C]	$\log_{10} a_T$	T [°C]	$\log_{10} a_T$
170	-1.85	170	-1.85	170	-2.05	185	-2.90	185	-3.33
150	-0.74	150	-0.92	150	-0.82	170	-2.14	170	-2.49
140	0.00	140	0.00	140	0.00	150	-0.74	150	-1.06
125	1.33	125	1.35	130	1.02	140	0.00	140	0.00
				125	1.63	135	0.63	135	0.62

Table 5. Rheological shift factors for M_n = 850 kDa composites

M_n = 850 kDa							
ϕ_{OAPS} = 0		ϕ_{OAPS} = 0.08		ϕ_{OAPS} = 0.16		ϕ_{OAPS} = 0.25	
T [°C]	$\log_{10} a_T$	T [°C]	$\log_{10} a_T$	T [°C]	$\log_{10} a_T$	T [°C]	$\log_{10} a_T$
200	-3.12	200	-3.35	200	-3.49	200	-3.42
180	-2.51	180	-2.64	180	-2.62	185	-2.81
160	-1.52	160	-1.53	160	-1.55	170	-2.17
140	0.00	140	0.00	140	0.00	150	-0.85
130	0.95	130	1.01	130	1.03	140	0.00
120	2.08	120	2.26	120	2.33	130	1.01
115	2.76					125	1.61

3.3.a – Small-Amplitude Oscilatory Shear Rheometry Results

The storage (G') and loss (G'') moduli as a function of frequency and temperature were measured for P2VP/OAPS nanocomposites with variable ϕ_{OAPS} and M_n. Representative G' and G'' data for M_n = 58 kDa (weakly entangled) and M_n = 850 kDa (highly entangled) are shown in Figure 33. For the composite with M_n = 58 kDa at the highest accessible loading (ϕ_{OAPS} = 0.44), the material displays a gelation response, presumably due to the formation of a percolated nanoparticle network in a similar manner to silica nanoparticles.[103,104] In the ungelled state, the response is shifted to lower frequencies as ϕ_{OAPS} increases.

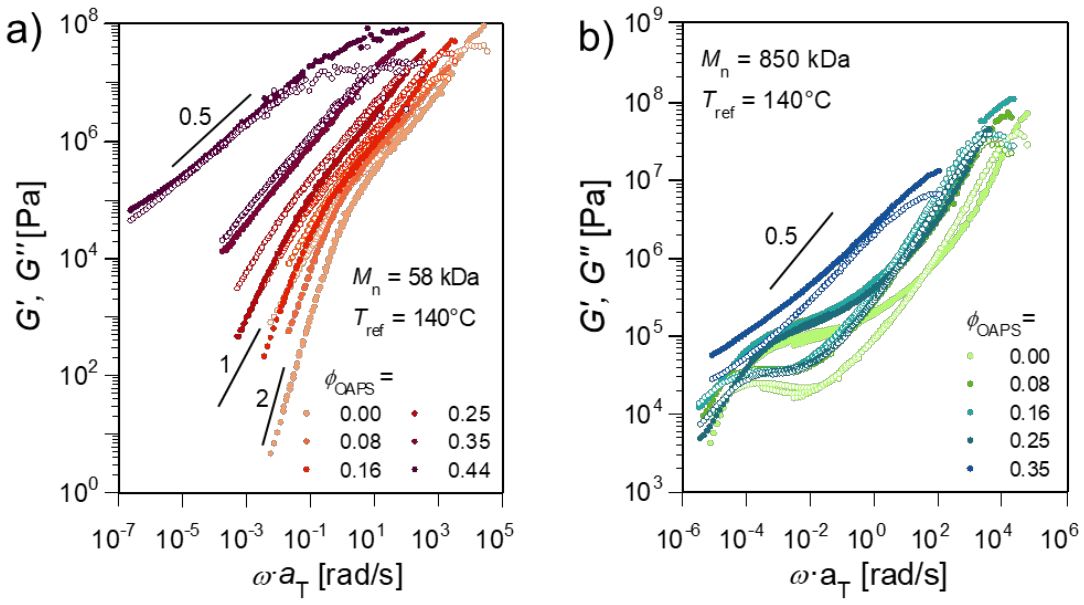

Figure 33. Storage (G', closed symbols) and loss (G'', open symbols) moduli measured by small amplitude oscillatory shear rheometry for P2VP/OAPS with (a) M_n = 58 kDa and (b) M_n = 850 kDa at different OAPS loadings. Master curves are created by shifting with shift factors in Table 4 and Table 5. Curves show mechanical reinforcement at moderate loadings ($\phi_{OAPS} \leq 0.25$) with gelation at high loadings ($\phi_{OAPS} \geq 0.35$).

The 850 kDa sample (Figure 33b) has an entanglement plateau and is qualitatively consistent with previous reports of entangled P2VP/OAPS nanocomposites.[10] At moderate loadings ($\phi_{OAPS} \leq 0.25$), the terminal flow time τ_t is relatively unchanged with OAPS loading, while the width of the entanglement plateau decreases as the entanglement onset time τ_e, approaches τ_t.

The construction of these figures relies on the assumption that time-temperature superposition (TTS) holds. Although the data at different temperatures collapsed nicely to a single master curve, the implicit assumption that the temperature dependence of all relaxation processes is identical is not strictly true for the loaded P2VP/OAPS composites due to the temperature dependence of hydrogen bonding. However, as noted in the all-atom molecular dynamics simulations presented in the previous Chapter, there are no sharp transitions in the fraction of hydrogen bonded monomers in this temperature regime. As

evidence that TTS is at least approximately correct, the τ_t remains largely unchanged in the M_n = 850 kDa nanocomposites, regardless of reference temperatures in the range 140°C ≤ T_{ref} ≤ 200°C (Figure 34). This indicates that TTS is a reasonable approximation in the P2VP/OAPS system, and that the number of entanglements in the polymer is roughly constant with OAPS loading.

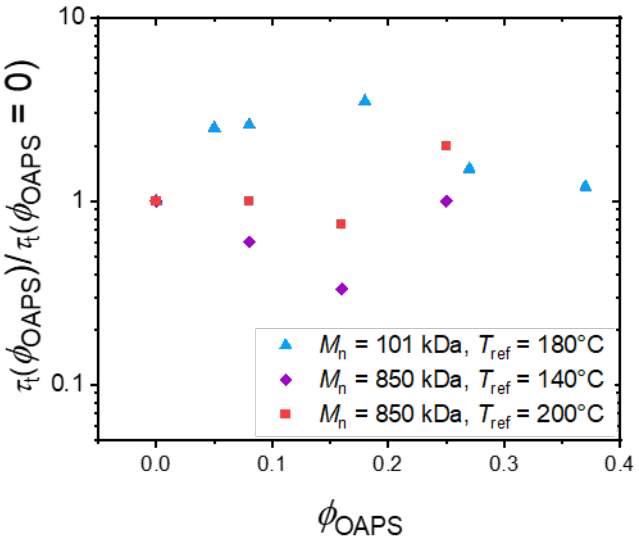

Figure 34**.** Plot of the rheological terminal flow times τ_t for the entangled composites at different reference temperatures against ϕ_{OAPS}.

To illustrate the different regimes of gelled versus ungelled nanocomposite rheology, the data obtained in Figure 33 are replotted as complex viscosity (η^*) in Figure 35. For the 58 kDa samples, the viscosity becomes saturated at low frequencies (i.e., zero-shear viscosity) for $\phi_{OAPS} \leq 0.16$, and diverges for $\phi_{OAPS} \geq 0.25$, which is indicative of gelation. The zero-shear viscosity increases with increasing OAPS loading, which is a completely different behavior compared to entangled samples. Due to instrumental frequency and temperature limitations, the zero-shear viscosity could not be evaluated for the 850 kDa samples, but the terminal behavior of η^* showed small deviations despite a 12 K increase in T_g.

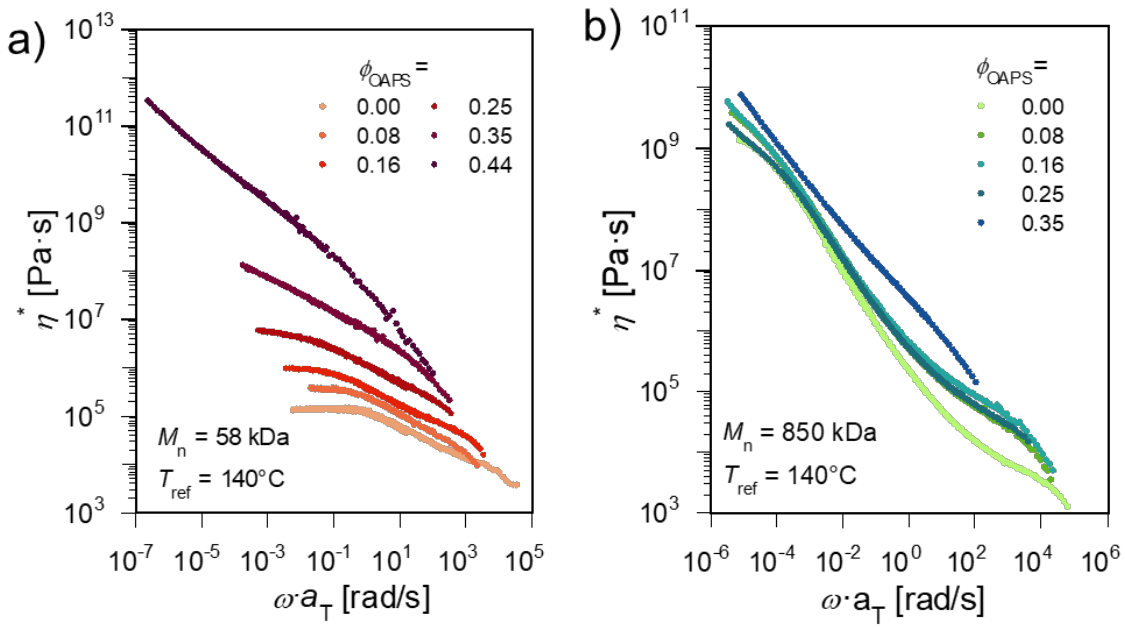

Figure 35. Frequency-dependent complex viscosity (η^*) of the P2VP/OAPS composites with (a) M_n = 58 kDa and (b) M_n = 850 kDa as a function of ϕ_{OAPS}.

3.3.b –Rheometry to Probe P2VP-OAPS and OAPS-OAPS Interactions

Two further experiments were performed to give insight into the role of OAPS-OAPS interactions and OAPS-P2VP interactions on the rheology of the nanocomposite. It was hypothesized that the nonlinear rheological response of the composite would have a strong dependence on OAPS loading if OAPS-OAPS interactions dominated the rheology, which would be observed in experiment as a substantial change in the onset of shear thinning and the shear thinning exponent of the nanocomposites depending on OAPS loading. Strain amplitude sweeps for the M_n = 850 kDa sample were performed at 180°C and 200°C at 0.01 Hz (Figure 36). The frequency is chosen to target the middle of the entanglement plateau in the neat polymer. Note that the high ϕ_{OAPS} sample (ϕ_{OAPS} = 0.35) could not be measured at high strains due to poor adhesion between the top rheometer plate and the sample. Across all samples, there was no appearance of a secondary plateau at high strain rates, and shear thinning exponents and onset strains are similar (Table 6). Therefore,

the effects of OAPS-OAPS and OAPS-P2VP interactions are either unaffected by strain or decrease in significance relative to the polymer chain relaxation. More studies in the nonlinear regime are needed to draw a firm conclusion in this regard.

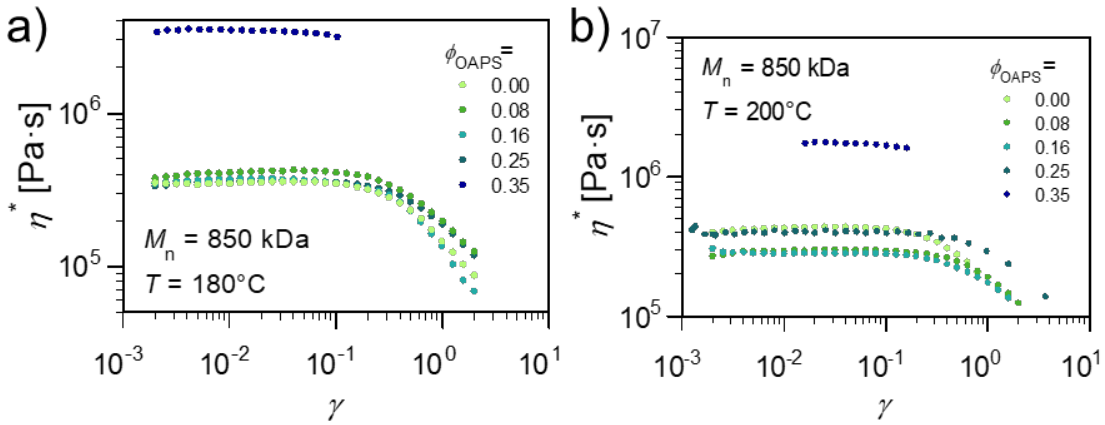

Figure 36. Strain amplitude sweeps at f = 0.01 Hz for the 850 kDa samples at a) 180 °C and b) 200°C.

Table 6. Shear thinning exponents measured from Figure 36

ϕ_{OAPS}	Shear Thinning Exponent	
	T = 180 °C	T = 200 °C
0	0.26	0.41
0.08	0.37	0.42
0.16	0.50	0.54
0.25	0.26	0.33

To test the effects of P2VP-OAPS interactions on the rheology of the nanocomposites, OAPS was loaded into random copolymers of styrene and 2VP, described in Chapter 2.[70] These polymers are unentangled with M_w of approximately 15 kDa. The zero-shear viscosity of the nanocomposites was measured at a reference temperature of 160°C and normalized by molecular weight in accordance with Rouse dynamics (Figure 37). If the OAPS-P2VP interactions played a large role in the rheology, it would be expected that the copolymer with the lowest f_{2VP} would have a weaker viscosity increase with polymer loading. However, the opposite appears to be true, with the lowest f_{2VP} nanocomposite displaying the strongest increase in viscosity with OAPS loading, however,

the results are not particularly differentiated between different f_{2VP} (Table 7). This indicates that the OAPS-P2VP interaction is not strongly influential on the rheology of the composite, at least at the experimentally achievable range of f_{2VP}.

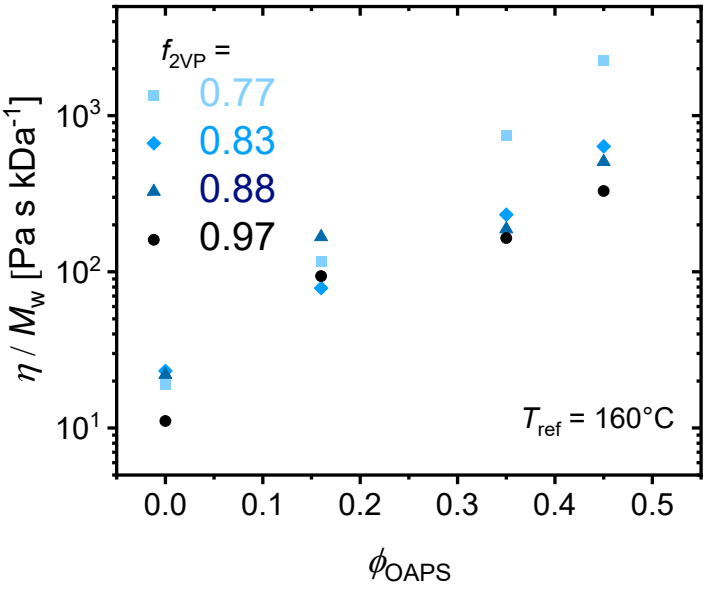

Figure 37**.** Terminal viscosity of poly(styrene-*r*-2VP) copolymers loaded with varying levels of OAPS.

Table 7. Exponential Slopes in f_{2VP} Copolymers at T_{ref} = 160°C

f_{2VP}	M_w (kDa)	Đ	Exponential Slope (n)
0.77	18	1.13	4.6 ± 0.1
0.83	14	1.10	3.1 ± 0.2
0.88	15	1.11	2.6 ± 0.8
0.97	13	1.15	3.0 ± 0.7

3.4 – Quantitative Analysis of Rheological Timescales

To analyze the relationships of the critical timescales, the loss tangents (tan δ) of the P2VP/OAPS are shown in Figure 38 with arrows corresponding to critical rheological time scales. For low M_n polymers with fewer entanglements, the critical time is given as

the unentangled terminal flow time τ_t, corresponding to when tan δ approaches a constant value independent of angular frequency (Figure 38a). In the 850 kDa sample (Figure 38b), the critical timescale is the entanglement onset time τ_e, corresponding to ~10^1 rad/s where tan δ is unity. This is chosen as a convenient metric used previously in the literature,[10] and note that this can physically be thought of as the time at which the stress supported by entanglements begins to dominate the mechanical response rather than the extra relaxation process. These features can also be seen in Figure 33b as the crossover point of G' and G'' on approaching the entanglement plateau from low to high frequency. In contrast to τ_e, the terminal flow time for high M_n polymers (τ_t) shows weaker composition dependence.

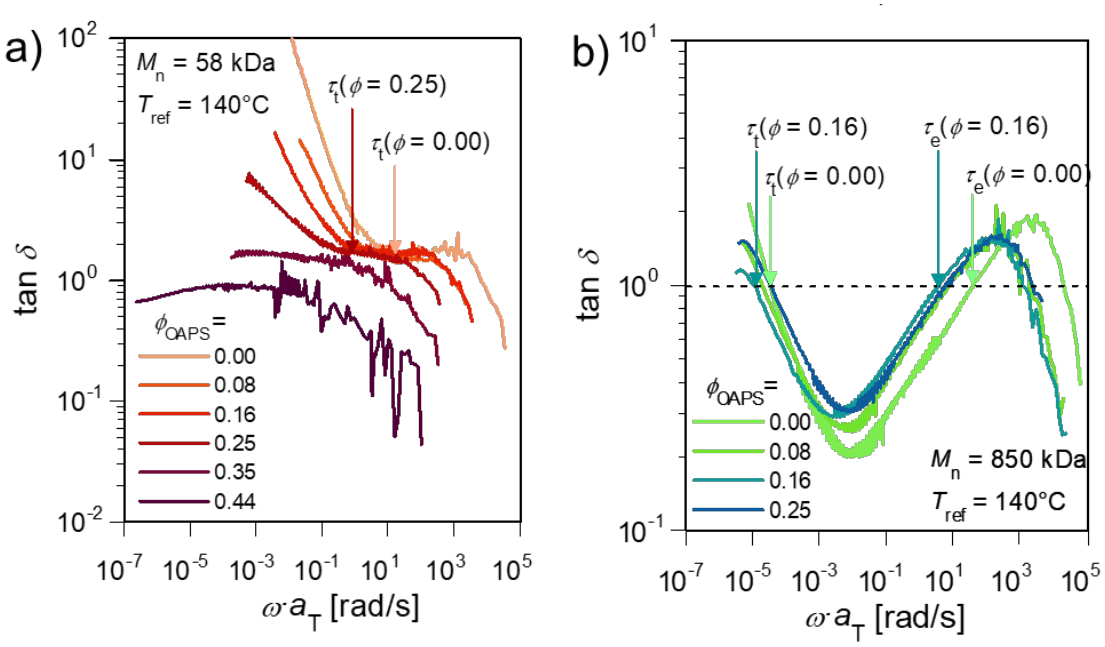

Figure 38. Loss tangent of the (a) M_n = 58 kDa and (b) M_n = 850 kDa P2VP/OAPS composites for various ϕ_{OAPS}. Arrows mark the critical timescales of terminal flow time τ_t (58 kDa and 850 kDa), and entanglement onset time τ_e (850 kDa) for the compositions that do not display rheological gelation.

The timescales of terminal flow τ_t for the low M_n nanocomposites are shown in Figure 39a, and the timescale of entanglement onset τ_e is shown in Figure 39b for the high M_n samples. Both are plotted against the α-relaxation time of P2VP/OAPS with M_n = 15

kDa adapted from dielectric spectroscopy.[105] Data for the 101 kDa nanocomposites is adapted from Cheng et al.[10] These critical timescales (τ_t and τ_e) are also plotted in Figure 38b, normalized to those of the neat polymer. The terminal flow time, entanglement onset time, slower process time, and α-relaxation time are fitted to $\log_{10}\tau \propto n \cdot \phi_{OAPS}$, where n is a temperature-dependent exponent and indicates how sensitive τ is to ϕ_{OAPS}.

The ϕ_{OAPS} dependence of critical rheological timescales (τ_e and τ_t for low M_n samples) characterized by the exponent $n = 3.5 \pm 1.8 \sim 6.5 \pm 1.4$ is much stronger than that of the α-process time ($n = 0.9 \pm 0.1$) as shown in Table 8. In other words, the change in T_g with increasing ϕ_{OAPS} can only be responsible for 1/5 of the change in timescale observed in the rheological measurements. The terminal flow time τ_t of the entangled polymers is essentially independent of ϕ_{OAPS} ($n = 0.2 \pm 1.5 \sim 0.6 \pm 0.5$, data shown in Figure 34). This illustrates that sticky Rouse and sticky reptation models[72–75,106] cannot capture the rheological complexity of these materials if the OAPS loading is used as a proxy for sticker count; the terminal flow time has a strong dependence on sticker count in these models, yet no strong ϕ_{OAPS} dependence of τ_t is observed.

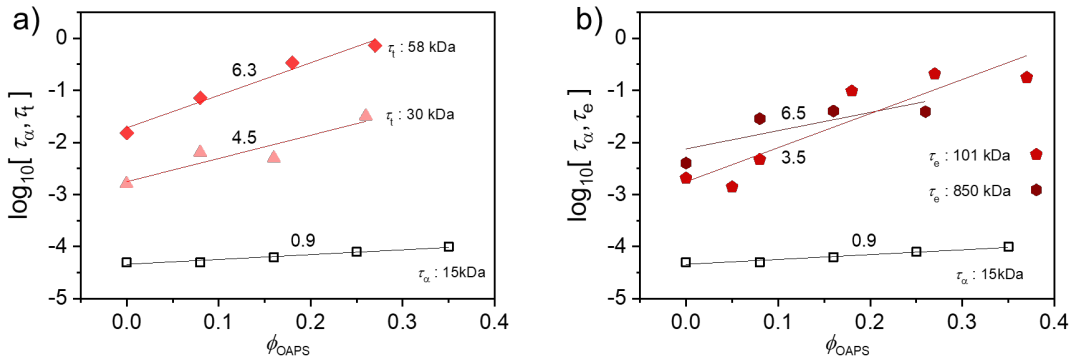

Figure 39. (a) Plot of the terminal flow times τ_t of the lower M_n samples, alongside the α-process time and their lines of best fit. (b) Plot of the entanglement onset times τ_e of the higher M_n samples. Note that across all analyses, nanocomposite compositions that display rheological gelation are excluded.

Table 8. Scaling exponent n of relaxation timescales with ϕ_{OAPS} ($\log_{10}\tau \propto \phi_{\mathrm{OAPS}} \cdot n$)

Relaxation Process	Approximate Timescale at 140°C [s]	M_n [kDa]	n
α-relaxation (τ_α)	10^{-4}	5	0.9 ± 0.1
Entanglement onset (τ_e)	10^{-3}-10^{0}	101	6.5 ± 1.4
		850	3.5 ± 1.8
Terminal flow for low M_n (τ_t)	10^{-3}-10^{-1}	32	4.5 ± 1.3
		58	6.3 ± 0.7
Terminal flow for high M_n (τ_t)	10^{0}	101	0.6 ± 0.5
	10^{5}	850	0.2 ± 1.5

3.5 – Conclusions

The linear-rheological response of P2VP/OAPS not only displays features that are common to other nanocomposites, such as gelation at high loadings, but also reveals unique dynamical behavior, particularly a marked increase in T_g and short relaxation times with little effect on entanglement relaxation time. Between the glassy frequencies and the entanglement frequencies, the modulus of P2VP/OAPS is enhanced relative to the neat polymer due to polymer/nanoparticle interactions which are present in unentangled or weakly entangled polymers, indicating that this response is not tied to entanglement. Thus, the apparent disentanglement observed in these strongly attractive composites does not correspond to the physically distinct, modest disentanglement effects discussed in Chapter 1 for weakly interacting POSS nanocomposites.

Additionally, experiments did not reveal a strong effect of 2VP content on the rheological response of the composite. This is contrary to the strong dependence of T_g on polymer and nanofiller composition revealed in the previous chapter, further indicating a decoupling of segmental and terminal flow behavior in these composites. Strain-sweep

rheometry was unable to establish the emergence of an OAPS jamming response at high strains, and linear rheometry of composites with varying f_{2VP} did not show a strong dependence on polymer composition. It is thus unclear whether the reinforcement is caused by an OAPS-OAPS interaction, or a polymer-OAPS interaction. Further work on tailoring the interactions in similar materials to target mechanical reinforcement on a specific timescale offers an intriguing way to create materials with enhanced T_g without substantially affecting processability on longer timescales.

CHAPTER 4

4 – DIELECTRIC RELAXATION SPECTROSCOPY OF POLY(2-VINYL PYRIDINE) HOMOPOLYMERS, COPOLYMERS, AND NANOCOMPOSITES

4.1 – Introduction

As discussed in Chapter 3, the rheological behavior of the P2VP/OAPS composite displays evidence of a secondary relaxation process manifesting on intermediate timescales between α-relaxation and the entire chain motion, which decreases the apparent width of the entanglement plateau but does not have a strong effect on entanglements itself. For this reason, we employed dielectric relaxation spectroscopy (DRS) for studying this relaxation, and potentially bringing clarity to the physical mechanism of the process.

DRS measurements were undertaken by collaborators, as described in our published work.[105] The α-process of the P2VP/OAPS composite was identified across a range of OAPS loadings, with associated timescales shown in the analysis of Chapter 3. In addition to the α-process, a slower relaxation process was observed, with a timescale that appears to match the timescale of the hypothesized extra relaxation process revealed by rheometry in Chapter 3, also increasing exponentially with OAPS loading (Figure 40). This process appeared in the derivative of the real part of the complex permittivity,[107] but became more pronounced when an insulating air layer was introduced between the upper electrode and the sample, with the intention of reducing DC conductivity, which occurs due to charge carrier motion between electrodes at low frequencies (Figure 41).

Additionally, the timescale of the associated relaxation appears to agree with the timescale of the slower Arrhenius processes (SAP) recently identified by Song et al. in polymer thin films via dielectric spectroscopy.[63] For clarity, the hypothesized rheological process will be denoted as "process-R", the process observed via DRS as "process-D", and the slower Arrhenius process as SAP.

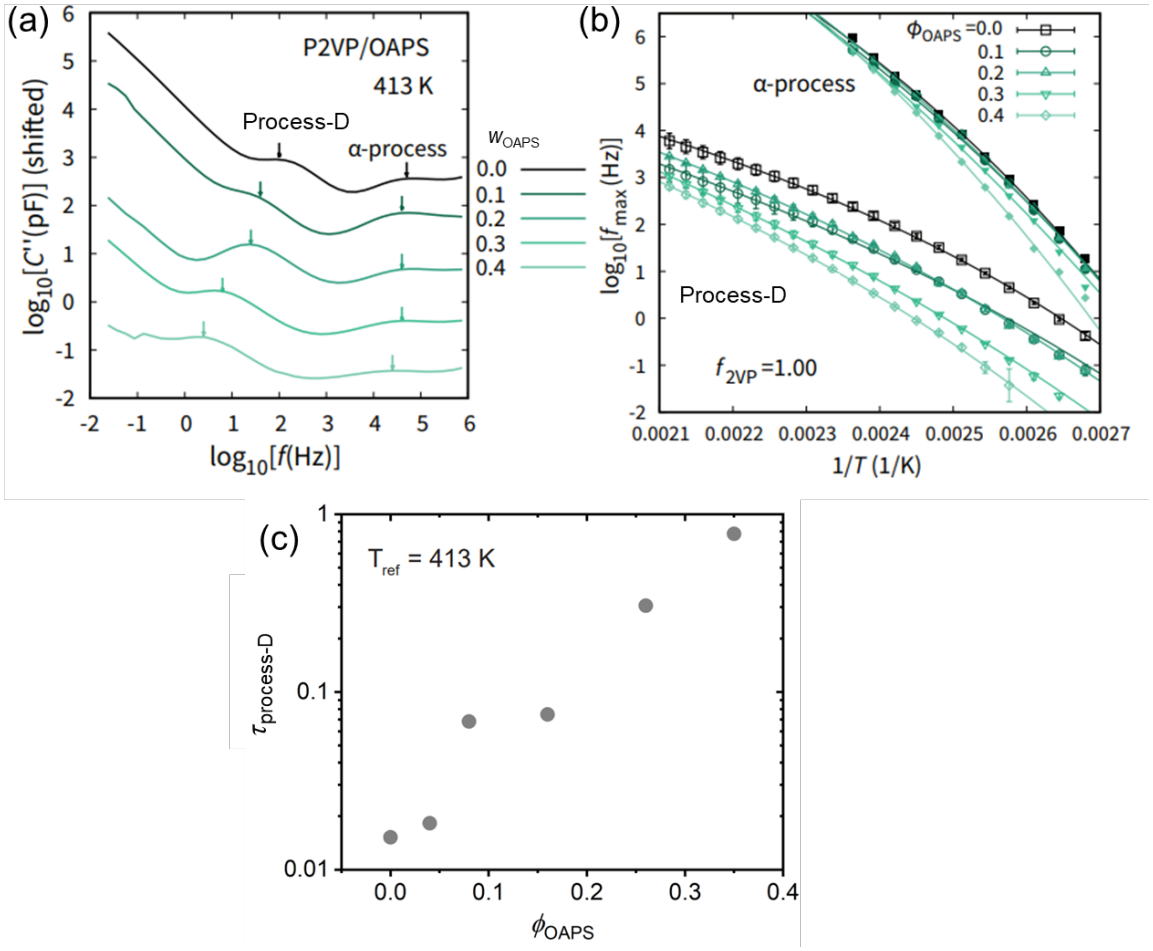

Figure 40. (a) Imaginary part of the complex capacitance of the dielectric response of P2VP/OAPS. Peaks correspond to dielectrically active processes in the material. (b) Temperature dependence of the α-process and process-D. (c) Process-D time versus OAPS loading, displaying an exponential increase with linearized slope of 4.9 ± 0.1.

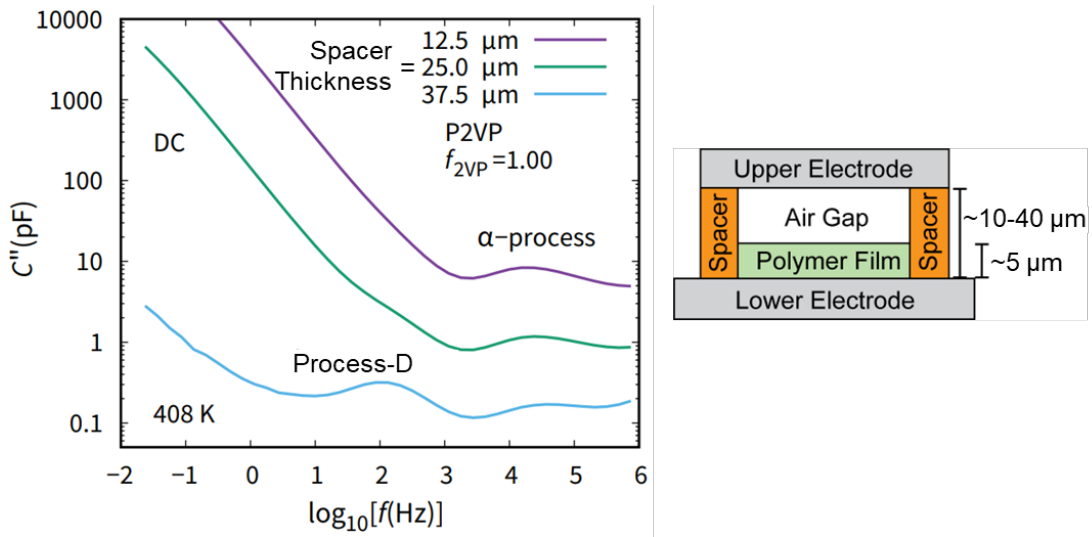

Figure 41. Dependence of dielectric response on spacer thickness.

A key factor for determining the mechanism of this relaxation would be the impact of polymer molar mass on the timescale of the process. This relaxation could then potentially be related to a physical picture, such as the vehicle mechanism mentioned in Chapter 1, depending on the molar mass dependence. The vehicle mechanism suggests a weak to non-existent relationship between the short-time motions of OAPS and polymer molar mass.[49] Measurements across a range of molar masses from 2 kDa to 850 kDa were taken for both neat polymer, and for nanocomposites with 20 wt% OAPS loading. As shown in Figure 42, the α-process matches the expected trend for polymers of increasing molar mass described empirically by the Flory-Fox equation; at very low molar mass, the frequency of the segmental relaxation degreases (i.e., T_g increases) until saturating at higher molar masses. However, the timescale of process-D is extremely scattered over 2 orders of magnitude, with no discernable trend with molar mass. This suggests an experimental artifact may strongly affect process-D but not the α-process.

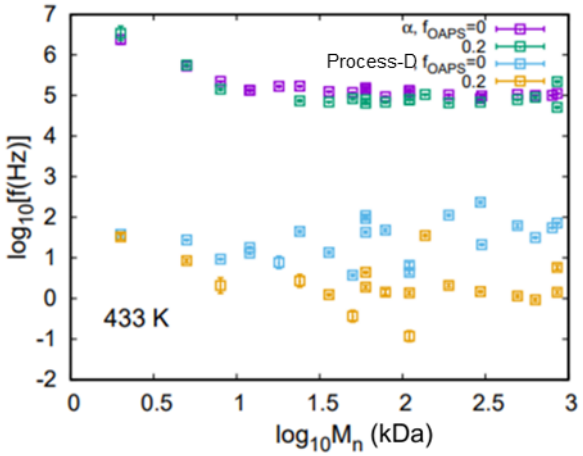

Figure 42. Molar mass dependence of the frequency of process-D and the α-process in DRS experiments.

4.2 – Methods

NMR, GPC, nanocomposite sample preparation, and DSC were performed as described in Chapter 2.

4.2.a – P2VP Synthesis

Procedure to synthesize P2VP was identical to that described in Chapter 2. If applicable, RAFT end-groups were then cleaved by stirring the polymer in a 0.5 M ethylamine solution in THF at room temperature for 30 minutes before precipitating two extra times in methanol.

4.2.b – Dielectric Relaxation Spectroscopy (DRS)

DRS measurements were performed by Dr. Koji Fukao and coworkers Hiromu Tabuchi, Ryo Iguchi, Hiroki Nobori, and Jun Yoshioka, as described in our published work.[105]

4.3 – Relation Between Slower Process and Other Phenomena

Because process-D occurred at temperatures and frequencies in which DC conductivity tended to dominate the impedance response of the material, an insulating air gap layer was introduced between the polymer surface and the upper electrode during testing. This experimental procedure has been employed previously, and has been shown in theory and practice to introduce a "conductivity peak" unrelated to a molecular relaxation in the material.[107–111] For clarity, this process will be named process-C, which can be thought of as a Maxwell–Wagner–Sillars (MWS) polarization of the insulator-sample interface, occurring approximately at the crossover frequency of the real and imaginary parts of the complex permittivity of the material. Air bubbles present in polymer samples can also introduce a similar artifact at similar frequencies revealed by the derivative method,[107] which could potentially correspond to the process-D, which was observed without an insulating air gap. As shown in previous Chapters, SAXS measurements of polymer nanocomposites routinely show $I \sim q^{-3}$ scaling, which is often attributed to the presence of crazes (i.e. voids) in the samples on the order of 10-100 nm in size,[89] which would thus cause MWS polarization to be observed.

4.3.a – MWS Peak from Air Gap

To evaluate the connection between process-D and process-C (a conductivity peak arising due to MWS polarization at the interface), a simple calculation was performed to check the expected position of a process-C peak based on the physical parameters of the experiment,

$$\tau_{\mathrm{MWS}} = \frac{\varepsilon_0(\varepsilon_1 d_2 + d_1)}{\sigma_1 d_2}, \tag{4.1}$$

$$\Delta C_{\mathrm{MWS}} = \frac{\varepsilon_0 S d_1}{d_2(\varepsilon_1 d_2 + d_1)}. \qquad 4.2$$

Polystyrene homopolymer (PS) at 200°C was evaluated from our experimental data with the conductivity $\sigma_1 = 4.0 \times 10^3$ pF/m·s, the thickness of PS layer $d_1 = 3.5$ μm, the thickness of air gap $d_2 = 34$ μm, dielectric permittivity $\varepsilon_1 = 2.8$, the area $S = 2.3 \times 10^{-4}$ m^2. Using these parameters, we obtain the peak frequency and relaxation strength of a possible MWS process:

$$f_{\mathrm{MWS}} = 5 \text{ Hz}, \qquad \Delta \mathrm{C}_{\mathrm{MWS}} = 2 \text{ pF} \qquad 4.3$$

The observed values of process-D evaluated at 200°C are:

$$f_{\mathrm{process-D}} = 27 \text{ Hz}, \qquad \Delta \mathrm{C}_{\mathrm{process-D}} = 6 \text{ pF} \qquad 4.4$$

There is a distinct difference between these values, however, it should be noted that the process-C peak is not always observed precisely at calculated frequencies.[107]

4.3.b – Comparison of Different Phenomena

The temperature dependence, timescale, and exponential dependence on OAPS loading are summarized in Table 9. In addition to the processes mentioned previously, conformational isotropization (CI) of the pendant polymer backbones are also included.[112] Based on the available data, process-D could reasonably be assigned to either process-R or process-C, however, it appears distinct from the SAP due to the differing temperature dependence.

Table 9. Parameters Describing Various Processes Which Could Occur in P2VP/OAPS

Process	Method	Materials	Temperature Dependence	Timescale at 140°C (s)	n – OAPS Loading Dependence
Process -D	DRS	P2VP, PS, and their copolymers	Super-Arrhenius	10^{-2} to 10^{0}	5.0 ± 0.1
Process -R	Rheology	P2VP/OAPS Nanocomposites	(a)	10^{-3} to 10^{0}	4.5 ± 1.5
Process -C	DRS	Various Polymers	Super-Arrhenius	10^{-3} to 10^{0} (b)	(b)
SAP	DRS	Various Polymers	Arrhenius	10^{-2} to 10^{0} (d)	–
CI	NMR	Poly(n-alkylmethacrylates)	Super-Arrhenius	10^{-2} to 10^{-5} (e)	–

a – The temperature dependence of process-R is unclear due to the necessity of TTS to access an appropriately broad frequency window
b – Calculated by assuming a MWS polarization of the polymer-air interface
c – This exponent can in principle be determined based on the DC conductivity measured in the DRS measurements
d – Data for polystyrene, not poly(2-vinylpyridine), which was not tested by Song et al.[63]
e – Time depends on length of alkyl chain

Further work would be needed to determine whether process-R may in fact be related to the SAP. Experimental techniques may include solid-state NMR with ^{15}N-enrichment as described in Chapter 2, neutron scattering techniques with deuterium labeled P2VP, an extension of the molecular dynamics simulations also described in Chapter 2, or fluorescence based molecular tracking, as described briefly in the following Chapter.

4.4 - Conclusion

It is thus inadvisable to use insulating layers to analyze material relaxations at timescales that would otherwise correspond to DC conductivity dominating the material response. Additionally, air bubbles may introduce artifacts at similar frequencies, without

the presence of an intentionally introduced air gap. For this reason, care must be taken in interpreting the results from the DRS measurements taken of these P2VP/OAPS composites. This necessarily requires proving that process-D is not caused solely by the presence of insulating layers that are unrelated to the dynamics of the system, particularly by comparing timescales, and fitting the peaks to a Debye process.

CHAPTER 5

5 – FLUORESCENCE MICROSCOPY TO PROBE MULTISCALE POLYMER DYNAMICS

5.1 – Introduction

When studying segmental and chain dynamics, separate techniques must often be used to probe α-relaxations and chain relaxations, except in the special case of polymers with dipole moments aligned along their chain backbone, in which case dielectric loss spectroscopy can be used to measure both.[108] Neutron spin-echo measurements can also be used to study relaxations across a range of length scales, though this technique requires highly specialized instrumentation and sophisticated deuterium labeling.[113,114] This makes the creation of a method to simultaneously measure segmental relaxation times and entire chain diffusion coefficients desirable as a complimentary technique to rheology.

Fluorescence correlation spectroscopy (FCS) was invented in the 1970s, and has since grown in popularity to study macromolecules in solution in the fields of molecular biology and polymer science.[115,116] There have been similar studies performed on polymer systems without solvent.[117–120] In FCS, fluorophore moieties are covalently bound to the macromolecule in question and observed with a magnification near the optical resolution limit of confocal microscopy. Although this does require an invasive labeling technique, the ease with which experiments can be performed in a variety of environments makes FCS a useful tool for measuring polymer chain dynamics. At a given time, the number of fluorophores in the confocal volume is measured by the intensity of emission observed in that volume. Fluorophores are typically at nanomolar concentrations, to limit their number

in the confocal volume to the order of 100 or less. From the data of measured intensity versus time, the autocorrelation function $G(\tau)$ is related to the translational diffusion coefficient, D, by

$$G(\tau) = G(0)\left(1 + \frac{4D\tau}{s^2}\right)^{-1}\left(1 + \frac{4D\tau}{u^2}\right)^{-\frac{1}{2}} \quad 5.1$$

where s and d are the lateral and vertical dimensions of the confocal volume, respectively.

Fluorescence-lifetime imaging microscopy (FLIM) is a technique that has also seen extensive use over the past 20 years in biological systems. The lifetime, quantum yield, and emission spectra of fluorophores can be strongly dependent on the system in the immediate vicinity of the fluorophore. In FLIM, a laser pulse is sent to the sample, fluorophores absorb the incoming photons by transitioning to higher energy states, then release a photon when transitioning back to the lower-energy state. This time between absorption and decay is quantified as the fluorophore lifetime and is rudimentarily measured with pulsed laser microscopes. Fluorescence lifetime is a useful measure for many properties, as it does not depend on other influences such as the absorption of photons from the sample, which is a problem when measuring intensity or spectral shifts. FLIM has been used in polymer science to measure stress in injection molded parts[121] and as a probe of segmental mobility in the region immediately surrounding the fluorophore, with dyes unattached[122–124] and attached[125,126] to the polymer in question. Similar methods have been used in polymer thin films by measuring fluorescence intensity, rather than lifetime, which is possible due to the isotropic nature of the samples and their simple geometry.[127,128] Fundamentally, both fluorescence lifetime and fluorescence intensity measurement

techniques probe the local density in the region of the fluorophore to measure T_g in polymer thin films, with T_g being observed as a change in the thermal expansion coefficient.

By combining fluorescent probe techniques, it is possible that polymer dynamics on both long and short length scales could be measured on the same instrument, which has the potential to increase throughput in measurements related to the decoupling of segmental and entire chain motion. In this study, a solution of fluorescently end-labeled polymers is characterized via FCS and FLIM. While FCS was achievable in the solution state, it may not be feasible to translate this into the melt state without highly specialized equipment. On the other hand, FLIM may be a valuable proxy for measuring polymer segment dynamics.

5.2 – Multiscale Dynamics of Polymers via Fluorescence Microscopy Techniques

5.2.a – Synthesis of Fluorescently Labeled Polymers

7-nitro-2,1,3-benzoxadiazole (NBD) was chosen as a fluorescent marker, due to its utility in determining the segmental mobility of polystyrene thin films by lifetime as shown by Kawaguchi et al.,[125] and high quantum yield to facilitate tracking via FCS. Following procedures established by Albuszis et al., 4-chloro-7-nitro-2,1,3-benzoxadiazole (NBD-Cl) was reacted with propargyl amine to form 7-Nitro-4-(prop-2-ynylamine)benzofurazan (NBD-Alkyne), as illustrated in Scheme 3.[129] 1.25 g of NBD-Cl and 0.5 nm of pyridine were dissolved in 10 mL of ethanol. To this solution, 0.44 mL of propargyl amine dissolved in 5 mL of ethanol was added dropwise, while the mixture was kept at 0°C by an ice bath. Note that both the NBD-Cl and propargyl amine must be diluted to avoid an unwanted

vigorous reaction. After 5 hours, the ethanol was evaporated. Then, the pyridine was removed via co-evaporation with 10 mL of toluene three times.

Scheme 3. Reaction of 4-chloro-7-nitro-2,1,3-benzoxadiazole (NBD-Cl) and propargyl amine in the presence of base to form 7-nitro-N-(prop-2-ynyl)-2,1,3-benzoxadiazol-4-amine (NBD-Alkyne)

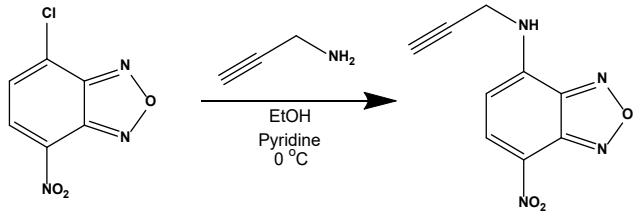

The reaction formed a black sooty product, from which a fluorescent orange product could be extracted using column chromatography, with a typical yield of ~20%. The black residue was likely caused by unwanted polymerization of the alkyne during synthesis. For chromatography, a mobile phase with a ratio of 70:30 petroleum ether to ethyl acetate was selected for the separation through a column of basic alumina. One fraction was found to fluoresce, which was collected and dried. The ^{1}H NMR spectra of this product are shown in Figure 43, indicating good separation from reagents.[129]

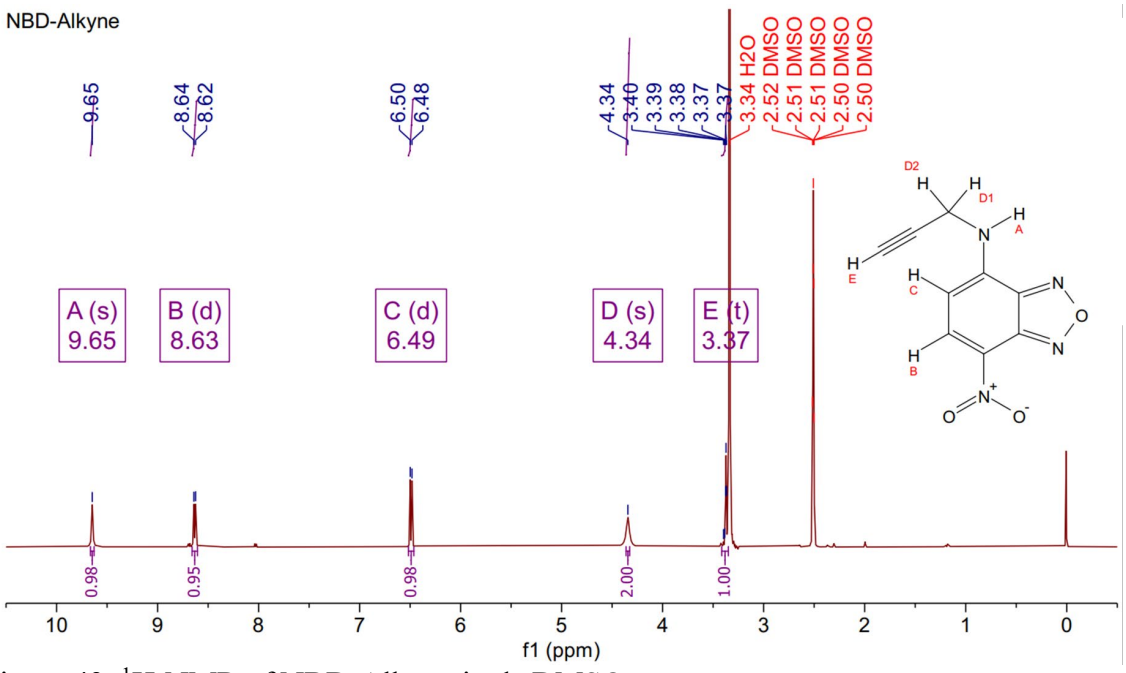

Figure 43. ^{1}H-NMR of NBD-Alkyne in d_6-DMSO.

Bromine terminated polystyrene (PS-Br, M_n=6kDa, $Đ$ = 1.3) was purchased from Polymer Source, Inc. Using an adapted procedure from Katzenstein,[130] NBD-Alkyne was attached to the PS-Br, as shown in Scheme 4. The bromine terminus was converted to azide by reaction with threefold molar excess of sodium azide in DMF to create PS-Azide, followed by threefold precipitation into methanol. This was followed by Cu(I)-mediated cycloaddition with twofold molar excess NBD-Alkyne. 200 mg of polymer, 10 mg of PMDETA, 7 mg of CuBr, and 40 mg of NBD-Alkyne was added to 4 mL of DMF in a vial. The reaction was performed at 60°C for three days, before precipitating seven times in methanol to remove unreacted NBD-Alkyne.

Scheme 4. Reaction of bromine terminated polystyrene (PS-Br) with sodium azide to form azide terminated polystyrene (PS-Azide), and subsequent reaction with NBD-Alkyne to form fluorophore-terminated polystyrene (PS-NBD).

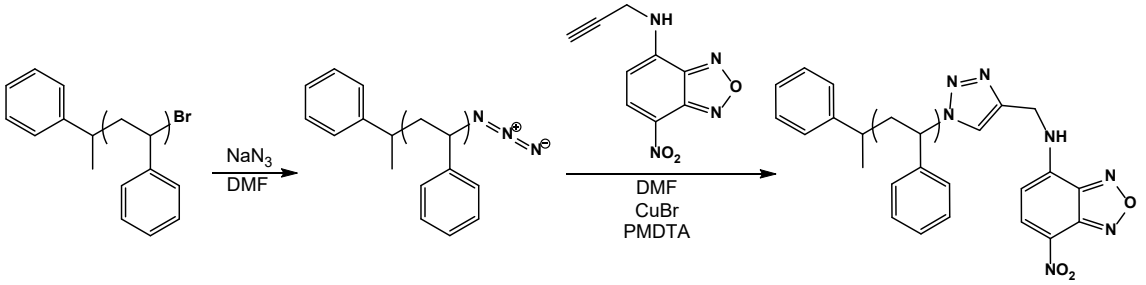

The reaction of PS-Br with sodium azide was verified via ATR-FTIR. Note the appearance of a peak at 2090 cm^{-1} in Figure 44, corresponding to an azide functional group. After reaction with NBD-Alkyne however, this peak does not appear to decrease in size, which would correspond to the disappearance of azide to form triazole groups.

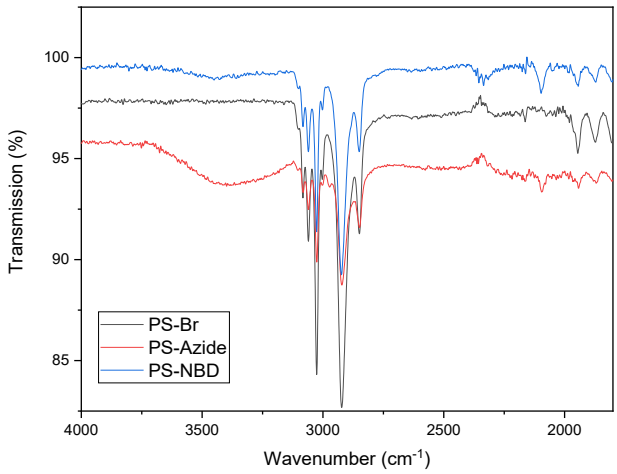

Figure 44. ATR-FTIR spectrum of PS-Br, PS-Azide, and PS-NBD. A peak from the azide terminus is immediately apparent for PS-Azide and PS-NBD, indicating that there was significant conversion of bromine to azide, but no apparent conversion of azide to NBD moiety.

Evidence for the formation of PS-NBD comes from photoluminescence spectroscopy. Photoluminescence spectroscopy was performed on a PTI QuantaMaster 8000 instrument, in glass cuvettes with THF as a solvent. The PS-NBD was excited with 465 nm light and the emission spectrum is shown in Figure 45. The emission intensity corresponds to unattached NBD-Alkyne at roughly 10 μM concentration in THF, which was used to estimate that the concentration of dye on chain ends was roughly 0.3% conversion. This is a rough estimate, and it assumes that the quantum yield of the fluorophore is unchanged upon attachment to the polymer, which may not be the case. It is also important to note that the emission spectrum of the NBD moiety is shifted to longer wavelengths when attached to the polymer, indicating a change in chemical environment, which is an additional sign that attachment was successful. To be sure that this emission was not due to unattached fluorophore entrained in the polymer, a control sample was created by mixing PS-Br with NBD-Alkyne in THF, so that no reaction would occur. This physical mixture was then separated according to the same procedure to separate unreacted

NBD-Alkyne from PS-NBD (seven precipitations in methanol). The emission spectra for this sample after separation is shown in the red dashed line in Figure 45, at the same concentration in THF as the PS-NBD. The emission is over an order of magnitude lower than that of PS-NBD, and the peak is not shifted to higher wavelengths as was observed for PS-NBD, rather, the emission wavelength matches that of unattached NBD-Alkyne. Thus, it is unlikely that the emission from PS-NBD is due to unattached NBD moieties.

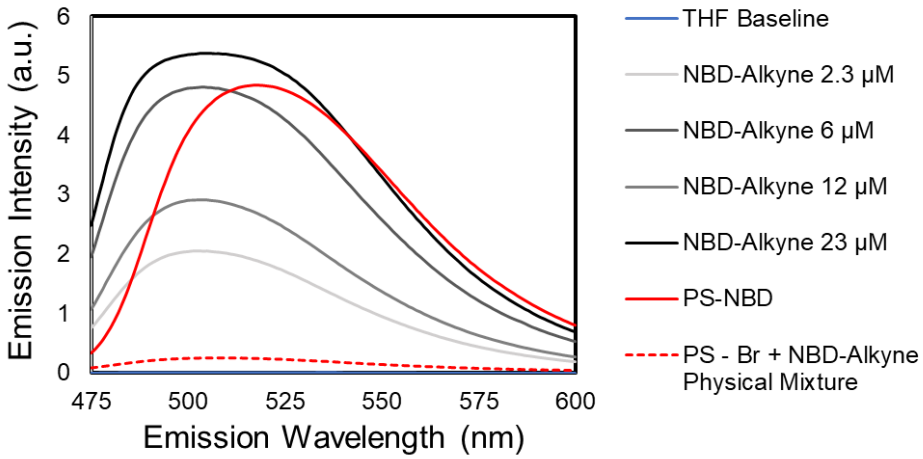

Figure 45. Photoluminescence of different components in THF, with excitation at 465 nm. Solid black lines correspond to different concentrations of free dye in solution. Solid red line corresponds to emission of PS-NBD in solution. Red dashed line corresponds to PS-Br mixed with free dye, and separated using the same precipitation techniques as were used to separate unreacted PS-Azide from PS-NBD.

5.2.b –Measuring Segment and Chain Dynamics with Fluorescence Correlation Spectroscopy and Fluorescence Lifetime Imaging Microscopy

FLIM and FCS measurements were taken on a Nikon A1SP confocal fluorescence microscope. FCS measurements were taken with 480 nm excitation wavelength, while FLIM measurements were taken with 450 nm excitation. Samples were prepared by pipetting the solution into the indentation of a depression microscope slide, covering with a coverslip, and securing with silicone adhesive. The slide was then inverted for imaging on the inverted microscope (Figure 46).

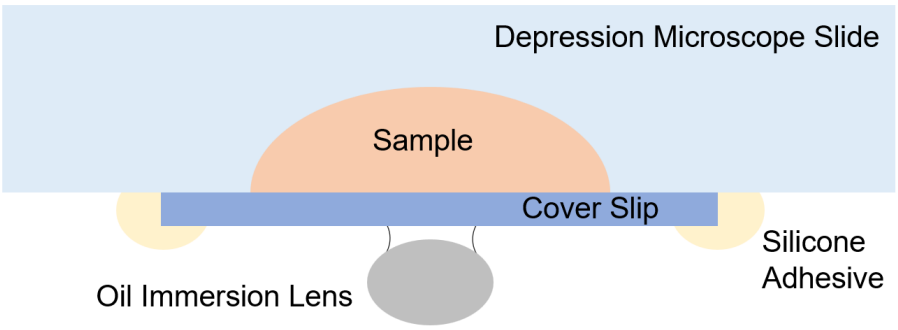

Figure 46. Schematic of inverted cover slide setup

FCS measurements were performed on PS, with polymer concentration of 50 mg/mL in THF. PS-NBD was diluted with PS-Br such that the fluorophore concentration was 1 nM, 10 nM, and 100 nM, based on the degree of conversion calculated via photoluminescence measurements. This is below the polymer overlap concentration.[131] The FCS curve for 100 nM dye concentration is shown in Figure 47. The decay time of this plot corresponds to a diffusion constant on the order of 10^{-6} cm^2/s, compared to estimates from literature[131,132] of 10^{-7} cm^2/s.

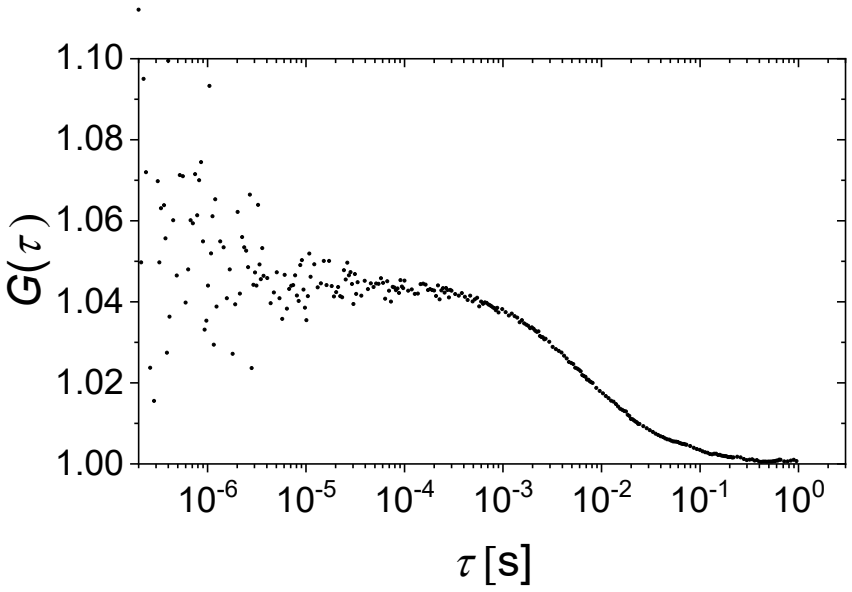

Figure 47. FCS data of the correlation function as a funciton of time for polymer of molar mass 6kDa with $Đ$ = 1.3 at 50 mg/mL in THF at room temperature, at 100 nM concentration of fluorophore.

A variety of constraints are placed on the experimental setup for FCS, which make measurement of polymer melts challenging. The primary difficulty is reaching appropriate temperatures for which diffusion coefficients can be reasonably measured on laboratory timescales for typical model polymers such as polystyrene or P2VP. Oil immersion lenses are practically necessary in FCS to keep the acquisition time reasonable, as the time required to accurately measure diffusion increases with the square of the confocal volume size. However, by putting the lens in contact with the specimen holder, the microscope will be exposed to a thermal stress, requiring specialized optics to avoid damaging the instrument.[117,118,133]

In addition to measuring diffusion with FCS, florescence lifetime was measured at an excitation wavelength of 488 nm. The PS-NBD was dissolved in THF with a concentration of 0.3 mg/mL, which corresponds to ~ 10 μM NBD concentration, while lifetime measurements can be conducted in concentrations as low as 1 nM. As shown in Figure 48**,** the lifetime ($\tau_{lifetime}$) of the NBD covalently attached to PS was determined to be 7.5 nsec at 25 °C. As a comparison, the lifetime of unattached or free dye, NBD-alkyne, was measured and its $\tau_{lifetime}$ was smaller than that of PS-NBD (5 nsec for 1nM in THF). This difference may be significant because it is reported that τ_{NBD} is reduced by only 30% as temperature is decreased by 100 K.[134] While there are complex contributions from solvent, the preliminary experiments suggest that the lifetime of NBD that is attached to PS can be measured in solution.

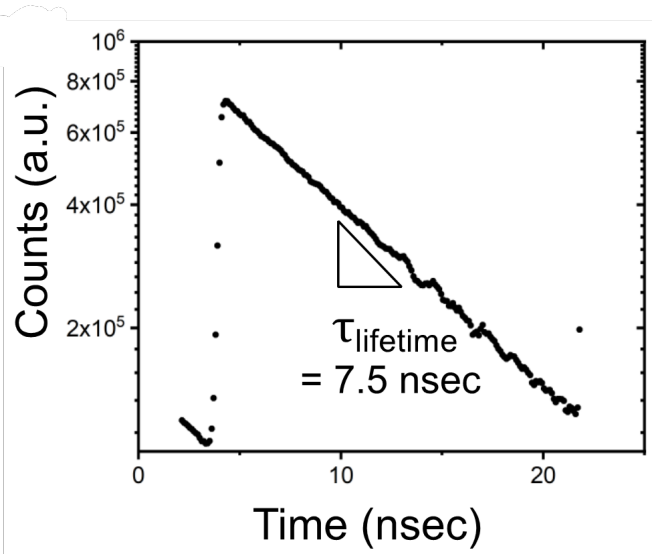

Figure 48. Lifetime ($\tau_{lifetime}$) measurement of NBD, which is covalently attached to PS in THF at room temperature

5.3 - Conclusion

Overall, fluorescence microscopy techniques can be useful for studying polymer dynamics, though they require materials that are synthesized to incorporate specific fluorophores into the polymer structure . FCS may not be appropriate to measure diffusion in polymer melts, because the relevant timescales are too long for the technique to be particularly applicable unless sample is well above T_g, which requires highly specialized equipment for most relevant polymers. Thus, Fluorescence Recovery After Patterned Photobleaching is likely a better method for measuring the diffusion of fluorescently labeled polymers in the melt state.[135,136]

CHAPTER 6

6 – CONCLUSIONS

6.1 – Summary

In this Dissertation, a range of experiments on a strongly attractive model polymer-POSS blend system have been highlighted, with particular emphasis on their glass transition temperature and dynamics. By changing the number of hydrogen bond donor/acceptor pairs in the system, the T_g increase is found to be roughly proportional to the number of interacting pairs. This behavior can be explained either by the Fox equation or more fundamental models. Results suggest that this modification does not have as significant of an effect on rheological behavior in the terminal flow regime. This is further examined with rheometry measurements of polymer nanocomposites of variable molar mass, which suggest that there is a secondary relaxation process associated with the material when the loading of POSS is high. These findings combine to give a detailed picture of how polymer-nanofiller interactions change the dynamics of polymer chains across the range of relevant length and time scales yet leave certain areas to be addressed by future investigations.

6.2 – Future Directions

Numerous research avenues are revealed or left open from this work. Techniques involving the use of fluorescent labels may also prove useful for measuring the dynamics of polymer systems across length scales, though care is needed to fundamentally understand the specific property that a fluorophore probe is sensing, and to screen out the complex interactions between fluorophores and the fillers that give POSS nanocomposites

their unique properties. Experiments attempting to identify whether the nature of the intermediate-frequency mechanical response of P2VP/OAPS is driven more by polymer-POSS or POSS-POSS interactions were inconclusive, leaving open fundamental questions about the rich dynamics of these materials unanswered. Future application-driven work may focus on the use of POSS nanocomposites as a method for templating structures formed during the rapid thermal annealing of polymer nanocomposites, leveraging the hybrid nature of the POSS molecule along with its unique effects to decouple segment and chain dynamics.

The temperature-dependent nature of these composites is critical from an academic perspective, yet much is left to be explored. Hydrogen-bonding clearly plays a critical role in the properties of the composite, with effects that may elucidate the apparent decoupling of short and long mode relaxations. Simulations were performed by collaborators to give some insight into this; however, direct experimental studies would be helpful. FTIR and NMR could be useful tools in this regard but may require modifications to the chemistry of the model system to be suitable. For FTIR to reliably distinguish hydrogen-bonded protons, the proton ought to be part of a secondary amine or an alcohol, unlike the primary amines that decorate OAPS. It would potentially be feasible to convert the OAPS amines to secondary amines by a substitution reaction with an alkyl halide, however, it would be critical to avoid forming the tertiary amine yet avoid introducing so much steric hinderance that hydrogen bonds were no longer feasible to form with the matrix polymer. Alternatively, phenolic POSS could be synthesized via a variety of pathways to add a hydroxy group to the phenyl rings of OPS. Solid-state NMR may also be useful, but higher sensitivity is required, along with temperature control well into the melt state. Analogous

materials with low T_g may be interesting in this regard, as would materials enriched with NMR active isotopes such as ^{15}N.

6.3 – Outlook

Broadly, the fundamental physical understanding of polymer nanocomposites has taken great strides over the last decade, with diligent experimentation, simulation, and theory advancing in tandem. In particular, the emerging paradigm of "bound polymer layers" and "interfacial polymer layers" have unified and clarified many of the results seen in experiments and simulations. This has provided a clear framework for understanding the observed differences and similarities between typical larger (~10 nm) polymer nanocomposites and the sorts of polymer-POSS nanocomposites presented in this dissertation. While larger fillers allow for a polymer chain to completely adsorb to its surface, POSS fillers (an order of magnitude smaller) differ because the entropic penalty for a single chain to decorate a single filler is too great. In order to completely unify our understanding of the structure, dynamics, and properties of polymer nanocomposites, theoretical models which are applicable across the range of filler length scales are needed. Furthermore, the results of these models and experiments must be considered in the face of other open questions in the field of polymer physics, particularly the nature of the glass-transition in polymer and colloidal systems.

The fruits of this insight will not be purely academic. As highlighted by the experimental work presented here, the formulation of polymer nanocomposites can dramatically alter their dynamics across the range of length- and timescales relevant for phenomena from the glass transition to entire chain diffusion. Industrially, this insight is already widely harnessed to vary the rheological and thixotropic behavior for advanced

applications in 3D printing and adhesives which require precisely tuned viscoelastic properties. A complete fundamental model which can account for a variety of fillers across a range of shapes and sizes will allow these applications to be advanced even further, as practitioners will be able to select *a priori* fillers which will give the desired properties for a given application.

BIBLIOGRAPHY

(1) Kumar, S. K.; Benicewicz, B. C.; Vaia, R. A.; Winey, K. I. 50th Anniversary Perspective: Are Polymer Nanocomposites Practical for Applications? *Macromolecules* **2017**, *50* (3), 714–731. https://doi.org/10.1021/acs.macromol.6b02330.

(2) Farahani, R. D.; Dubé, M.; Therriault, D. Three-Dimensional Printing of Multifunctional Nanocomposites: Manufacturing Techniques and Applications. *Adv. Mater.* **2016**, *28* (28), 5794–5821. https://doi.org/10.1002/adma.201506215.

(3) Holt, A. P.; Sangoro, J. R.; Wang, Y.; Agapov, A. L.; Sokolov, A. P. Chain and Segmental Dynamics of Poly(2-Vinylpyridine) Nanocomposites. *Macromolecules* **2013**, *46* (10), 4168–4173. https://doi.org/10.1021/ma400418b.

(4) Bailey, E. J.; Griffin, P. J.; Tyagi, M.; Winey, K. I. Segmental Diffusion in Attractive Polymer Nanocomposites: A Quasi-Elastic Neutron Scattering Study. *Macromolecules* **2019**, *52* (2), 669–678. https://doi.org/10.1021/acs.macromol.8b01716.

(5) Bailey, E. J.; Griffin, P. J.; Composto, R. J.; Winey, K. I. Multiscale Dynamics of Small, Attractive Nanoparticles and Entangled Polymers in Polymer Nanocomposites. *Macromolecules* **2019**, *52* (5), 2181–2188. https://doi.org/10.1021/acs.macromol.8b02646.

(6) Zhang, T.; Winey, K. I.; Riggleman, R. A. Polymer Conformations and Dynamics under Confinement with Two Length Scales. *Macromolecules* **2019**, *52* (1), 217–226. https://doi.org/10.1021/acs.macromol.8b01779.

(7) Emamy, H.; Kumar, S. K.; Starr, F. W. Diminishing Interfacial Effects with Decreasing Nanoparticle Size in Polymer-Nanoparticle Composites. *Phys. Rev. Lett.* **2018**, *121* (20), 207801. https://doi.org/10.1103/PhysRevLett.121.207801.

(8) Carroll, B.; Bocharova, V.; Carrillo, J.-M. Y.; Kisliuk, A.; Cheng, S.; Yamamoto, U.; Schweizer, K. S.; Sumpter, B. G.; Sokolov, A. P. Diffusion of Sticky Nanoparticles in a Polymer Melt: Crossover from Suppressed to Enhanced Transport. *Macromolecules* **2018**, *51* (6), 2268–2275. https://doi.org/10.1021/acs.macromol.7b02695.

(9) Song, Y.; Zheng, Q. Size-Dependent Linear Rheology of Silica Filled Poly(2-Vinylpyridine). *Polymer* **2017**, *130*, 74–78. https://doi.org/10.1016/j.polymer.2017.09.070.

(10) Cheng, S.; Xie, S.-J.; Carrillo, J.-M. Y.; Carroll, B.; Martin, H.; Cao, P.-F.; Dadmun, M. D.; Sumpter, B. G.; Novikov, V. N.; Schweizer, K. S.; Sokolov, A. P. Big Effect of Small Nanoparticles: A Shift in Paradigm for Polymer Nanocomposites. *ACS Nano* **2017**, *11* (1), 752–759. https://doi.org/10.1021/acsnano.6b07172.

(11) Choi, J.; Hore, M. J. A.; Meth, J. S.; Clarke, N.; Winey, K. I.; Composto, R. J. Universal Scaling of Polymer Diffusion in Nanocomposites. *ACS Macro Lett.* **2013**, *2* (6), 485–490. https://doi.org/10.1021/mz400064w.

(12) Bocharova, V.; Genix, A.-C.; Carrillo, J.-M. Y.; Kumar, R.; Carroll, B.; Erwin, A.; Voylov, D.; Kisliuk, A.; Wang, Y.; Sumpter, B. G.; Sokolov, A. P. Addition of Short Polymer Chains Mechanically Reinforces Glassy Poly(2-Vinylpyridine)–Silica Nanoparticle Nanocomposites. *ACS Appl. Nano Mater.* **2020**, *3* (4), 3427–3438. https://doi.org/10.1021/acsanm.0c00180.
(13) Genix, A.-C.; Bocharova, V.; Kisliuk, A.; Carroll, B.; Zhao, S.; Oberdisse, J.; Sokolov, A. P. Enhancing the Mechanical Properties of Glassy Nanocomposites by Tuning Polymer Molecular Weight. *ACS Appl. Mater. Interfaces* **2018**, *10* (39), 33601–33610. https://doi.org/10.1021/acsami.8b13109.
(14) Cheng, S.; Holt, A. P.; Wang, H.; Fan, F.; Bocharova, V.; Martin, H.; Etampawala, T.; White, B. T.; Saito, T.; Kang, N.-G.; Dadmun, M. D.; Mays, J. W.; Sokolov, A. P. Unexpected Molecular Weight Effect in Polymer Nanocomposites. *Phys. Rev. Lett.* **2016**, *116* (3), 038302. https://doi.org/10.1103/PhysRevLett.116.038302.
(15) Bansal, A.; Yang, H.; Li, C.; Cho, K.; Benicewicz, B. C.; Kumar, S. K.; Schadler, L. S. Quantitative Equivalence between Polymer Nanocomposites and Thin Polymer Films. *Nat. Mater.* **2005**, *4* (9), 693–698. https://doi.org/10.1038/nmat1447.
(16) Cheng, S.; Carroll, B.; Lu, W.; Fan, F.; Carrillo, J.-M. Y.; Martin, H.; Holt, A. P.; Kang, N.-G.; Bocharova, V.; Mays, J. W.; Sumpter, B. G.; Dadmun, M.; Sokolov, A. P. Interfacial Properties of Polymer Nanocomposites: Role of Chain Rigidity and Dynamic Heterogeneity Length Scale. *Macromolecules* **2017**, *50* (6), 2397–2406. https://doi.org/10.1021/acs.macromol.6b02816.
(17) Zheng, Z.; Li, F.; Liu, J.; Pastore, R.; Raos, G.; Wu, Y.; Zhang, L. Effects of Chemically Heterogeneous Nanoparticles on Polymer Dynamics: Insights from Molecular Dynamics Simulations. *Soft Matter* **2018**, *14* (7), 1219–1226. https://doi.org/10.1039/C7SM02414B.
(18) Trazkovich, A. J.; Wendt, M. F.; Hall, L. M. Effect of Copolymer Sequence on Local Viscoelastic Properties near a Nanoparticle. *Macromolecules* **2019**, *52* (2), 513–527. https://doi.org/10.1021/acs.macromol.8b02136.
(19) Jhalaria, M.; Jimenez, A. M.; Mathur, R.; Tekell, M. C.; Huang, Y.; Narayanan, S.; Benicewicz, B. C.; Kumar, S. K. Long-Term Aging in Miscible Polymer Nanocomposites. *Macromolecules* **2022**, *55* (11), 4502–4515. https://doi.org/10.1021/acs.macromol.2c00332.
(20) Lin, E. Y.; Frischknecht, A. L.; Winey, K. I.; Riggleman, R. A. Effect of Surface Properties and Polymer Chain Length on Polymer Adsorption in Solution. *J. Chem. Phys.* **2021**, *155* (3), 034701. https://doi.org/10.1063/5.0052121.
(21) Oh, S. M.; Lee, C. H.; Kim, S. Y. Processing Method Determines the Long-Term Stability of Particle Dispersions in Concentrated Nanoparticle/Polymer Suspensions. *Soft Matter* **2022**, *18* (4), 841–848. https://doi.org/10.1039/D1SM01428E.
(22) Oh, S. M.; Kim, S. Y. Intensified Nonequilibrium Effect of Polymer Nanocomposites with Decreasing Nanoparticle Size. *ACS Appl. Mater. Interfaces* **2023**, *15* (3), 4527–4537. https://doi.org/10.1021/acsami.2c20156.
(23) Popov, I.; Carroll, B.; Bocharova, V.; Genix, A.-C.; Cheng, S.; Khamzin, A.; Kisliuk, A.; Sokolov, A. P. Strong Reduction in Amplitude of the Interfacial Segmental Dynamics in Polymer Nanocomposites. *Macromolecules* **2020**, *53* (10), 4126–4135. https://doi.org/10.1021/acs.macromol.0c00496.

(24) Zhang, W.; Emamy, H.; Pazmiño Betancourt, B. A.; Vargas-Lara, F.; Starr, F. W.; Douglas, J. F. The Interfacial Zone in Thin Polymer Films and around Nanoparticles in Polymer Nanocomposites. *J. Chem. Phys.* **2019**, *151* (12), 124705. https://doi.org/10.1063/1.5119269.
(25) Yang, S.; Liu, S.; Narayanan, S.; Zhang, C.; Akcora, P. Chemical Heterogeneity in Interfacial Layers of Polymer Nanocomposites. *Soft Matter* **2018**, *14* (23), 4784–4791. https://doi.org/10.1039/C8SM00663F.
(26) Cheng, S.; Carroll, B.; Bocharova, V.; Carrillo, J.-M.; Sumpter, B. G.; Sokolov, A. P. Focus: Structure and Dynamics of the Interfacial Layer in Polymer Nanocomposites with Attractive Interactions. *J. Chem. Phys.* **2017**, *146* (20), 203201. https://doi.org/10.1063/1.4978504.
(27) Cheng, S.; Bocharova, V.; Belianinov, A.; Xiong, S.; Kisliuk, A.; Somnath, S.; Holt, A. P.; Ovchinnikova, O. S.; Jesse, S.; Martin, H.; Etampawala, T.; Dadmun, M.; Sokolov, A. P. Unraveling the Mechanism of Nanoscale Mechanical Reinforcement in Glassy Polymer Nanocomposites. *Nano Lett.* **2016**, *16* (6), 3630–3637. https://doi.org/10.1021/acs.nanolett.6b00766.
(28) Cheng, S.; Mirigian, S.; Carrillo, J.-M. Y.; Bocharova, V.; Sumpter, B. G.; Schweizer, K. S.; Sokolov, A. P. Revealing Spatially Heterogeneous Relaxation in a Model Nanocomposite. *J. Chem. Phys.* **2015**, *143* (19), 194704. https://doi.org/10.1063/1.4935595.
(29) Jouault, N.; Moll, J. F.; Meng, D.; Windsor, K.; Ramcharan, S.; Kearney, C.; Kumar, S. K. Bound Polymer Layer in Nanocomposites. *ACS Macro Lett.* **2013**, *2* (5), 371–374. https://doi.org/10.1021/mz300646a.
(30) Starr, F. W.; Schrøder, T. B.; Glotzer, S. C. Molecular Dynamics Simulation of a Polymer Melt with a Nanoscopic Particle. *Macromolecules* **2002**, *35* (11), 4481–4492. https://doi.org/10.1021/ma010626p.
(31) Lin, E. Y.; Frischknecht, A. L.; Riggleman, R. A. Origin of Mechanical Enhancement in Polymer Nanoparticle (NP) Composites with Ultrahigh NP Loading. *Macromolecules* **2020**, *53* (8), 2976–2982. https://doi.org/10.1021/acs.macromol.9b02733.
(32) Ondreas, F.; Lepcio, P.; Zboncak, M.; Zarybnicka, K.; Govaert, L. E.; Jancar, J. Effect of Nanoparticle Organization on Molecular Mobility and Mechanical Properties of Polymer Nanocomposites. *Macromolecules* **2019**, *52* (16), 6250–6259. https://doi.org/10.1021/acs.macromol.9b01197.
(33) Oh, S. M.; Abbasi, M.; Shin, T. J.; Saalwächter, K.; Kim, S. Y. Initial Solvent-Driven Nonequilibrium Effect on Structure, Properties, and Dynamics of Polymer Nanocomposites. *Phys. Rev. Lett.* **2019**, *123* (16), 167801. https://doi.org/10.1103/PhysRevLett.123.167801.
(34) Chen, Q.; Gong, S.; Moll, J.; Zhao, D.; Kumar, S. K.; Colby, R. H. Mechanical Reinforcement of Polymer Nanocomposites from Percolation of a Nanoparticle Network. *ACS Macro Lett.* **2015**, *4* (4), 398–402. https://doi.org/10.1021/acsmacrolett.5b00002.
(35) Bailey, E. J.; Griffin, P. J.; Composto, R. J.; Winey, K. I. Characterizing the Areal Density and Desorption Kinetics of Physically Adsorbed Polymer in Polymer Nanocomposite Melts. *Macromolecules* **2020**, *53* (7), 2744–2753. https://doi.org/10.1021/acs.macromol.9b02205.

(36) Li, G.; Wang, L.; Ni, H.; Pittman, C. U. Polyhedral Oligomeric Silsesquioxane (POSS) Polymers and Copolymers: A Review. *J. Inorg. Organomet. Polym.* **2001**, *11* (3), 123–154. https://doi.org/10.1023/A:1015287910502.
(37) Tanaka, K.; Adachi, S.; Chujo, Y. Structure–Property Relationship of Octa-Substituted POSS in Thermal and Mechanical Reinforcements of Conventional Polymers. *J. Polym. Sci. Part Polym. Chem.* **2009**, *47* (21), 5690–5697. https://doi.org/10.1002/pola.23612.
(38) Haddad, T. S.; Lichtenhan, J. D. Hybrid Organic−Inorganic Thermoplastics: Styryl-Based Polyhedral Oligomeric Silsesquioxane Polymers. *Macromolecules* **1996**, *29* (22), 7302–7304. https://doi.org/10.1021/ma960609d.
(39) Romo–Uribe, A.; Mather, P. T.; Haddad, T. S.; Lichtenhan, J. D. Viscoelastic and morphological behavior of hybrid styryl-based polyhedral oligomeric silsesquioxane (POSS) copolymers. *J. Polym. Sci. Part B Polym. Phys.* **1998**, *36* (11), 1857–1872. https://doi.org/10.1002/(SICI)1099-0488(199808)36:11<1857::AID-POLB7>3.0.CO;2-N.
(40) Tegou, E.; Bellas, V.; Gogolides, E.; Argitis, P. Polyhedral Oligomeric Silsesquioxane (POSS) Acrylate Copolymers for Microfabrication: Properties and Formulation of Resist Materials. *Microelectron. Eng.* **2004**, *73–74*, 238–243. https://doi.org/10.1016/j.mee.2004.02.047.
(41) Hu, W.-H.; Huang, K.-W.; Chiou, C.-W.; Kuo, S.-W. Complementary Multiple Hydrogen Bonding Interactions Induce the Self-Assembly of Supramolecular Structures from Heteronucleobase-Functionalized Benzoxazine and Polyhedral Oligomeric Silsesquioxane Nanoparticles. *Macromolecules* **2012**, *45* (22), 9020–9028. https://doi.org/10.1021/ma302077x.
(42) Romo-Uribe, A. Viscoelastic Behavior of Unentangled POSS–Styrene Nanocomposites and the Modification of Macromolecular Dynamics. *Macromolecules* **2017**, *50* (18), 7177–7189. https://doi.org/10.1021/acs.macromol.7b01645.
(43) Romo-Uribe, A.; Reyes-Mayer, A.; Paredes-Pérez, M.; Lichtenhan, J.; Yañez-Lino, M.; Sarmiento-Bustos, E. POSS Driven Chain Disentanglements, Decreased the Melt Viscosity and Reduced O2 Transmission in Polyethylene. *Polymer* **2019**, *165*, 61–71. https://doi.org/10.1016/j.polymer.2019.01.024.
(44) Tamaki, R.; Tanaka, Y.; Asuncion, M. Z.; Choi, J.; Laine, R. M. Octa(Aminophenyl)Silsesquioxane as a Nanoconstruction Site. *J. Am. Chem. Soc.* **2001**, *123* (49), 12416–12417. https://doi.org/10.1021/ja011781m.
(45) Tanaka, K.; Adachi, S.; Chujo, Y. Side-Chain Effect of Octa-Substituted POSS Fillers on Refraction in Polymer Composites. *J. Polym. Sci. Part Polym. Chem.* **2010**, *48* (24), 5712–5717. https://doi.org/10.1002/pola.24370.
(46) Godnjavec, J.; Znoj, B.; Veronovski, N.; Venturini, P. Polyhedral Oligomeric Silsesquioxanes as Titanium Dioxide Surface Modifiers for Transparent Acrylic UV Blocking Hybrid Coating. *Prog. Org. Coat.* **2012**, *74* (4), 654–659. https://doi.org/10.1016/j.porgcoat.2011.09.032.
(47) Li, C.; Li, X.; Tao, C.; Ren, L.; Zhao, Y.; Bai, S.; Yuan, X. Amphiphilic Antifogging/Anti-Icing Coatings Containing POSS-PDMAEMA-b-PSBMA. *ACS Appl. Mater. Interfaces* **2017**, *9* (27), 22959–22969. https://doi.org/10.1021/acsami.7b05286.

(48) Anand Ganesh, V.; Sreekumaran Nair, A.; Kumar Raut, H.; Tan, T. T. Y.; He, C.; Ramakrishna, S.; Xu, J. Superhydrophobic Fluorinated POSS–PVDF-HFP Nanocomposite Coating on Glass by Electrospinning. *J. Mater. Chem.* **2012**, *22* (35), 18479–18485. https://doi.org/10.1039/C2JM33088A.
(49) Yamamoto, U.; Carrillo, J.-M. Y.; Bocharova, V.; Sokolov, A. P.; Sumpter, B. G.; Schweizer, K. S. Theory and Simulation of Attractive Nanoparticle Transport in Polymer Melts. *Macromolecules* **2018**, *51* (6), 2258–2267. https://doi.org/10.1021/acs.macromol.7b02694.
(50) R. Amaral, A. J.; Pasparakis, G. Stimuli Responsive Self-Healing Polymers: Gels, Elastomers and Membranes. *Polym. Chem.* **2017**, *8* (42), 6464–6484. https://doi.org/10.1039/C7PY01386H.
(51) Fox, T. G. Influence of Diluent and of Copolymer Composition on the Glass Temperature of a Polymer System. *Bull Am Phys Soc* **1956**, *1*, 123.
(52) Lipson, J. E. G. Global and Local Views of the Glass Transition in Mixtures. *Macromolecules* **2020**, *53* (17), 7219–7223. https://doi.org/10.1021/acs.macromol.0c01455.
(53) Couchman, P. R.; Karasz, F. E. A Classical Thermodynamic Discussion of the Effect of Composition on Glass-Transition Temperatures. *Macromolecules* **1978**, *11* (1), 117–119. https://doi.org/10.1021/ma60061a021.
(54) Gordon, J. M.; Rouse, G. B.; Gibbs, J. H.; Risen, W. M. The Composition Dependence of Glass Transition Properties. *J. Chem. Phys.* **1977**, *66* (11), 4971–4976. https://doi.org/10.1063/1.433798.
(55) Gibbs, J. H.; DiMarzio, E. A. Nature of the Glass Transition and the Glassy State. *J. Chem. Phys.* **1958**, *28* (3), 373–383. https://doi.org/10.1063/1.1744141.
(56) Jayaraman, A.; Klok, H.-A. ACS Polymers Au's Grand Challenges in Polymer Science. *ACS Polym. Au* **2023**, *3* (1), 1–4. https://doi.org/10.1021/acspolymersau.3c00001.
(57) Lodge, T. Celebrating 50 Years of Macromolecules. *Macromolecules* **2017**, *50* (24), 9525–9527. https://doi.org/10.1021/acs.macromol.7b02507.
(58) Dyre, J. C.; Hechsher, T.; Niss, K. A Brief Critique of the Adam–Gibbs Entropy Model. *J. Non-Cryst. Solids* **2009**, *355* (10), 624–627. https://doi.org/10.1016/j.jnoncrysol.2009.01.039.
(59) Raftopoulos, K. N.; Pielichowski, K. Segmental Dynamics in Hybrid Polymer/POSS Nanomaterials. *Prog. Polym. Sci.* **2016**, *52*, 136–187. https://doi.org/10.1016/j.progpolymsci.2015.01.003.
(60) Stukalin, E. B.; Douglas, J. F.; Freed, K. F. Application of the Entropy Theory of Glass Formation to Poly(α-Olefins). *J. Chem. Phys.* **2009**, *131* (11), 114905. https://doi.org/10.1063/1.3216109.
(61) Lang, R. J.; Merling, W. L.; Simmons, D. S. Combined Dependence of Nanoconfined T_g on Interfacial Energy and Softness of Confinement. *ACS Macro Lett.* **2014**, *3* (8), 758–762. https://doi.org/10.1021/mz500361v.
(62) Ghosh, A.; Samanta, S.; Ge, S.; Sokolov, A. P.; Schweizer, K. S. Influence of Attractive Functional Groups on the Segmental Dynamics and Glass Transition in Associating Polymers. *Macromolecules* **2022**. https://doi.org/10.1021/acs.macromol.2c00080.

(63) Song, Z.; Rodríguez-Tinoco, C.; Mathew, A.; Napolitano, S. Fast Equilibration Mechanisms in Disordered Materials Mediated by Slow Liquid Dynamics. *Sci. Adv.* **2022**, *8* (15), 7154. https://doi.org/10.1126/sciadv.abm7154.
(64) Di Lisio, V.; Gallino, I.; Riegler, S. S.; Frey, M.; Neuber, N.; Kumar, G.; Schroers, J.; Busch, R.; Cangialosi, D. Size-Dependent Vitrification in Metallic Glasses. *Nat. Commun.* **2023**, *14* (1), 4698. https://doi.org/10.1038/s41467-023-40417-4.
(65) Di Lisio, V.; Stavropoulou, V.-M.; Cangialosi, D. Physical Aging in Molecular Glasses beyond the α Relaxation. *J. Chem. Phys.* **2023**, *159* (6), 064505. https://doi.org/10.1063/5.0157994.
(66) Cangialosi, D.; Boucher, V. M.; Alegría, A.; Colmenero, J. Direct Evidence of Two Equilibration Mechanisms in Glassy Polymers. *Phys. Rev. Lett.* **2013**, *111* (9), 095701. https://doi.org/10.1103/PhysRevLett.111.095701.
(67) Koh, Y. P.; Simon, S. L. Enthalpy Recovery of Polystyrene: Does a Long-Term Aging Plateau Exist? *Macromolecules* **2013**, *46* (14), 5815–5821. https://doi.org/10.1021/ma4011236.
(68) Jin, S.; McKenna, G. B. Anomalous Structural Recovery in the near Glass Transition Range in a Polymer Glass: Data Revisited in Light of Temperature Variability in Vacuum Oven-Based Experiments*. *Polym. Eng. Sci.* **2022**, *62* (4), 1124–1136. https://doi.org/10.1002/pen.25911.
(69) Cangialosi, D.; Alegría, A.; Colmenero, J. Comment on "Anomalous Structural Recovery in the near Glass Transition Range in a Polymer Glass: Data Revisited in Light of Temperature Variability in Vacuum Oven-Based Experiments." *Polym. Eng. Sci.* **2022**, *62* (8), 2716–2721. https://doi.org/10.1002/pen.26054.
(70) Young, W. W.; Saez, J. P.; Katsumata, R. Rationalizing the Composition Dependence of Glass Transition Temperatures in Amorphous Polymer/POSS Composites. *ACS Macro Lett.* **2021**, *10* (11), 1404–1409. https://doi.org/10.1021/acsmacrolett.1c00597.
(71) Young, W. W.; Shi, R.; Jia, X.-M.; Qian, H.-J.; Katsumata, R. Relating the Degree of Nanofiller Functionality to the Glass Transition Temperature and Structure in a Polymer–Polyhedral Oligomeric Silsesquioxane Nanocomposite. *Macromolecules* **2022**, *55* (12), 4891–4898. https://doi.org/10.1021/acs.macromol.2c00646.
(72) Baxandall, L. G. Dynamics of Reversibly Crosslinked Chains. *Macromolecules* **1989**, *22* (4), 1982–1988. https://doi.org/10.1021/ma00194a076.
(73) Leibler, L.; Rubinstein, M.; Colby, R. H. Dynamics of Reversible Networks. *Macromolecules* **1991**, *24* (16), 4701–4707. https://doi.org/10.1021/ma00016a034.
(74) Rubinstein, M.; Semenov, A. N. Dynamics of Entangled Solutions of Associating Polymers. *Macromolecules* **2001**, *34* (4), 1058–1068. https://doi.org/10.1021/ma0013049.
(75) Rubinstein, M.; Semenov, A. N. Thermoreversible Gelation in Solutions of Associating Polymers. 2. Linear Dynamics. *Macromolecules* **1998**, *31* (4), 1386–1397. https://doi.org/10.1021/ma970617+.
(76) You, W.; Yu, W. Slow Linear Viscoelastic Relaxation of Polymer Nanocomposites: Contribution from Confined Diffusion of Nanoparticles. *Macromolecules* **2019**, *52* (23), 9094–9104. https://doi.org/10.1021/acs.macromol.9b01538.

(77) Zhou, Y.; Schweizer, K. S. Theory for the Elementary Time Scale of Stress Relaxation in Polymer Nanocomposites. *ACS Macro Lett.* **2022**, 199–204. https://doi.org/10.1021/acsmacrolett.1c00732.
(78) Zhang, X.; Zhao, S.; Xin, Z. The Chain Dis-Entanglement Effect of Polyhedral Oligomeric Silsesquioxanes (POSS) on Ultra-High Molecular Weight Polyethylene (UHMWPE). *Polymer* **2020**, *202*, 122631. https://doi.org/10.1016/j.polymer.2020.122631.
(79) Heydarnezhad, H. R.; Mohammadi, N.; Alegria, A. Non-Einstein Rheology in Segmented Polyurethane Nanocomposites. *Macromolecules* **2021**. https://doi.org/10.1021/acs.macromol.0c02503.
(80) Kropka, J. M.; Putz, K. W.; Pryamitsyn, V.; Ganesan, V.; Green, P. F. Origin of Dynamical Properties in PMMA−C60 Nanocomposites. *Macromolecules* **2007**, *40* (15), 5424–5432. https://doi.org/10.1021/ma070407p.
(81) Kropka, J. M.; Garcia Sakai, V.; Green, P. F. Local Polymer Dynamics in Polymer−C60 Mixtures. *Nano Lett.* **2008**, *8* (4), 1061–1065. https://doi.org/10.1021/nl072980s.
(82) Kopesky, E. T.; Haddad, T. S.; Cohen, R. E.; McKinley, G. H. Thermomechanical Properties of Poly(Methyl Methacrylate)s Containing Tethered and Untethered Polyhedral Oligomeric Silsesquioxanes. *Macromolecules* **2004**, *37* (24), 8992–9004. https://doi.org/10.1021/ma048934l.
(83) Kopesky, E. T.; Haddad, T. S.; McKinley, G. H.; Cohen, R. E. Miscibility and Viscoelastic Properties of Acrylic Polyhedral Oligomeric Silsesquioxane–Poly(Methyl Methacrylate) Blends. *Polymer* **2005**, *46* (13), 4743–4752. https://doi.org/10.1016/j.polymer.2005.04.001.
(84) Kuo, S.-W.; Lin, H.-C.; Huang, W.-J.; Huang, C.-F.; Chang, F.-C. Hydrogen Bonding Interactions and Miscibility between Phenolic Resin and Octa(Acetoxystyryl) Polyhedral Oligomeric Silsesquioxane (AS-POSS) Nanocomposites. *J. Polym. Sci. Part B Polym. Phys.* **2006**, *44* (4), 673–686. https://doi.org/10.1002/polb.20731.
(85) Bailey, E. J.; Winey, K. I. Dynamics of Polymer Segments, Polymer Chains, and Nanoparticles in Polymer Nanocomposite Melts: A Review. *Prog. Polym. Sci.* **2020**, 101242. https://doi.org/10.1016/j.progpolymsci.2020.101242.
(86) Bryson, K. C. Controlling the Assembly of Nanoparticles in Polymer Blends, University of Massachusettes Amherst, 2016.
(87) Wu, Y.; Liu, L.; Yang, R.; Zhang, W. Synthesis and Characterization of Low-Functional Nitrated and Aminated Octa(Phenyl) Silsesquioxane. *ChemistrySelect* **2019**, *4* (10), 2941–2948. https://doi.org/10.1002/slct.201900272.
(88) Wu, Y.; Liu, L.; Yang, R.; Zhang, W. Synthesis and Characterization of Low-Functional Nitrated and Aminated Octa(Phenyl) Silsesquioxane. *ChemistrySelect* **2019**, *4* (10), 2941–2948. https://doi.org/10.1002/slct.201900272.
(89) Jouault, N.; Kumar, S. K.; Smalley, R. J.; Chi, C.; Moneta, R.; Wood, B.; Salerno, H.; Melnichenko, Y. B.; He, L.; Guise, W. E.; Hammouda, B.; Crawford, M. K. Do Very Small POSS Nanoparticles Perturb S-PMMA Chain Conformations? *Macromolecules* **2018**, *51* (14), 5278–5293. https://doi.org/10.1021/acs.macromol.8b00432.

(90) Jia, X.-M.; Qian, H.-J.; Lu, Z.-Y. The Interfacial Structure and Dynamics in a Polymer Nanocomposite Containing Small Attractive Nanoparticles: A Full Atomistic Molecular Dynamics Simulation Study. *Phys. Chem. Chem. Phys.* **2020**, *22* (20), 11400–11408. https://doi.org/10.1039/D0CP00799D.
(91) Li, S.; Simon, G. P.; Matisons, J. G. Morphology of Blends Containing High Concentrations of POSS Nanoparticles in Different Polymer Matrices. *Polym. Eng. Sci.* **2010**, *50* (5), 991–999. https://doi.org/10.1002/pen.21612.
(92) Starr, F. W.; Douglas, J. F.; Meng, D.; Kumar, S. K. Bound Layers "Cloak" Nanoparticles in Strongly Interacting Polymer Nanocomposites. *ACS Nano* **2016**, *10* (12), 10960–10965. https://doi.org/10.1021/acsnano.6b05683.
(93) Shimizu, S.; Watanabe, N.; Kataoka, T.; Shoji, T.; Abe, N.; Morishita, S.; Ichimura, H. Pyridine and Pyridine Derivatives. In *Ullmann's Encyclopedia of Industrial Chemistry*; John Wiley & Sons, Ltd, 2000. https://doi.org/10.1002/14356007.a22_399.
(94) Müller, M.; Seidel, U.; Stadler, R. Influence of Hydrogen Bonding on the Viscoelastic Properties of Thermoreversible Networks: Analysis of the Local Complex Dynamics. *Polymer* **1995**, *36* (16), 3143–3150. https://doi.org/10.1016/0032-3861(95)97877-I.
(95) Wang, F. C.; Feve, M.; Lam, T. M.; Pascault, J.-P. FTIR Analysis of Hydrogen Bonding in Amorphous Linear Aromatic Polyurethanes. I. Influence of Temperature. *J. Polym. Sci. Part B Polym. Phys.* **1994**, *32* (8), 1305–1313. https://doi.org/10.1002/polb.1994.090320801.
(96) Jayaraman, A. 100th Anniversary of Macromolecular Science Viewpoint: Modeling and Simulation of Macromolecules with Hydrogen Bonds: Challenges, Successes, and Opportunities. *ACS Macro Lett.* **2020**, 656–665. https://doi.org/10.1021/acsmacrolett.0c00134.
(97) Mikkelsen, M.; Eliasen, K. L.; Lindemann, N.; Moch, K.; Böhmer, R.; Karimi-Varzaneh, H. A.; Lacayo-Pineda, J.; Jakobsen, B.; Niss, K.; Christensen, T.; Hecksher, T. Piezoelectric Shear Rheometry: Further Developments in Experimental Implementation and Data Extraction. *J. Rheol.* **2022**, *66* (5), 983–1003. https://doi.org/10.1122/8.0000379.
(98) Schroyen, B.; Vlassopoulos, D.; Van Puyvelde, P.; Vermant, J. Bulk Rheometry at High Frequencies: A Review of Experimental Approaches. *Rheol. Acta* **2020**, *59* (1), 1–22. https://doi.org/10.1007/s00397-019-01172-w.
(99) Hecksher, T.; Torchinsky, D. H.; Klieber, C.; Johnson, J. A.; Dyre, J. C.; Nelson, K. A. Toward Broadband Mechanical Spectroscopy. *Proc. Natl. Acad. Sci.* **2017**, *114* (33), 8710–8715. https://doi.org/10.1073/pnas.1707251114.
(100) Young, W. W.; Katsumata, R. Intermediate Polymer Relaxation Explains the Anomalous Rheology of Nanocomposites with Ultrasmall Attractive POSS Nanoparticles. *ACS Polym. Au* **2023**, *3* (6), 466–474. https://doi.org/10.1021/acspolymersau.3c00020.
(101) Poh, L.; Narimissa, E.; Wagner, M. H.; Winter, H. H. Interactive Shear and Extensional Rheology—25 Years of IRIS Software. *Rheol. Acta* **2022**, *61* (4), 259–269. https://doi.org/10.1007/s00397-022-01331-6.

(102) Takahashi, Y.; Ochiai, N.; Matsushita, Y.; Noda, I. Viscoelastic Properties of Poly(2-Vinylpyridine) in Bulk and Solution. *Polym. J.* **1996**, *28* (12), 1065–1070. https://doi.org/10.1295/polymj.28.1065.
(103) Baeza, G. P.; Dessi, C.; Costanzo, S.; Zhao, D.; Gong, S.; Alegria, A.; Colby, R. H.; Rubinstein, M.; Vlassopoulos, D.; Kumar, S. K. Network Dynamics in Nanofilled Polymers. *Nat. Commun.* **2016**, *7*, 11368. https://doi.org/10.1038/ncomms11368.
(104) Akcora, P.; Kumar, S. K.; Moll, J.; Lewis, S.; Schadler, L. S.; Li, Y.; Benicewicz, B. C.; Sandy, A.; Narayanan, S.; Ilavsky, J.; Thiyagarajan, P.; Colby, R. H.; Douglas, J. F. "Gel-like" Mechanical Reinforcement in Polymer Nanocomposite Melts. *Macromolecules* **2010**, *43* (2), 1003–1010. https://doi.org/10.1021/ma902072d.
(105) Young, W. W.; Tabuchi, H.; Iguchi, R.; Konishi, T.; Fukao, K.; Katsumata, R. A Hidden Relaxation Process in Poly(2-Vinylpyridine) Homopolymers, Copolymers, and Nanocomposites. *Macromolecules* **2022**, *55* (15), 6590–6597. https://doi.org/10.1021/acs.macromol.2c00789.
(106) Golkaram, M.; Loos, K. A Critical Approach to Polymer Dynamics in Supramolecular Polymers. *Macromolecules* **2019**, *52* (24), 9427–9444. https://doi.org/10.1021/acs.macromol.9b02085.
(107) Richert, R.; Agapov, A.; Sokolov, A. P. Appearance of a Debye Process at the Conductivity Relaxation Frequency of a Viscous Liquid. *J. Chem. Phys.* **2011**, *134* (10), 104508. https://doi.org/10.1063/1.3565481.
(108) *Broadband Dielectric Spectroscopy: A Modern Analytical Technique*; Woodward, W. H. H., Ed.; American Chemical Society, Series Ed.; ACS Symposium Series; American Chemical Society: Washington, DC, 2021; Vol. 1375. https://doi.org/10.1021/bk-2021-1375.
(109) Richert, R. Comment on "Hidden Slow Dynamics in Water." *Phys. Rev. Lett.* **2010**, *104* (24), 249801. https://doi.org/10.1103/PhysRevLett.104.249801.
(110) Richert, R. Insulated Electrodes for Eliminating Conductivity in Dielectric Relaxation Experiments. *Eur. Phys. J. B* **2009**, *68* (2), 197–200. https://doi.org/10.1140/epjb/e2009-00084-8.
(111) Gainaru, C. P.; Böhmer, R. Comment on "Hidden Slow Dynamics in Water." *Phys. Rev. Lett.* **2010**, *104* (24), 249803. https://doi.org/10.1103/PhysRevLett.104.249803.
(112) Wind, M.; Graf, R.; Heuer, A.; Spiess, H. W. Structural Relaxation of Polymers at the Glass Transition: Conformational Memory in Poly(n-Alkylmethacrylates). *Phys. Rev. Lett.* **2003**, *91* (15), 155702. https://doi.org/10.1103/PhysRevLett.91.155702.
(113) Ewen, B.; Richter, D. Neutron Spin Echo Investigations on the Segmental Dynamics of Polymers in Melts, Networks and Solutions. In *Neutron Spin Echo Spectroscopy Viscoelasticity Rheology*; Advances in Polymer Science; Springer Berlin Heidelberg: Berlin, Heidelberg, 1997; pp 1–129. https://doi.org/10.1007/3-540-68449-2_1.
(114) Musino, D.; Oberdisse, J.; Farago, B.; Alegria, A.; Genix, A.-C. Resolving Segmental Polymer Dynamics in Nanocomposites by Incoherent Neutron Spin–Echo Spectroscopy. *ACS Macro Lett.* **2020**, *9* (6), 910–916. https://doi.org/10.1021/acsmacrolett.0c00369.

(115) Magde, D.; Elson, E.; Webb, W. W. Thermodynamic Fluctuations in a Reacting System---Measurement by Fluorescence Correlation Spectroscopy. *Phys. Rev. Lett.* **1972**, *29* (11), 705–708. https://doi.org/10.1103/PhysRevLett.29.705.
(116) Wöll, D. Fluorescence Correlation Spectroscopy in Polymer Science. *RSC Adv.* **2013**, *4* (5), 2447–2465. https://doi.org/10.1039/C3RA44909B.
(117) Flier, B. M. I.; Baier, M. C.; Huber, J.; Müllen, K.; Mecking, S.; Zumbusch, A.; Wöll, D. Heterogeneous Diffusion in Thin Polymer Films As Observed by High-Temperature Single-Molecule Fluorescence Microscopy. *J. Am. Chem. Soc.* **2012**, *134* (1), 480–488. https://doi.org/10.1021/ja208581r.
(118) Kulzer, F.; Xia, T.; Orrit, M. Single Molecules as Optical Nanoprobes for Soft and Complex Matter. *Angew. Chem. Int. Ed.* **2010**, *49* (5), 854–866. https://doi.org/10.1002/anie.200904858.
(119) Müller, C. B.; Richtering, W. Sealed and Temperature-Controlled Sample Cell for Inverted and Confocal Microscopes and Fluorescence Correlation Spectroscopy. *Colloid Polym. Sci.* **2008**, *286* (11), 1215–1222. https://doi.org/10.1007/s00396-008-1901-3.
(120) Reorientation and Translation of Individual Dye Molecules in a Polymer Matrix. *Eur. Polym. J.* **2004**, *40* (5), 1019–1026. https://doi.org/10.1016/j.eurpolymj.2004.01.016.
(121) Ikawa, T.; Shiga, T.; Okada, A. Measurement of Residual Stresses in Injection-Molded Polymer Parts by Time-Resolved Fluorescence. *J. Appl. Polym. Sci.* **2002**, *83* (12), 2600–2603. https://doi.org/10.1002/app.10212.
(122) Vallée, R. A. L.; Vancso, G. J.; van Hulst, N. F.; Calbert, J.-P.; Cornil, J.; Brédas, J. L. Molecular Fluorescence Lifetime Fluctuations: On the Possible Role of Conformational Effects. *Chem. Phys. Lett.* **2003**, *372* (1), 282–287. https://doi.org/10.1016/S0009-2614(03)00379-8.
(123) Vallée, R. A. L.; Tomczak, N.; Vancso, G. J.; Kuipers, L.; van Hulst, N. F. Fluorescence Lifetime Fluctuations of Single Molecules Probe Local Density Fluctuations in Disordered Media: A Bulk Approach. *J. Chem. Phys.* **2005**, *122* (11), 114704. https://doi.org/10.1063/1.1861881.
(124) Braeken, E.; De Cremer, G.; Marsal, P.; Pèpe, G.; Müllen, K.; Vallée, R. A. L. Single Molecule Probing of the Local Segmental Relaxation Dynamics in Polymer above the Glass Transition Temperature. *J. Am. Chem. Soc.* **2009**, *131* (34), 12201–12210. https://doi.org/10.1021/ja901636v.
(125) Kawaguchi, D.; Tateishi, Y.; Tanaka, K. Time-Resolved Fluorescence Analysis for Dye-Labeled Polystyrene in Thin Films. *J. Non-Cryst. Solids* **2015**, *407*, 284–287. https://doi.org/10.1016/j.jnoncrysol.2014.09.010.
(126) Vu, H.; Woodcock, J. W.; Krishnamurthy, A.; Obrzut, J.; Gilman, J. W.; Coughlin, E. B. Visualization of Polymer Dynamics in Cellulose Nanocrystal Matrices Using Fluorescence Lifetime Measurements. *ACS Appl. Mater. Interfaces* **2022**, *14* (8), 10793–10804. https://doi.org/10.1021/acsami.1c21906.
(127) Ellison, C. J.; Torkelson, J. M. The Distribution of Glass-Transition Temperatures in Nanoscopically Confined Glass Formers. *Nat. Mater.* **2003**, *2* (10), 695–700. https://doi.org/10.1038/nmat980.

(128) Ellison, C. J.; Torkelson, J. M. Sensing the Glass Transition in Thin and Ultrathin Polymer Films via Fluorescence Probes and Labels. *J. Polym. Sci. Part B Polym. Phys.* **2002**, *40* (24), 2745–2758. https://doi.org/10.1002/polb.10343.
(129) Albuszis, M.; J. Roth, P.; Pauer, W.; Moritz, H.-U. Macroporous Uniform Azide- and Alkyne-Functional Polymer Microspheres with Tuneable Surface Area: Synthesis, in-Depth Characterization and Click-Modification. *Polym. Chem.* **2014**, *5* (19), 5689–5699. https://doi.org/10.1039/C4PY00709C.
(130) Katzenstein, J. M. Mobility in Polymer Thin Films : Diffusion and Marangoni Driven Patterning. Thesis, 2013. https://repositories.lib.utexas.edu/handle/2152/25121 (accessed 2019-06-27).
(131) Von Meerwall, E. D.; Amis, E. J.; Ferry, J. D. Self-Diffusion in Solutions of Polystyrene in Tetrahydrofuran: Comparison of Concentration Dependences of the Diffusion Coefficients of Polymer, Solvent, and a Ternary Probe Component. *Macromolecules* **1985**, *18* (2), 260–266. https://doi.org/10.1021/ma00144a024.
(132) P. T. Callaghan; D. N. Pinder. Self-Diffusion of Random-Coil Polystyrene Determined by Pulsed Field Gradient Nuclear Magnetic Resonance: Dependence on Concentration and Molar Mass | Macromolecules. *Macromolecules* **1980**, *14*, 1334–1340. https://doi.org/10.1021/ma50006a037.
(133) Wöll, D.; Braeken, E.; Deres, A.; Schryver, F. C. D.; Uji-i, H.; Hofkens, J. Polymers and Single Molecule Fluorescence Spectroscopy , What Can We Learn? *Chem. Soc. Rev.* **2009**, *38* (2), 313–328. https://doi.org/10.1039/B704319H.
(134) Tanaka, K.; Tateishi, Y.; Okada, Y.; Nagamura, T.; Doi, M.; Morita, H. Interfacial Mobility of Polymers on Inorganic Solids. *J. Phys. Chem. B* **2009**, *113* (14), 4571–4577. https://doi.org/10.1021/jp810370f.
(135) Katzenstein, J. M.; Janes, D. W.; Hocker, H. E.; Chandler, J. K.; Ellison, C. J. Nanoconfined Self-Diffusion of Poly(Isobutyl Methacrylate) in Films with a Thickness-Independent Glass Transition. *Macromolecules* **2012**, *45* (3), 1544–1552. https://doi.org/10.1021/ma202362j.
(136) Katsumata, R.; Dulaney, A. R.; Kim, C. B.; Ellison, C. J. Glass Transition and Self-Diffusion of Unentangled Polymer Melts Nanoconfined by Different Interfaces. *Macromolecules* **2018**, *51* (19), 7509–7517. https://doi.org/10.1021/acs.macromol.8b00475.